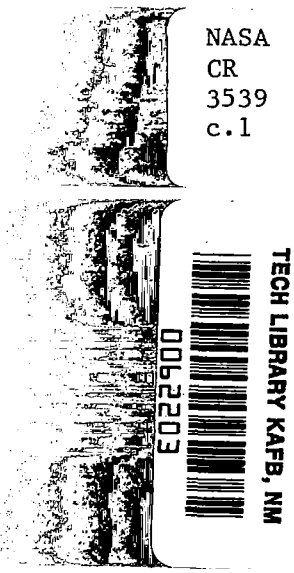

NASA Contractor Report 3539

Development of a Locally Mass Flux Conservative Computer Code for Calculating 3-D Viscous Flow in Turbomachines

Leonard Walitt

CONTRACT NAS3-20834
APRIL 1982

NASA

NASA Contractor Report 3539

Development of a Locally Mass Flux Conservative Computer Code for Calculating 3-D Viscous Flow in Turbomachines

Leonard Walitt
Thermo Mechanical Systems Company
Canoga Park, California

Prepared for
Lewis Research Center
under Contract NAS3-20834

National Aeronautics
and Space Administration

**Scientific and Technical
Information Branch**

1982

TABLE OF CONTENTS

SUMMARY

The VANS successive approximation numerical method has been extended to the computation of 3-D, viscous, transonic flows in turbomachines. The principal development reported herein is the generation of a cross-sectional computer code, which conserves mass flux at each point of the cross-sectional surface of computation.

In the VANS numerical method, the cross-sectional computation follows a blade-to-blade calculation. The VANS blade-to-blade code was developed earlier.

Numerical calculations were made for an axial annular turbine cascade and a transonic, centrifugal impeller with splitter vanes. The subsonic turbine cascade computation was generated in blade-to-blade surfaces to evaluate the accuracy of the blade-to-blade mode of marching. Calculated blade pressures at the hub, mid, and tip radii of the cascade agreed with corresponding measurements. The transonic impeller computation was conducted to test the newly developed locally mass flux conservative cross-sectional computer code. Both blade-to-blade and cross-sectional modes of calculation were implemented for this problem. A triple point shock structure was computed in the inducer region of the impeller. In addition, time averaged shroud static pressures generally agreed with measured shroud pressures.

The principal conclusions drawn from this research effort are two-fold:

1. The blade-to-blade computation produces a useful engineering flow field in regions of subsonic relative flow.

2. Cross-sectional computation, with a locally mass flux conservative continuity equation, is required to compute the shock waves in regions of supersonic relative flow.

1.0 INTRODUCTION

The results reported herein are part of a continuing joint U.S.Army Propulsion Laboratory-NASA Lewis Research Center program concerned with numerical simulation of three-dimensional, viscous flow fields in turbomachines.

Under Contracts NAS3-108016 and NAS3-20032 a blade-to-blade computer code, called "VANS/BB", and a cross-sectional computer code, called "VANS/CS", were developed. Starting from a quasi-three-dimensional flow field, such as that generated by the MERIDL code (Ref.1), the VANS/BB and VANS/CS computer programs are applied respectively, to compute the 3-D, viscous flow in a turbomachine.

The research reported in this submittal addresses advanced VANS/BB and VANS/CS code developments and applications of these codes to a subsonic axial annular turbine cascade and a transonic centrifugal impeller with splitter vanes.

The principal code developments concern the employment of a continuous two-dimensinal interpolation scheme with VANS codes, a wedge force balance computational algorithm for the VANS codes and modification to the cross-sectional (VANS/CS) computer program. VANS/CS was modified to solve an exact continuity equation in each cross-sectional surface. Thus, the mass flux is conserved both locally and throughout the cross-section. In addition, the streamwise pressure gradient, which is the driving force for the cross-section computation, was modified to suit both supersonic and subsonic regions of the flow field. These modifications and their applications are the principal subjects discussed. Appendix A addresses the interpolation scheme, while Appendix B describes the wedge force balance algorithm. The mass flux conservative VANS/CS code is described in the main text of the report.

The report covers the following five topics:

1. Background.
2. Formulation of locally mass flux conservative numerical method.
3. Subsonic axial turbine cascade computations.
4. Transonic contrifugal impeller computations.
5. Conclusions and recommendations.

Dr. Theodore Katsanis helped develope the VANS blade-to-blade computer code, generated the zeroth approximate field for the axial cascade, and ran a portion of the axial cascade problem reported herein. Mr. Theodore McKain of the Detroit Diesel Allison Division of General Motors generated the zeroth approximate field for the impeller computation and provided helpful suggestions during the course of this work. Mr. Dennis C. Chapman of the Detroit Diesel Allison Division of General Motors provided many helpful discussions and suggestions in the process of solving for the impeller plow field. Messrs. Curtis C. Walker and John Acurio of the Army Propulsion Laboratory provided many helpful suggestions and discussions for both the axial turbine cascade and centrifugal impeller problems presented herein.

2.0 SYMBOLS

C_p Heat Capacity at Constant Pressure

C_v Heat Capacity at Constant Volume

E Specific Internal Energy

H Thermodynamic Heat Function or Enthalpy

h_x Metric of Transformation

h_y Metric of Transformation

h_z Metric of Transformation

$\underline{i}$ Unit Vector of Curvilinear Coordinate x

$\underline{i}_1$ Unit Vector of Rotating Cartesian Coordinate of X_1

$\underline{i}_2$ Unit Vector of Rotating Cartesian Coordinate of X_2

$\underline{i}_3$ Unit Vector of Rotating Cartesian Coordinate of X_3

$\underline{j}$ Unit Vector of Curvilinear Coordinate y

J Index Specifying Streamlike-lines on blade-to-blade Surface

K Index Specifying Potential-like lines on blade-to-blade Surface

$\underline{k}$ Unit Vector of Curvilinear Coordinate z

$\tilde{K}_s$ Von Karman's Constant

M Momentum

m Mass

n Time Index for Finite Difference equation

P Pressure

R_o Maximum Radius of the Impeller (at the exit)

r,R Radial Coordinate, which together with X_3 form a Cylindrical Coordinate System

S_x Grid Velocity Component along x Direction

S_y Grid Velocity Component along y Direction

T_{ij} Total Laminar Stress Tensor

t Time or Time-like-variable

u Particle Velocity Component along x Direction

$\underline{u}$ Particle Velocity Vector

U_z Speed of March along z Direction

v Particle Velocity Component along y Direction

$\frac{V}{Vcr}$ Critical Velocity Ratio

w Particle Velocity Component along z Direction

$w'=w-U_z$ Velocity along z on a Galilean Frame which moves with a Constant Speed U_z along z with respect to the laboratory frame

x Curvilinear Coordinate along Azimuthal Direction

X_1 Coordinate Axes of Rotating Cartesian Coordinate which Rotate about Axial Axis X_3 with Speed ω

X_2 Coordinate Axes of Rotating Cartesian Coordinate which Rotate about Axial Axis X_3 with Speed ω

X_3 Axial Coordinate

y Curvilinear Coordinate along Streamwise Direction (from inlet to discharge)

z Curvilinear Coordinate in Marching Direction

Symbols in Greek Letters

γ Heat Capacity Ratio C_p/C_v

δ Boundary Layer Thickness

δ^* Incompressible Displacement Thickness

ϵ Eddy Viscosity

μ Molecular Viscosity Coefficient

ν Kinematic Viscosity Coefficient

$\underrightarrow{\omega}$ Rotation Velocity of Impeller

σ_{ij} Total Stress Tensor

τ_{ij} Reynolds Stress Tensor

α Pressure Blade Surface Meridional Angle

β Local Flow Angle Between Pressure Blade Surface and Meridional Plane

ρ Density

τ Characteristic Time

τ_w Shearing Stress at Wall

λ Viscosity Coefficient for the Deviatoril Strain $\lambda = -\frac{2}{3}\mu$

θ Azimuthal Coordinate Angle, together with r and X_3 form cylindrical coordinate system

(ξ_1, ξ_2, ξ_3) Curvilinear coordinates

3.0 BACKGROUND

The VANS numerical method is based on the combination of two different sets of principles developed for solving the parabolized steady Navier-Stokes equations for three-dimensional viscous flow. These principles have evolved from two independent studies of the parabolized Navier-Stokes equations. The first set of principles were developed for parabolized Navier-Stokes computations for supersonic flow by Lubard and Helliwell (Refs. 2 and 3) and Schiff and Steger (Ref. 4). The second set of principles evolved from parabolized Navies-Stokes computations for subsonic duct flows by Patankas and Spalding (Ref. 5), Briley and McDonald (Ref. 6), and Moore and Moore (Refs. 7 and 8).

For supersonic flow about a body-at-angle-of-attack (Ref. 3), it is assumed that in the viscous terms of the equations of motion, streamwise derivatives $\frac{\partial}{\partial \xi_1}$ are smaller than derivatives away from the body $\frac{\partial}{\partial \xi_2}$ and derivatives around the body $\frac{\partial}{\partial \xi_3}$. The resulting system of equations is called the parabolized Navier-Stokes equations (PNS) for supersonic flow. Supersonic PNS approximations can be achieved for body conforming coordinate systems (ξ_1, ξ_2, ξ_3). The equations are solved by marching in the ξ_1 direction with elliptic effects accounted for in the ξ_2 and ξ_3 coordinates.

An integral part of the supersonic PNS method is the evaluation of the pressure term $\frac{\partial P}{\partial \xi_1}$ in the streamwise momentum equation. For supersonic regions of the flow field, the term $\frac{\partial P}{\partial \xi_1}$ can be backward differenced. Based on streamwise pressure gradient differencing, the computation of shock-wave patterns have been an integral part of this method. However, where the local Mach number is near or less than unity, there is a possibility for departure solutions. Suppression of departure solutions requires proper numerical treatment of $\frac{\partial P}{\partial \xi_1}$ in subsonic regions. Thus, supersonic PNS methods are applicable to supersonic flows and may be extended to small local regions of subsonic flow.

For subsonic duct flows the Navier-Stokes equations are solved by iteration between a marching integration of the conservation relations through the flow field, and the solution of an elliptic pressure correlation equation (Refs. 8 and 9). This method is referred to as the subsonic PNS technique. The solution proceeds from an initial approximation to the pressure $Pa(\xi_1, \xi_2, \xi_3)$. The momentum equations are updated in the streamwise direction ξ_1 throughout a given cross-sectional surface to determine the velocity components u_1, u_2, u_3 using the estimated pressure distribution $P_a(\xi_1, \xi_2, \xi_3)$. The equation of state is employed with either the rothalpy relation for rotating systems, or uniform stagnation temperature for stationary systems, to compute the specific internal energy and density. A three-dimensional elliptic pressure-correction equation is then solved, to obtain an improved estimate of the pressure distribution. The pressure-correction equation depends on the error in cross-sectional mass flow rate, which is evaluated for each iteration. The iteration proceeds until a mass flow rate with desired accuracy is obtained. The method of Reference 7 is limited to subsonic flow mainly because density variations are neglected in the formulation of the pressure-correction equations. This results in convergence problems for the iteration process at Mach numbers near and above unity. However, it is believed that even if the iteration method were made convergent at supersonic speeds, correct shock structure prediction would be beyond this scheme, due to the approximate nature of the continuity equation being solved.

For mixed supersonic-subsonic flows, which occur in many impellers, one must either extend the supersonic PNS method into the subsonic domain, or revise the subsonic PNS analysis to include supersonic flow. It is doubtful that the subsonic PNS analysis can be extended to supersonic flows; hence, the supersonic PNS approach was adopted here.

The original VANS* successive approximation method has been described in detail previously and the integral equations solved cited (Refs. 9,10,and 11). In the next four paragraphs the original method is briefly reveiwed.

For illustrative purposes we start with a schematic of a radial impeller for a centrifugal compressor shown in Fig. 1. The machine is rotating clockwise about the system's axis. Let us consider the darkened blading passage. The blade surface labelled "pressure surface" is like the windward side of an airfoil, while the blade surface, labelled "section surface" is like the leeward side of an airfoil.

In the blade-to-blade mode of marching, the computation takes place on a blade-to-blade surface which is normal to the meridional planes of the machine, extends from inducer to the discharge, and moves from the hub to the shroud. The darkened surface of Fig. 1 is the hub blade-to-blade surface. The blade-to-blade method of marching is illustrated in the blade passage schematic shown in Fig. 2. The X_1,X_2, and X_3 coordinates of Fig. 2 represent a left handed, rotating, Cartesian coordinate system and coordinates (x,y,z) represent a left-handed, rotating, orthogonal, curvilinear coordinate system. The z-direction is the marching direction with the calculation taking place in the (x,y) blade-to-blade surfaces. The (x,y) blade-to-blade surfaces move from the hub to the shroud of the impeller. As the surface moves from hub to shroud, elliptic terms of the finite difference equations are evaluated from the zeroth approximation; i.e., the solution of Katsanis and McNally (1), while parabolic terms are evaluated directly from data within the blade-to-blade surface. Elliptic terms have to do with hub to shroud derivatives, with respect to z, and all other terms are considered parabolic terms.

*The letters VANS stand for Vectorized Asymmetric Navier Stokes codes.

In the cross-sectional mode of marching we move down the channel, from the inducer to discharge, in cross-sectional surfaces normal to the hub and shroud of the system. A schematic of the blade passage with the cross-sectional surface indicated is presented in Fig. 3. The z-direction is now normal to the (x,y) cross-sectional surface of Fig. 3. The (x,y) cross-sectional surfaces move from the inducer to the discharge of the impeller. The elliptic and parabolic terms in the cross-sectional mode of marching are the reverse of what they were previously in the blade-to-blade mode. Now streamwise derivatives become elliptic terms, since z moves in the streamwise direction, and hub-shroud derivatives are parabolic terms. This permutation of elliptic and parabolic terms, resulting from alternating the direction of marching, produces rapid adjustment of the field in a few passes through the system.

The blade-to blade march accounts for blade separations and upstream influence effects, while the cross-sectional march accounts for shroud scrubbing, blade leakage, hub effects and channel corner vortices. The cross-sectional mode of computation integrates the blade fluid mechanics with the effects of the shroud,hub and leakage.

Integral equations for conservation of mass, x-momentum, y-momentum z-momentum and the internal energy relation are presented in Appendix A. These relations are applicable to blade-to-blade surfaces and cross-sectional surfaces. A permutation of the (x,y,z) curvilinear coordinates is all that is required to go from one surface to another. Derivations of these relations are presented in Ref. (9) and Ref. (10).

To illustrate the elliptic source terms and parabolic terms of the equations of motion, the equation for mass conservation on a zone of the

blade-to-blade surface (Fig. 2) is presented below.

$$\frac{\partial}{\partial t}\int_A \rho\, h_x h_y dA + \int_C \rho(\underline{q}-\underline{q}_s)\cdot \underline{n} dC + \frac{1}{U_z}\int_C \rho(U_z-w)\underline{q}_s \cdot \underline{n} dC = \frac{1}{U_z}\frac{\partial}{\partial t}\int_A \tilde{\rho}(U_z-\tilde{w})h_x h_y dA \quad (1)$$

where:

$$\underline{q} = uh_y h_z \underline{i} + vh_x h_z \underline{j} \quad (2)$$

$$\underline{q}_s = S_x h_y h_z \underline{i} + S_y h_x h_z \underline{j} \quad (3)$$

$$z = U_z t. \quad (4)$$

Eq. 1 represents the conservation of mass theorem in terms of area integrals for a zone in the (x,y) plane and line integrals evaluated on a curve C representing the zone perimeter in the (x,y) plane. Curvilinear effects are accounted for by the metrics h_x, h_y, h_z and their derivatives.* The term on the right-hand-side of Eq. 1 is an elliptic source term and must be evaluated from flow field properties of the zeroth approximation. The second term on the left-hand-side of Eq. 1 is a parabolic term which is evaluated directly. The third term on the left-hand-side of Eq. 1 is associated with grid motion and the elliptic source term on the right-hand-side of Eq.1. However, it is evaluated directly to maintain the self-consistency properties of the numerical method.

The VANS numerical method described above is applicable to both subsonic and supersonic flows. For subsonic flows the method produces quantitabely relevant flow field data (Ref. 1). However, it has been found that for the supersonic case, VANS calculated shock-waves are smeared out and generally weaker than they should be. This has been traced to the approximate continuity equation solved in the algorithm. Continuity Eq.1 has a source term on the righ-hand-side, which causes the shock-wave problems.

---

*The variables of Eq. 1 are defined in Section 2.0.

In order to correct the continuity equation deficiency, a modified VANS cross-sectional code was generated. The modified code, designated "VANS/CS/MC", numerically solves the exact continuity equation for steady, three-dimensional flow. The revised mass conservative VANS numerical method is the subject of Section 4.0.

4.0 FORMULATION OF LOCALLY MASS FLUX CONSERVATIVE NUMERICAL METHOD

The locally mass flux conservative method herein is based on a combination of the principles upon which the supersonic and subsonic PNS techniques are based. In particular, the cross-sectional finite difference equations are formulated along the lines of the supersonic PNS method, and the blade-to-blade mode of computation is employed to determine the streamwise pressure gradient in regions of subsonic flow. The revised method is similar to that described in Section 3.0. It is composed of the blade-to-blade mode of marching, followed by the cross-sectional mode of marching.

4.1 Blade-to-Blade Mode of Computation

Integral equations of the blade-to-blade mode of computation are presented in Appendix C. These relations apply to a zone of the blade-to-blade surface of Fig. 2 and are the same as presented previously (Ref. 10). In fact, the blade-to-blade mode of computation is identical to that developed previously. This field is computed in two steps.

1. The computation is conducted at the hub blade-to-blade surface until the pressure field has stabilized there.

2. The blade-to-blade surface is then moved from hub to shroud using the unsteady analogy; i.e., the time variable in the Equations of Motion of Appendix A is related to the curvilinear distance variable z according to Eq.(4).

The procedure for explicitly solving equations C1 to C6 of Appendix C is as follows:

1. The approximate Continuity Equation(C1) is solved for the density field throughout the blade-to-blade surface.

2. The Internal Energy relation (C2) and the Equation of State (C3) are solved simultaneously for the specific internal energy, pressure and stress tensor.

3. The x, y, and z momentum equations (C4,C5, C6) are solved, respectively, for (M_x, M_y, M_z) and (u,v,w). This mode of computation is weakly coupled to the pressure gradient in the hub-shroud direction, i.e., $\frac{\partial P}{\partial z}$. This is precisely what is required, since the hub-shroud pressure gradient is not well known from the quasi-3-D zeroth approximate field. This technique produces a satisfactory flow field in the blade-to-blade surface itself for subsonic flow. However,poor predictions of the hub-shroud component of velocity (w) result. This is because the hub-shroud component of velocity depends strongly on the pressure gradient in this direction, which is not well defined in the zeroth approximate quasi-3-D solution.

4.2 Cross-Sectional Mode of Computation

Integral equations for the revised cross-sectional mode of computation are presented in Appendix D. These relations are applicable to a zone of the cross-sectional shown in Fig.3.It is seen from the Appendices that the Continuity Eq. D2 differs from Continuity Eq. C1. Eq. C1 contains a source term on the right hand side,while Eq. D2 is exact. In fact, the Internal Energy relation D5, Momentum equations D1, D7, and D8 are all missing a source term in comparison to their respective equations C, C, and C. Furthermore, the dependent variables updated in Appendix D contain the stream-wise component of velocity w.

The procedure for explicitly solving the equations of Appendix D is similar to that of supersonic PNS computation (Ref. 2). Computation is conducted by marching in the z direction in five steps.

1. The z direction momentum flux is computed from Eq. D1. This flux parameter, $(\rho ww)_{z\ \text{momentum}}$, is strongly dependent on the stress gradient,

$$\frac{\partial \sigma_{zz}}{\partial z} = \frac{1}{Uz} \frac{\partial}{\partial t} \int_A h_x h_y \tilde{\sigma}_{zz}\, dA \quad , \qquad \text{of Eq. D1.}$$

For supersonic flow regions this term is evaluated from the blade-to-blade pressure gradient of Section 4.1, corrected by its zeroth approximate pressure gradient, while for subsonic flow regions it is evaluated from the blade-to-blade pressure gradient of Section 4.1 directly. In addition, the pressure gradient is corrected in a manner similar to the Patankar and Spalding method (Ref. 5), to insure that mass flux is conserved from cross-section to cross-section.

2. Continuity Eq. D2 is then solved for the mass flux (ρw) continuity.

3. Eqs. D3 and D4 are solved for the z component of velocity and density, respectively.

4. The Internal Energy relation D5 and Eq. of state D6 are solved for the specific internal energy, pressure and stress tensor.

5. The (x,y) momentum equations,D7 and D8, are solved for u and v, respectively.

This method strongly couples the streamwise pressure gradient to compptation of the flow field and considers both supersonic and subsonic regions of the flow. In addition, the mass flux is exactly conserved in the flow passage. The mass flux conservation property is illustrated in Appendix E.

5.0 CALCULATION OF THE FLOW FIELD IN AN AXIAL ANNULAR TURBINE CASCADE

The VANS blade-to-blade code,i.e., VANS/BB, computed the flow field on a blade-to-blade surface which moved from the hub to the tip of the system. Calculations were conducted on the U.S. Army CDC 7600 computer in Huntsville, Alabama. To move the blade-to-blade surface from the hub to the tip of the cascade required 2.68 hours on the CDC 7600. In this period of computational time approximately unit characteristic time* passed.

This section is comprised of the following six topics:

1. Cascade geometry and input conditions.
2. Finite difference meshes, boundary conditions, and initial conditions.
3. Flow stabilization at hub.
4. General flow field structure.
5. Critical velocity ratio contours.
6. Comparisons of calculated and measured surface pressures.

5.1 Cascade Geometry and Input Conditions

The turbine cascade geometry is comprised of an annular ring of 36 vanes having a hub radius of 8.5 inches and a shroud radius of 10 inches. A schematic cross-sectinal view of the axial annular cascade experimental setup is shown in Fig. 4. The blade geometry and coordinates are shown in Fig. 5. The solidity at the mean radius, defined as the ratio of the axial chord to the pitch of the blades, is .93. This is similar to an axial fan.

---

*Unit characteristic time is defined as the time it takes a particle to travel from the leading to trailing edges of blade.

Flow conditions for the cascade are as follows:

1. $\left(\frac{V}{Vcr}\right)_i = .231$

2. $\left(\frac{V}{Vcr}\right)_e = .778$

3. $\dot{m} = .31132$ slug/sec

where $\left(\frac{V}{Vcr}\right)_i$ represents the ratio of velocity to critical velocity upstream of the blades, $\left(\frac{V}{Vcr}\right)_e$ represents the ratio of velocity to critical velocity far downstream of the blades at the mean radius, and $\dot{m}$ represents the mass flux passing through cascade.

The principal objective of this calculation is to apply the existing blade-to-blade, computer code, , i.e., VANS/BB, to the axial cascade problem. Application of the VANS/BB program to the cascade and comparison of calculations with experimental data (Ref.12) will demonstrate the validity of the unsteady analogy for subsonic flows.

5.2 Finite Difference Meshes, Boundary Conditions and Initial Conditions

Figs. 6 to 11 present finite difference meshes at the hub radius, mean radius and tip radius, respectively. Figs. 6 and 7 correspond to the hub, Figs. 8 and 9 correspond to the mean radius, and Figs. 10 and 11 correspond to the tip. All the meshes are comprised of 42 streamline-like-lines and 63 potential-like-lines. Spacing is fine near the blade surfaces and coarse in the center of the channel. Figs. 7, 9, and 11 present blow-ups of the mesh at the blade trailing edge. The blunt blade trailing edge is clearly seen at the pressure surface in these figures.

As the blade-to-blade surface moves from the hub to the tip of the system, the domain of computation increases. This is clearly seen in Figs. 6, 8, and 10. The increased domain of computation is caused by the increasing radius of the system. Thus, the flow in the axial annular turbine cascade system is clearly three-dimensional.

The hub blade-to-blade surface finite difference mesh for the axial annular cascade problem is shown in Fig. 6. This mesh is comprised of 42 streamline-like-lines and 63 potential-like-lines, i.e., 2646 mesh points. The streamline-like-line spacing is fine in the vicinity of the blade surfaces and coarse in the center of the passage. In addition, it is seen from Fig. 6 that the upstream boundary of the domain of computation is approximately 90% of an axial chord upstream of the blade leading edge. Figure 7 shows a blow-up of the finite difference mesh at the blade trailing edge. The blunt trailing edge is clearly shown in the figure.

Boundary conditions for this problem are as follows:

1. At the upstream boundary the MERIDL particle velocities are prescribed.

2. Along the lateral boundaries of the system, both upstream of and downstream of the blading, periodic boundary conditions are envoked.

3. Along the blade surfaces themselves, no slip flow is enforced.

4. At the downstream boundary of the region of calculation the MERIDL computed static pressure multiplied by the factor 1.1 is enforced.

The MERIDL quasi-3-D flow field (Ref.1) serves as the zeroth approximate solution and initial condition for the computation. Blade-to-blade computation does not consider hub or shroud effects. The MERIDL quasi 3-D field at the hub becomes the initial condition for the hub stabilization computation.

5.3 Flow Stabilization at Hub

The axial annular cascade problem stabilization process is very complex. Calculation starts with the hub MERIDL blade-to-blade field as the initial condition and develops from there. The blade-to-blade surface was moved at low speed, i.e., $U_z \approx 5$ fps, to stabilize the hub flow field.

The upstream boundary location of the axial annular cascade, which was 90% of an axial chord upstream of the blade leading edge, produced a

stagnation pressure rise of 7.8 percent at the upstream boundary. However, the upstream critical velocity ratio was $\left(\frac{V}{V_{cr}}\right)_i = .225$, which was .006 units less than the input critical velocity ratio. Therefore, the effects of this upstream boundary location were to primarily increase the incoming pressure level of the system, with little change to the basic system fluid mechanics. Hence, if the back pressure is increased, the calculations and measurements can be compared on a non-dimensional basis. The poor MERIDL zeroth approximate field is the principal reason for this interaction at the upstream boundary.

The flow field calculation at the hub took place in two stages. First, the MERIDL pressure was imposed at the downstream boundary and the flow field was run to stabilization. As described above, this produced a stagnation pressure rise at the downstream boundary. Since the MERIDL pressure P_{3M} was imposed downstream, the ratio of MERIDL pressure to upstream stagnation pressure was $(P_{3M}/P_{to})_M = .594$. This value was too low. The hub after-mixed-static-to-total pressure ratio should be $(P_{3M}/P_{to})_{AM} = .65$. Therefore, the MERIDL pressure was multiplied by 1.10 to produce the proper downstream static-to-total pressure ratio. Based on the revised back pressure, the second stage of the computation was conducted. The second stage computation continued until the pressure field did not change on the blade surfaces.

Figs. 12 and 13 show hub pressure surface and suction surface pressure distributions, respectively. The three distributions correspond to three characteristic times τ in the computation. Unit characteristic time corresponds to the time it takes a particle to travel an axial chord. It is seen from Figs. 12 and 13 that the pressure variations at characteristic times $\tau = 2.667$

and τ = 2.717 are almost identical. Two hundred cycles of computation exist between characteristic times τ = 2.717 and τ = 2.667. Therefore, the hub flow field was stabilized at characteristic time τ = 2.717.

5.4 General Flow Field Structure

The general flow field structure for this turbine cascade is depicted in velocity vector plots at the hub, mean and tip of the system. Figs. 14, 16, and 18 show the velocity fields on blade-to-blade surfaces at the hub, mean and tip of the cascade, respectively. Figs. 15, 17, and 19 show blow-ups in the discharge region at the hub, mean and tip, respectively.

The blunt leading edge stagnation point flow is clearly seen at the hub, mean and tip in Figs. 14, 16, and 18, respectively. At the leading edge of the pressure surface, the flow actually becomes negative at the hub (Fig. 14). This negative pressure surface leading edge flow becomes more pronounced at the tip (Fig. 18). At the hub and tip of the system, a horseshoe vortex forms at the pressure surface leading edge (Ref. 13). Since the effects of the hub and tip walls are not included in the blade-to-blade solutions, no horseshoe vortex can be calculated. However, it is interesting to note that some negative flow is computed in this region, even in the blade-to-blade computation.

A strong boundary layer flow is seen along the suction surface and pressure surface at the hub, mean and tip (Figs. 14, 16, 18). These boundary layers separate at the blunt trailing edge of the blade. The trailing edge separated region is clearly seen on the pressure surface in the velocity vector blow-up of Fig. 15, 17, and 19 at the hub, mean and tip of the system, respectively. Aft of the blade trailing edge a strong viscous near-wake is seen emanating downstream (Figs. 15, 17, 19).

5.5 Critical-Velocity Ratio Contours

Contours of the ratio of the velocity to the critical velocity are presented in Figs. 20 to 25. Figs. 20, 22, and 24 present contour plots over the entire domain of computation at the hub, mean, and tip radii, respectively. Critical velocity ratio blow-ups at the discharge are shown in Figs. 21, 23, and 25.

At the hub (Fig. 20), the flow expands from $\frac{V}{Vcr} \sim .20$ to $\frac{V}{Vcr} \sim .80$. However, near the suction surface islands of contour level $\frac{V}{Vcr} \sim .90$ are present. Thus, the flow is not uniformly expanded to a critical velocity ratio near .80. Boundary layers are indicated on both the pressure and suction surfaces. The suction surface boundary layer is thicker than the pressure surface boundary layer.

A strong near-wake flow is indicated at the hub in the critical velocity ratio blow-up of Fig. 21. The strong shear layer flow persists aft of the suction and pressure surfaces. Due to the separation at the trailing edge of the pressure surface, the shear layer aft of the pressure surface is thicker than the shear layer aft of the suction surface. Thus, a strong shear layer flow persists at an axial station of 19.05 percent of an axial chord aft of the blade trailing edge.

Fig. 22 presents a critical velocity ratio contour plot at the mean radius of the system. The flow now expands from $\frac{V}{Vcr} \sim .20$ to $\frac{V}{Vcr} \sim .70$. Furthermore, there are large islands of $\frac{V}{Vcr} \sim .80$ in a sea of contour level $\frac{V}{Vcr} \sim .70$. As was discussed in Section 5.1, the measured critical velocity ratio far downstream of the blades at the mean radius was $\frac{V}{Vcr} = .778$. This value is consistent with the contour plot of Fig. 17.

Strong boundary layer flows are indicated along the blade surfaces (Fig. 22), as well as strong shear flows in the near-wake of the system (Fig. 23). The shear layer flow aft of the suction surface is thicker than the corresponding shear layer flow aft of the pressure surface trailing edge.

Comparison of the contour plots at the hub and mean radii indicate that the flow is decelerating as the radius increases. This is consistent with the static pressure measurements of Goldman and McLallin (Ref. 12). The after-mixed ratio of static pressure-to-upstream stagnation pressure varies from .65 at the hub to .725 at the shroud (Ref. 12).

At the tip radius the cascade flow accelerates from $\frac{V}{Vcr} \sim .20$ to $\frac{V}{Vcr} \sim .70$ (Fig. 24). The tip radius expansion produces a nearby uniform flow at the critical velocity ratio $\frac{V}{Vcr} \sim .70$. There are no islands present in the discharge region at the tip radius (Fig.24).

Comparison of Figs. 20,22, and 24 clearly shows the effects of increasing the backpressure with increasing radius. The peak speed at the hub is $\frac{V}{Vcr} \sim .90$, the peak speed at the mean is $\frac{V}{Vcr} \sim .80$, and the peak speed at the shroud is $\frac{V}{Vcr} \sim .70$.

Strong boundary layer and wake flows are shown at the tip radius in Figs. 24 and 25, respectively. The separated pressure surface trailing edge flow produces a strong shear layer flow throughout the near-wake region (Fig.25).

5.6 Comparisons of Calculated and Measured Static Pressures

Figs. 26 to 28 compare calculated and measured surface pressures at the hub radius, mean radius, and tip radius, respectively. The solid line indicates the viscous VANS blade-to-blade calculation, the dashed line indicates the inviscid TSONIC blade-to-blade calculation (Ref. 14) and data points are the measured pressures of Goldman and McLallin (Ref. 12). The area between the solid curves of these figures represents the blade loading as predicted by VANS.

At the hub of the system (Fig. 26) the VANS prediction produces a good correspondence with data on the suction and pressure surfaces of the blade. The TSONIC prediction matches the pressure surface data quite well, except near the trailing edge where the inviscid pressure ratio returns to unity. On the suction surface, the TSONIC prediction is high at $X_3 \sim .08$ and at the trailing edge.

At the mean radius of the system (Fig. 27) the viscous VANS prediction and the inviscid TSONIC prediction are in excellent correspondence with data. However, since the TSONIC prediction is based on inviscid theory, it returns to a stagnation condition at the blade trailing edge. Thus, there is some trailing edge discrepancy in the TSONIC prediction.

Fig. 28 compares the surface pressures at the tip radius. The viscous VANS prediction is in excellent agreement with these data of Goldman and McLallin. The inviscid TSONIC prediction is in good agreement with pressure data except at $X_3 \sim .06$, where it is low, and at the trailing edge.

On balance both the VANS and TSONIC predictions are generally in accord with the measurements. Since TSONIC assumes inviscid flow, it cannot compute the separation and wake flow at the blade trailing edge.

The results of Section 5.6 clearly indicate that the VANS blade-to-blade prediction is in accord with the measurements of Goldman and McLallin (Ref.12). Thus, the unsteady analogy produces a satisfactory pressure field for the subsonic turbine cascade. However, the effects of the hub and tip end-walls are not yet included in the VANS prediction. To properly include end-wall effects a meridional mode of machining; i.e. VANS/MD, must be implemented, followed by the cross-sectional marching mode; i.e. VANS/CSM. This procedure would result in the computation of the horseshoe vortex as well as the remaining end-wall effects.

6.0 CALCULATION OF THE FLOW FIELD IN A TRANSONIC CENTRIFUGAL IMPELLER

The VANS computer codes have been applied to solve for the three-dimensional viscous flow field in the blading passage of a Detroit Diesel Allison* centrifugal impeller design (Ref. 15). The computation included transonic relative flow with shocks, shroud leakage effects, and inducer bleed slot effects. It is the objective of the section to describe the VANS blade-to-blade and cross-sectional computations.

This report covers three principal topics:

1. Schematic of impeller geometry and input conditions.
2. Calculated blade-to-blade field.
3. Calculated cross-sectional field.

6.1 Impeller Geometry and Input Conditions

The hub and shroud lines for the system are schematically indicated in Fig. 29. VANS evaluates the blade-to-blade and cross-sectional flow fields in the curvilinear coordinate system (x,y,z). For the blade-to-blade calculation streamline-like-lines represent traces of blade-to-blade surfaces and define curves of constant z-coordinate. Potential-like-lines, orthogonal to the streamline-like-lines, define curves of constant y-coordinate. The parameter x represents the angular coordinate. For the cross-sectional calculation the z and y coordinates permutate.

Input conditions for the geometry of Fig.29 are as follows:

laboratory stagnation pressure P^1_{ti} = 2116.22 psfa

laboratory stagnation temperature T^1_{ti} = 518.7°R

inducer tip critical velocity ratio ~ 1.22

---

*This work funded by Detroit Diesel Allison Division of General Motors under Purchase Order No. HO 1321.

6.2 The Blade-to-Blade Flow Field

Computation of the intermediate blade-to-blade flow field required six hours on the CYBER 176 computer.* The principal fluid mechanical effects calculated concern a leading edge suction surface separation at the hub and a trailing edge suction surface separation at the shroud.

A velocity vector plot of the flow field in the neighborhood of the leading edge of the suction surface is shown in Fig.30. The blade-to-blade surface meridinal trace is located approximately 12 percent of the distance between hub and shroud. A vortex is clearly indicated at the leading edge of the suction surface. This vortex occupies about 15 percent of the blade passage at the leading edge. It is believed that its cause is a 6degrees angle-of-attack with respect to the camber line leading edge. As the blade-to-blade surface moved towards the shroud, the angle-of-attack decreased to 2 degrees. This resulted in attached flow at the suction surface leading edge near the shroud.

A velocity vector plot of the discharge flow field in the neighborhood of the suction surface is shown in Fig.31. The blade-to-blade surface meridinal trace is located near the shroud in this case. A long narrow separated region exists along the suction surface. This region occupies about 10 percent of the passage between the splitter pressure surface and suction surface. The separation point occurs near an inflection point in the suction surface shape.

The blade-to-blade flow field, which contains leading and trailing edge suction surface separations, serves as the previous approximation to the cross-sectional mode of computation. Cross-sectional calculations are discussed

---

*CRAY-1 computation presently requires two hours, while future calculations should require 2/3 of an hour.

in the next section.

6.3 The Cross-Sectional Flow Field

Computation of the cross-sectional flow field required 4.9 hours* on the CDC7600 computer. Numerical results are specified in terms of velocity vector plots, critical velocity ratio contours and static pressure contours. These plots are made on various cross-sectional surfaces of computation.

Fig. 29 shows a schematic meridional view of the impeller including cross-sectional traces which have been analyzed. Each cross-sectional surface analyzed is labeled with the parameter $\tilde{z}$ defined as follows:

$$\tilde{z} = \frac{\text{hub meridional distance from blade leading edge}}{\text{hub meridional distance between leading and trailing edge of blade}}$$

A parameter $\tilde{z}$ = .105 means the cross-sectional surface is located 10.5 percent of the way to the discharge; negative $\tilde{z}$ values imply hub distances upstream of the blades. It is noted that the cross-sectional traces of Fig. 29 represent computational cross-sections which are not normal to the blading. Thus, these surfaces depict the angular component of velocity and portions of the radial and axial components. Secondary flows are difficult to visualize in these computational surfaces.

The cross-sectional flow field is first described generally in terms of velocity vector plots, then critical velocity ratio and pressure contour plots are presented. The inducer shock structure is then discussed. Finally, shroud pressure comparisons are made to evaluate calculational accuracy.

6.3.1 General Flow Field Structure

Velocity vector plots are shown in the inducer region in Figs. 32 to 39. In each figure the suction surface is labeled, the pressure surface is labeled, the hub and shroud lines are indicated, and the direction

*CRAY-1 computation presently requires 1.6 hours, while future calculations should require half an hour.

of rotation is specified. The ordinate m represents distance along the cross-sectional traces of Fig. 29, while the abcissa ℓ represents an arc length.

Fig. 32 shows a velocity vector plot upstream of the blading ($\tilde{z} = -.2183$). The cross-sectional flow is basically undisturbed with the angular component increasing with radius.

In Fig. 33 ($z = .1053$ of Fig. 29) the cross-section is completely within the blading. The flow separates at the suction surface near the hub, with a vortex normal to the plane of the paper. The low energy air in the vortical region is acted upon by the outward centrifugal force, producing an outward radial-like flow. This is clearly indicated in Fig. 33.

Leakage flow at the suction surface tip and an oblique shock-wave emanating from the pressure surface are also indicated in Fig. 33. The oblique shock-wave impacts the shroud at about 25 percent of the total shroud distance between blades.

The downward radial-like flow and fairly large angular components of velocity shown in the neighborhood of the suction surface (Fig. 33) are caused by the shape of the cross-sectional surface upon which the velocity vector plot is made. Since this surface is not normal to the blades, a portion of the streamwise velocity will show up. This will distort the secondary flow picture somewhat. To remedy the situation, data on the cross-sections of Fig. 29 should be interpolated onto a set of true cross-sectional surfaces. There was no time or funds to accomplish this under the present program.

The flow field just upstream of the bleed slot is shown in Fig. 34 ($\tilde{z} = .1362$). This field contains three fluid mechanical elements.

1. A strong outward radial flow along the suction surface, caused by the centrifugal force in the suction surface boundary layer and separated region.

2. Inward flow at the suction surface tip, due to the leakage.

3. An oblique shock-wave, whose trace impacts the shroud at approximately 40 percent of the blade-to-blade distance along the shroud.

At $\tilde{z}$ = .1522 (Fig. 35), the cross-sectional flow field is shown just downstream of the bleed slot leading edge (see Fig. 29). Outward radial-like-flow-exists along the suction surface in the center of the cross-section. This is a continuation of what was described previously in Figs. 33 and 34. Since the interior pressure increases as one moves from the suction to the pressure surface, bleed slot flux will enter the system near the suction surface and exit the system near the pressure surface. This is clearly indicated in Fig. 35. In addition, the bleed slot flow has affected the oblique shock trace, which was indicated in Figs. 33 and 34. This trace is no longer clearly defined.

The velocity field shown in Fig. 36 ($\tilde{z}$ = .1645) occurs when the cross-section is in the center of the bleed slot. Strong outward radial-like flow is indicated along the suction surface in the center of the cross-section, and a strong inward radial flow occurs at the bleed slot near the suction surface. Furthermore, the oblique shock wave trace of Figs. 33 and 34 is not well defined in Figure 36.

Fig. 37 ($\tilde{z}$ = .185) represents the flow field just aft of the bleed slot trailing edge. A large cross-sectional vortex is indicated at the shroud-suction surface junction. This vortex is caused by the interaction of the strong inward radial flow from the bleed slot and the outward radial flow along the suction surface. The streamwise flow is also negative in the vortical region; hence, a true three-dimensional separation has occurred.

Figs. 38 and 39 present velocity vector plots of the cross-sectional flow field at z parameters of .440 and .959, respectively.

At $\tilde{z}$ = .440 (Fig. 38) the velocity field is shown on a cross-section in the radial portion of the impeller. Comparison of Figs. 37 and 38, clearly indicates that the splitter vane greatly reduces the secondary flow distrotion in the cross section. The radial cross-section of Fig. 38 represents a true cross-sectional surface with respect to the blades; hence, the secondary flows of the system are clearly seen. The centrifugal forces near the pressure and suction surfaces produce an outward secondary flow in the low energy boundary layers on these walls.

In the backswept portion of the impeller, the cross-sections exhibit rake. Rake is clearly seen in Fig. 39.

The introduction of rake clearly increases the secondary flow distortions in the system. Fig. 39 shows higher distortion levels than Fig. 38. Furthermore, at $\tilde{z}$ = .959 the flow at the junction of the suction surface and shroud is separated.

The velocity vector plots of Figs. 32 to 39 have provided a qualitative picture of the inducer fluid mechanics. Principal elements of the fluid mechanics are fivefold:

1. The leading edge suction surface flow separated near the hub and the centrifugal force produced a radial outward flow in this region.

2. An oblique shock-wave emanated from the pressure surface.

3. The bleed slot produced a strong radial inward flow near the suction surface.

4. The interaction of the outward radial flow on the section surface and the inward bleed slot flow, produced a three-dimensional

vortex at the junction of the shroud and suction surface.

5. The trailing edge suction surface flow is separated.

6.3.2 Critical Velocity Ratio Contours

Figs. 40 to 44 show contour plots of the critical velocity ratio on the cross-sections labeled $\tilde{z}$ = .105, .136, .185, .440 and .954, respectively. These contour maps show the pressure surface on the left and suction surface on the right. This is opposite to the orientation of the velocity vector plots shown previously. Different plotting codes were employed to generate the contour maps.

At $\tilde{z}$ = .105 (Fig. 40), the cross-section surface is just inside the blading. Boundary layers are seen on the hub, pressure surface and shroud. The suction surface separation is indicated near the hub by the thickening of the boundary layer there. A peak critical velocity ratio contour of W/Wcr $\approx$ 1.4 is indicated in Fig. 40. Coalescence of the contour levels W/Wcr $\sim$ 1.4 and W/Wcr $\sim$ 1.3 defines the oblique shock trace; although, the definition is not sharp.

On the cross-section just upstream of the bleed slot (Fig. 41, $\tilde{z}$ = .136), the region of contour level W/Wcr $\sim$ 1.4 is smaller than the corresponding region of Fig. 40. The oblique shock-wave trace is moving towards the suction surface. In addition, boundary layers are indicated on the hub, shroud, and pressure surface. The thick layer along the suction surface represents the separated region near the hub and the effects of leakage inflow near the shroud.

In Fig. 42 ($\tilde{z}$ = .185), the critical velocity ratio contours are shown on a cross-section just aft of the bleed slot trailing edge. This contour map corresponds to the velocity vector plot of Fig. 37, which showed a vortical flow at the shroud-suction surface junction. The region of contour level W/Wcr $\sim$ 1.4 is now smaller than those of Figs. 40 and 41.

In what corresponds to the vortical region shown in the velocity vector plot of Fig. 37, the critical velocity ratio rapidly changes from W/Wcr $\sim$ 1.4 to approximately W/Wcr $\sim$ .40. That is, a normal shock trace exists between the regions of W/Wcr $\sim$ 1.4 and W/Wcr $\sim$ .40. Through the normal shock the critical velocity ratio goes from W/Wcr $\sim$ 1.4 to Wcr $\sim$ .90. As the parameter m increases the sonic line departs from the normal shock front. At the shroud the shock front is oblique. The oblique shock transition produces a critical velocity ratio change from W/Wcr $\sim$ 1.4 to W/Wcr $\sim$ 1.10. The normal shock, oblique shock and sonic line are labeled in the figure.

In summary, the critical velocity ratio contour plot of Fig. 42 depicts the interaction of a normal shock and an oblique shock. This interaction, which produces a slip stream, is commonly referred to as the "triple point." In Section 6.3.5 the triple point is further discussed.

Figs. 43 and 44 present relative-to-critical ratio contours on cross-sections whose z parameters are.440 and .954, respectively.

The velocity field in the radial portion of the system is indicated in Fig. 43. Fig. 43 ($\tilde{z}$ = .440) shows boundary layers on the hub, shroud, main blade and splitter vane. Loading of the blade is clearly indicated in the lefthand passage (between the main blade pressure surface and splitter suction surface); the shroud critical velocity ratios near the pressure surface are lower than those near the splitter suction surface. A peak critical velocity ratio contour level of $\frac{W}{Wcr} \sim .80$ exists in Fig. 43. Furthermore, the left and right hand passages have similar flows near the hub, but differ near the shroud. It is believed that the effects of the bleed slot injection are still present in the right hand passage.

The velocity field in the backswept region of the impeller, which also indicates rake , is shown in Fig. 44. Flow field deceleration is indicated in a comparison of Figs. 43 and 44. In the left hand passage of Fig. 44 ,

the average critical velocity ratio is $\frac{W}{Wcr} \sim .40$, while $\frac{W}{Wcr} \sim .80$ exists in the corresponding passage of Fig. 43. Furthermore, the left hand passage of Fig. 44 shows little loading near the hub and higher loading near the shroud. This result is in accord with the critical velocity ratio plot of Fig. 42 in the radial portion of the impeller. Finally, the right hand passage of Fig. 44 has greater distortion than the respective left hand passage.

6.3.3 Pressure Ratio Contours

Contours of the ratio of static pressure P to laboratory stagnation pressure $P_{t_i}^{1}$ are shown in Figs. 45, 46, 47, and 48.

Fig. 45 shows the pressure field on a cross-section just inside the blading ($\tilde{z} = .105$). The trace of the oblique-shock emanating from the pressure surface is clearly indicated. This front corresponds to the front shown in the velocity vector plot of Fig. 34. The oblique shock impacts the shroud at approximately 25 percent of the distance between pressure and suction surface. The pressure ratio corresponding to the peak critical velocity ratio region $W/Wcr \sim 1.4$ of Fig. 40 is $P/P_{t_i}^{1} \sim .40$. Fig. 45 also shows that the blade loading is farily high; $P/P_{t_i}^{1} \sim 1.10$ near the pressure surface and $P/P_{t_i}^{1} \sim .40$ near the suction surface.

At $\tilde{z} = .136$ (Fig. 46) the oblique shock trace has moved closer to the suction surface than in Fig. 45. The trace impacts the shroud at the 40 percent blade-to-blade distance. Fig. 46 also shows high blade loading, $P/P_{t_i}^{1} \sim 1.10$ near the pressure surface and $P/P_{t_i}^{1} \sim .40$ near the suction surface.

Figs. 47 and 48 show contour plots of the ratio of static pressure P to the laboratory total pressure $P_{t_i}^{1}$. An examination of these figures shows that the static pressure of the system gradually rises from about $\frac{P}{P_{t_i}^{1}} \sim 1.6$ at $\tilde{z} \sim .440$ to $\frac{P}{P_{t_i}^{1}} \sim 3.2$ at $\tilde{z} = .954$. In the radial portion of the system (Fig. 47) the cross sections are strongly loaded near the shroud. This was also indicated in the critical velocity ratio plots of Figure 43.

Finally, pressure contour plots in the right-hand-passage of Fig. 48 clearly indicate higher distortion than the corresponding contour plots in the left-hand-passage.

6.3.4 Inducer Flow Field Shock Structure

Based on the pressure and critical velocity ratio contour plots of Sections 6.3.2 and 6.3.3 the inducer shock structure was mapped on the shroud blade-to-blade surface. This section presents the mapped shock field and discusses the validity of this field in the inducer region.

Fig. 49 shows the flow field structure in the impeller inducer region at the shroud. The abscissa represents meridional distance $m = \int hydy$, while the ordinate represents the arc length $\ell = \int hxdx$. The solid lines indicate the shock structure, while the dashed lines indicate traces of streamlines.

The shock structure is composed of three elements. An oblique shock emanating from the pressure surface of the system, a normal shock at the leading edge of the bleed slot, and a reflected oblique shock. The mass injection causes the normal shock to form and propagate toward the suction surface. At the intersection of the oblique shock (emanating from the pressure surface) and the normal shock (at the bleed slot leading edge) a reflected oblique shock is seen propagating towards the pressure surface. This is the formation of the triple point. A slip stream, dividing supersonic and subsonic flow, is also seen emanating from the triple point. Schlieren photographs of a started cascade (Fig. 50) indicate a similar triple point interaction (Ref. 16).

In order to evaluate the accuracy of the shock structure of Fig. 49, three items are discussed in the remainder of this section. They are as follows:

1. Kantrowitz-Donaldson starting criterion for cascades.
2. Theoretical calculation of the critical velocity

ratio just upstream of the geometric throat.

3. Strength of oblique shock emanating from pressure surface.

The Kantrowitz-Donaldson criterion (Ref. 16) for a cascade is given by the inequality below:

$$\left(\frac{S_*}{g\ \mathrm{Cos}\beta_\infty}\right)_{\text{geometric}} \geq \left(\frac{S_*}{g\ \mathrm{Cos}\beta_\infty}\right)_{\text{isentropic}} \left(\frac{P_{o1}}{P_{oth}}\right) \qquad (7)$$

where: $(\ )_1$ = property just upstream of the throat of Fig. 49

g = pitch of blading

S_* = throat area

β_∞ = flow angle upstream of the cascade with respect to m axis of Fig. 49

P_{oth}/P_{o1} = pressure recovery across a normal shock at the throat of Fig. 49

Inequality 7 represents a necessary condition for an inlet to be started.

Data for use in Inequality 7 are as follows:

$\beta_\infty = 70^\circ$

$\left(\frac{S_*}{g}\right)_{\text{geometric}} = .5378$

$\left(\frac{W}{W_{cr}}\right) = 1.22$

$\left(\frac{W}{W_{cr}}\right)_1 = 1.40$

$\left(\frac{S_*}{g\ \mathrm{Cos}\beta_\infty}\right)_{\text{isentropic}} = \left(\frac{A_*}{A}\right)_\infty = .94509$

$\left(\frac{P_{oth}}{P_{o1}}\right)_1 = .91319$

Based on the above:

$$\left(\frac{S_*}{g\ \mathrm{Cos}\beta_\infty}\right)_{\text{geometric}} = \frac{.5378}{.3420} = 1.5725$$

and $\left(\frac{S_*}{g\ \mathrm{Cos}\beta_\infty}\right)_{\text{isentropic}} \left(\frac{P_{o1}}{P_{th}}\right) = \frac{.94509}{.91319} = 1.3049$

Therefore, according to Inequality 7 the impeller inducer flow is started.

Based on the free-stream critical velocity ratio; i.e., $\left(\frac{W}{W_{cr}}\right)_{\infty} = 1.22$, and the free-streamline trace, the critical velocity ratio $\left(\frac{W}{W_{cr}}\right)_1$ was estimated just upstream of the geometric throat. Fig. 49 shows the free-streamline traced through the leading edges of the pressure and suction surfaces. The free-stream to throat area ratio becomes

$$\frac{A_{\infty}}{A_{th}} = .857.$$

Isentropic expansion from free-stream to the throat produces a critical velocity ratio

$$\left(\frac{W}{W_{cr}}\right)_1 = 1.41$$

and a static to laboratory total pressure ratio

$$\left(\frac{P}{P_{t_i}}\right)_1 = .457$$

These values are in accord with the corresponding parameters of $\left(\frac{W}{W_{cr}}\right)_1 = 1.40$ and $\left(\frac{P}{P_{t_i}}\right)_1 = .40$ computed by VANS and discussed in Sections 6.3.2 and 6.3.3.

Therefore, based on the Kantrowitz-Donaldson criterion and the above theoretical analysis the calculated flow field must be correct just upstream of the throat of the system.

To establish the strength of the oblique shock emanating from the pressure surface leading edge, it is assumed that two-dimensional oblique shock theory holds on the shroud blade-to-blade surface. The effective wedge angle made by the pressure surface leading edge with respect to the incoming flow is $\delta = 11.5^{\circ}$. Wave angle comparisons are made between strong shock theory, weak shock theory and VANS predictions in the forthcoming paragraph.

Based on $\delta = 11.5^{\circ}$ and an incoming critical velocity ratio $\left(\frac{W}{W_{cr}}\right)_1 = 1.41$, the strong and weak shock wave angles θ_w are determined. These angles are compared with the VANS calculated angle in Table 1.

TABLE 1

Comparison of Wave Angles from Theory and Calculation

Computational Mode	$(\frac{W}{W_{cr}})_1$	δ deg	Wave Angle θ_w, deg
Strong Shock Theory	1.41	11.5	75.9
Weak Shock Theory	1.41	11.5	57.0
VANS Calculation	-	-	65.0

It is seen from Table 1 that the VANS calculated wave angle lies between strong shock and weak shock theory. Thus, the calculated shock strength may be correct at the pressure surface leading edge.

6.3.5 Shroud Pressure Comparisons

VANS calculated averaged shroud pressures are compared with measurements and quasi-3-D predictions in Fig. 51. Curve 1 represents the VANS blade-to-blade calculation, Curve 2 represents the VANS cross-sectional calculation, the dashed line corresponds to the quasi-3-D prediction and these data points are measured pressures. Except for the data point just upstream of the bleed slot leading edge, the VANS cross-sectional calculation matches these measured data. The slightly higher measured pressure just upstream of the bleed slot could be attributed to the upstream influence effects of the injection.

The lower blade-to-blade average shroud pressure distribution is a result of the approximate continuity equation employed in the blade-to-blade mode of computation. This technique produces valid pressures in the subsonic domain of the impeller. However, the blade-to-blade pressure gradient is

corrected by the zeroth approximate field and used herein in supersonic domains of flow. Thus, the approximate nature of the blade-to-blade computation is corrected in supersonic regions of the flow.

7.0 CONCLUSIONS AND RECOMMENDATIONS

The VANS successive approximation method has been extended to the computation of 3-D, viscous, transonic flow in turbomachines. A cross-sectional computer code was developed, which conserves mass flux at each point of the cross-sectional surface of computation. Numerical calculations were made for an axial annular turbine cascade and a transonic centrifugal impeller, with splitter vanes and inducer mass injection.

The principal conclusions drawn from this research effort are twofold:

1. The blade-to-blade computer code produces a useful engineering flow field in regions of subsonic relative flow.

2. Cross-sectional computation, with a locally mass flux conservative continuity equation, is required to compute shock waves in regions of supersonic relative flow.

It is recommended that the axial annular turbine cascade problem be completed through meridional and cross-sectional modes of computation. Implementation of these additional computational modes may produce the horseshoe vortices that form on the hub and shroud end walls. Since (1) pressure data exist, (2) laser velocimeter measurements have been taken and more will be taken, and (3) flow visualization experiments have been conducted with this geometry,a quantitative assessment of the VANS computations can be made. Hence, an evaluation of the VANS numerical capability can be made. Furthermore, the effects of the horseshoe vortex on the turbine cascade fluid dynamics can be assessed. A knowledge of horseshoe vortex fluid mechanical effects will eventually lead to more durable turbine designs.

8.0 REFERENCES

1. Katsanis, T., and McNally, W.D., "Revised FORTRAN Program for Calculating Velocities and Streamlines on the Hub-Shroud Mid-Channel Stream Surface of an Axial, Radial, or Mixed Flow Turbo-Machine or Annular Duct," II Programmers Manual, NASA TN D-8431, July 1977.

2. Lubard,S. and Helliwell,W.S., "Calculation of the Flow on a Cone at High Angle of Attack", AIAA Journal, Vol. 12, July 1974, pp. 965-974.

3. Helliwell,W.S.; Dickinson,R.P.; and Lubard,S.C., "Viscous Flow over Arbitrary Geometries at High Angle of Attack", AIAA Journal, Vol. 19, No. 2, February 1981, pp. 191-197.

4. Schiff,L.B. and Steger,J.L., "Numerical Simulation of Steady Supersonic Viscous Flow", AIAA paper 79-0130, 17th Aerospace Sciences Meeting New Orleans, January 1979.

5. Patankar,S.V. and Spalding,D.B., "A Calculation Procedure for Heat, Mass and Momentum Transfer in Three-Dimensional Parabolic Flows", Int. J. Heat Mass Transfer, Vol. 15 pp. 1787-1806, Permagon Press 1972, Great Britain.

6. Briley,W.R. and McDonald,H., "Analysis and Computation of Viscous Subsonic Primary and Secondary Flows", AIAA Paper No. 77-1453, pp. 74-88, Proceedings of Computational Fluid Mechanics Symposium, New Orleans, 1979.

7. Moore,J. and Moore, J.G., "Calculations of Three-Dimensional, Viscous Flow and Wake Development in a Centrifugal Impeller", in "Performance Prediction of Centrifugal Pumps and Compressors", ASME Publication,1980.

8. Moore,J. and Moore,J.G., "Three Dimensional,Viscous Flow Calculations for Assessing the Thermodynamics Performance of Centrifugal Compressors, Study of Eckardt Comparessor", AGARP-CP-282,pp.9-1-9-19,May 1980.

9. Walitt,L.;Harp,J.L.; and Liu,C.Y., "Numerical Calculation of the Internal Flow Field in a Centrifugal Compressor Impeller, NASA CR 134984, December 1975.

10. Walitt,L.;Liu,C.Y.; and Harp,J.L., "An Alternating Direction Explicit Method for Computing Three-Dimensional Viscous Flow Fields in Turbo-machines", SAE Paper No. 781001, Vol. 87 of the 1978 SAE Transactions, pp/ 3829-3854.

11. Walitt,L., "Numerical Analysis of the Three-Dimensional Viscous Flow Field in a Centrifugal Impeller", AGARD-CP-282,pp. 6-1 - 6-29,May 1980.

12. Goldman, L.J. and McLallin, K.L., "Cold-Air Annular-Cascade Investigation of Aerodynamic Performance of Core-Engine-Cooled Turbine Vanes. I-Solid Vane Performance and Facility Description", NASA TM X-3224, 1975.

13. Gaugler,R.E. and Russell,L.M., "Streakline Flow Visualization Study of a Horseshoe Vortex in a Large-Scale, Two-Dimensional Turbine Starter Nozzle", NASA TM 79274, March 1980.

14. Katsanis,T., "FTN Program for Calculating Transonic Velocities on a Blade-to-Blade Stream Surface of a Turbomachine", NASA TN D-5427, 1969.

15. Private communication from T. McKain of Detroit Diesel Allison, October 1980.

16. Chauvin,J.; Sieverding,C.; and Griepentrog,H., "Flow in Cascades with a Transonic Regime," Proceedings of the Symposium of Flow Research on Blading, Baden, Switzerland 1969, pp. 151-196, Elsevier Publishing Company, Amsterdam, 1970.

APPENDIX A

CONTINUOUS INTERPOLATION SCHEME

The interpolation scheme in the VANS computer codes was modified so that interpolated quantities of the previous approximation were continuous in the three dimensional domain of computation. The research was conducted in three phases.

1. An analysis of the interpolation scheme previously embodied in VANS.
2. Adaptation of a continous interpolation scheme for VANS codes.
3. Modification of the interpolation scheme in the VANS computer codes.

Interpolation Scheme Previously Embodied in the VANS/BB Computer Code

After careful study of the VANS numberical data,it was found that the first order double Taylors series employed to interpolate data from the previous approximation field onto the mesh points in either a blade-to-blade or cross-sectional surface produced small oscillations in interpolated quantities.

Consider the point P in (x, y, z) curvilinear space. In each (x,y) blade-to-blade surface, the point P maintains the same axial coordinate (X_3), metrics (hx, hy, hz), metric derivatives $\left(\frac{\partial hx}{\partial y}, \frac{\partial hx}{\partial z}, \frac{\partial hy}{\partial y}, \frac{\partial hy}{\partial z}, \frac{\partial hx}{\partial y}, \frac{\partial hx}{\partial z}\right)$, and axial coordinate drivatives $\left(\frac{\partial x_3}{\partial y}, \frac{\partial x_3}{\partial z}\right)$ independent of the angular coordinate x. In addition the zeroth approximate MERIDL velocities (Ref. 1) at the blade surfaces (W_{ℓ}, Wtr), mean stream surface velocity and angular coordinates (W_m, β_m, α_m) and angular coordinates of the pressure and suction surfaces of the blade (Xg, Xtr) are specified along streamline-like lines in a meridional plane; hence, these data are independent of the angular coordinate x as well. Therefore, the three-dimensional interpolation in (x, y, z) space has been reduced to a two-dimensional interpolation in the (y, z) plane. The angular dependence of the velocity components away from the blades is introduced after the interpolation has taken place.

The previous procedure was to locate the zone in (y,z) space containing point

P (y,z) and interpolate using a first order double Taylor's series. Figure 51 shows the point P located within the zone labelled (1, 2, 3, 4) in (y,z) space. Let V_1, V_2, V_3 be zeroth iterate properties, respectively, at points 1, 2, 3. Using a first order double Taylor's series we get the following relations.

$$V_1 = V_p + \left(\frac{\partial V}{\partial y}\right)_p (y_1 - y) + \left(\frac{\partial V}{\partial z}\right)_p (z_1 - z) \qquad \text{(A1)}$$

$$V_2 = V_p + \left(\frac{\partial V}{\partial y}\right)_p (y_2 - y) + \left(\frac{\partial V}{\partial z}\right)_p (z_2 - z) \qquad \text{(A2)}$$

$$V_3 = V_p + \left(\frac{\partial V}{\partial y}\right)_p (y_3 - y) + \left(\frac{\partial V}{\partial z}\right)_p (z_3 - z) \qquad \text{(A3)}$$

Equations (A1, A2, and A3) can be solved simultaneously for V_p. We then repeat the procedure for points (2, 3, 4),(3, 4, 1), and (4, 1, 2). The value of V at point P is then the arithmetic average of the above.

The above procedure is continous as long as the point P remains within or on the boundary of zone (1, 2, 3, 4). However, as the blade-to-blade surface moves from hub to shroud the point P could cross the zone boundaries and be contained by another zone. After the point P crosses a zone boundary, two of the four end points of the new zone will be different. This introduces a discontinuity in the property V_p after point P crosses a boundary. These discontinuities caused fluctuations in the source terms of the equations of motion, which in turn produced the small oscillations recorded in the annular cascade flow field.

Revised Interpolation Scheme for VANS/BB

The continuous interpolation scheme developed by Katsanis (Ref. 1) was selected for incorporation into the VANS computer codes.

The Katsanis scheme for interpolation is quite simple for a rectangular zone (1, 2, 3, 4) located in the (y, z) plane containing the point P (y,z) (Figure 52b). We first form the numerical derivatives

$$f_z = (z - z_2)/(z_3 - z_2) \qquad \text{(A4)}$$

$$f_y = (y - y_2)/(y_1 - y_2) \qquad \text{(A5)}$$

Linear interpolations are then conducted with f_y to find V at the points 1 and 3 of Figure 52b.

$$V_{\underline{1}} = V_2 + fy\ (V_1 - V_2) \qquad (A6)$$

$$V_{\underline{3}} = V_3 + fy\ (V_4 - V_3) \qquad (A7)$$

A linear interpolation with f_z determines the property V_p

$$V_p = V_{\underline{1}} + fz\ (V_{\underline{3}} - V_{\underline{1}}) \qquad (A8)$$

Equations A6, A7, and A8 can be combined to determine V_p directly in terms of f_y and f_z.

$$V_p = V_1\ fy\ (1-fz) + V_2(1-fy)(1-fz) + V_3 fz(1-fy) + V_4 fyfz \qquad (A9)$$

Equation A9 reduces to a linear interpolation along any boundary line of the zone (1, 2, 3, 4). Therefore, this linear, two-dimensional interpolation scheme produces a continuous interpolated variable V_p.

Although the above interpolation scheme is quite simple to implement, a fairly extensive coding effort was required to revise the VANS/BB computer code.

Linear Continuous Interpolation Scheme Incorporated into Existing Versions of VANS/BB and VANS/CS Computer Codes

The Katsanis 2-D linear continuous interpolation scheme, called "LININT", was coded and incorporated into the present versions of the VANS computer codes. The axial annular turbine cascade problem (Section 5.0) was utilized to debug this coding.

Table 1 presents a comparison of interpolated zeroth approximation flow field quantities based on a Taylors series interpolation and the LININT interpolation.

These data corresond to a blade-to-blade surface just above the hub, i.e., at a z coordinate of .4000000-05 radians, and at a point on the surface having an axial coordinate X_3 of .3051584-01 ft. and a radial coordinate h_x of .708330 ft.

The MERIDL blade-to-blade surfaces bounding the above blade-to-blade surface have z coordinates of 0.0 and .10236-01 radians, respectively.

TABLE 1

Comparison of Taylor Series and LININT Interpolation Schemes

z = .40000000-05 radians

X_3 = .3051584-01 ft.

hx = .708330 ft.

Variable	Units	Taylor Series Interpolation	LININT Interpolation
hy	ft/rad	.833333	.833333
h_z	ft/rad	.4884698	.4884698
X_3/ y	ft/rad	.833333	.833333
X_3/ z	ft/rad	0.0	0.0
hx/ y	ft/rad^2	0.0	0.0
hx/ z	ft/rad^2	.4884698	.4884698
hy/ y	ft/rad^2	-.2095527-10	-.2095527-10
hy/ z	ft/rad^2	0.0	0.0
hz/ y	ft/rad^2	0.0	0.0
hz/ z	ft/rad^2	-.1666937	-.1666937
X	radians	-.6356348-01	-.6356348-01
Xtr	radians	.5189184-01	.5189184-01
Wm	ft/sec	.3761843+03	.3761844+03
m	radians	-.3102789	-.3102790
m	radians	-.1328640-05	-.1328640-05
W	ft/sec	.6185929+03	.6185930+03
Wtr	ft/sec	.1337685+03	.1337686+03

It is seen from Table 1 that corresponding quantities are almost identical. This is true because the point in question lies within the same zone in (y,z) space. Where the blade-to-blade surface moves to just above z = .10236-01 radians significant differences between the two methods of interpolation will exist.

APPENDIX B

QUADRILATERAL WEDGE FORCE BALANCE

In order to increase the accuracy and degree of continuity of dependent variables computed by VANS, the method of calculation of forces was revised. The force balance previously embodied in VANS considers the three dimensional computational element as an equivalent quadrilateral slab. Actually the geometric figure is a wedge shaped quadrilateral. A discussion of the original method of force calculation and the revised method of force calculation follows.

The original method of force calculation considers the computational element as an equivalent quadrilateral slab. Let us consider the three dimensional element of Fig. 53 in cartesian (X_1, X_2, X_3) space with X_3 being the axial direction. This figure shows half of the computational element, i.e., the z-curvilinear dimension is $\Delta z/2$, and divides the (x,y) blade-to-blade surface labeled 2, 3, 4, 5, 6, 7, 8, 9 into four quadrilateral zones (solid lines) and one momentum zone (dashed line). The four quadrilateral zones are labeled by the letters a, b, c, and d, respectively. The momentum zone is labeled by the number 1. The stress tensor is defined in each of the quadrilateral zones and is labeled by the letter defining that zone. For example σ_a is the stress tensor of quadrilateral zone a. To determine the force on Momentum zone 1, we simply contract the appropriate stress tensor with the areas of Momentum zone 1. This method of force calculation is second order accurate and internally consistent.* To the knowledge of the author of this submittal, this method of force calculation is the only one known that exhibits both properties.

---

*Internal consistency implies that the finite difference continuity, momentum, and internal energy relations imply an exact finite difference conservation of total energy equation.

According to the momentum equations of Reference 10, the three components of force for Momentum zone 1 are evaluated from the following integrals:

$$F_{x_1} = \int_c \mathbb{T}_x \cdot \underline{n}\, dc \qquad \text{(B1)}$$

$$F_{y_1} = \int_c \mathbb{T}_y \cdot \underline{n}\, dc \qquad \text{(B2)}$$

$$F_{z_1} = \int_c \mathbb{T}_z \cdot \underline{n}\, dc \qquad \text{(B3)}$$

where

$$\mathbb{T}_x = \sigma_{xx}\, hyhz\, \underline{i} + \tau_{xy}\, hx\, hz\, \underline{j}$$

$$\mathbb{T}_y = \tau_{xy}\, hyhz\, \underline{i} + \sigma_{yy}\, hx\, hz\, \underline{j}$$

$$\mathbb{T}_z = \tau_{zx}\, hyhz\, \underline{i} + \tau_{zy}\, hx\, hz\, \underline{j}$$

and where c is the perimeter a, b, c, d of Fig. 53, $\underline{n}$ is a unit normal to the curve c, (hx, hy, hz) are the metrics of the transformation, (i,j) are unit basis vectors for curvilinear coordinates (x,y) respectively (xx, yy) are normal stresses, and (xy, zx, zy) are shear stresses. Equations (B1) - (B3) define forces only within the (x,y) blade-to-blade surface. Contributions of the wedge face areas of Fig. 53 to the force acting on Momentum zone 1 are evaluated from different terms of the equations of motion.

Under the approximation that the geometry of Fig. 53 is approximately a quadrilateral slab, the finite difference approximation to integral Equations (B1) and (B2) becomes

$$\underline{F}_1 = -\underline{Fa} - \underline{Fb} + \underline{Fc} + \underline{Fd} \qquad \text{(B4)}$$

where

$$\underline{Fa} = \frac{\mathbb{T}_a}{2} \cdot \underline{A}_{21}$$

$$\underline{Fb} = \frac{\mathbb{T}_b}{2} \cdot \underline{A}_{46}$$

$$\underline{Fc} = \frac{\mathbb{T}_c}{2} \cdot \underline{A}_{86}$$

$$\underline{Fd} = \frac{\mathbb{T}_d}{2} \cdot \underline{A}_{28}$$

and where the finite difference contribution of the wedge face areas to the force acting on Momentum zone 1, i.e. $\underline{Fw}_1$, appears elsewhere. The vector area $\underline{A}_{24}$ is defined in terms of the curvilinear coordinates x, y, z and their metrics as follows:

$$\underline{A}_{24} = \begin{pmatrix} (y_2-y_4)\ hy_{24}hz_{24} \\ -(x_2-x_4)\ hx_{24}hz_{24} \end{pmatrix}$$

where the upper term of the vector is the x component and the lower term of the vector is the y component.

For the case where quadrilateral 1, 2, 3, 4 is a slab, i.e., the wedge faces are parallel, it can be shown that

$$\underline{A}_{24} = -2\ (\underline{A}_{ad} + \underline{A}_{aa}) \qquad \text{(B5)}$$

Similar results apply for vector areas $\underline{A}_{46}$, $\underline{A}_{86}$, and $\underline{A}_{28}$. However, quadrilateral 1, 2, 3, 4 is not a slab and Equation (B5) is approximate, with the degree of accuracy becoming higher as one moves away from the axis of the system. In fact for the case where $\sigma_a=\sigma_b=\sigma_c=\sigma_d=$ pressure (p), the force balance of Equation B4 coupled with the wedge face force terms in the equations of motion do not go identically to zero. A small force balance residual occurs which diminishes as one moves away from the axis.

In order to rectify the above, the computational element was considered a quadrilateral wedge for purposes of formulating the force balance. A schematic of the three dimensional computational element illustrating the quadrilateral wedge force balance is showin in Figure 54. The quadrilateral force balance becomes

$$\underline{F}_1 = \underline{F}_a + \underline{F}_b + \underline{F}_c + \underline{F}_d \qquad \text{(B6)}$$

where

$$\underline{Fa} = \sigma_a \cdot (\underline{A}\,\underline{1d} + \underline{Aa1} + \frac{1}{4}\,\underline{Awa})$$
$$\underline{Fb} = \sigma_b \cdot (\underline{Ab1} + \underline{A1a} + \frac{1}{4}\,\underline{Awb}) \qquad \text{(B7)}$$
$$\underline{Fc} = \sigma_c \cdot (\underline{A1b} + \underline{Ac1} + \frac{1}{4}\,\underline{Awc})$$
$$\underline{Fd} = \sigma_d \cdot (\underline{A1c} + \underline{Ad1} + \frac{1}{4}\,\underline{Awd})$$

and where the areas $\underline{A1d}$ and $\underline{Aa1}$ are defined in terms of the following vectors:

$$\underline{A1d} = \begin{pmatrix} (y_1 - y_{\underline{d}}) & hy_{\underline{1d}} & hz_{\underline{1d}} \\ -(x_1 - x_{\underline{d}}) & hx_{\underline{1d}} & hz_{\underline{1d}} \end{pmatrix} = \begin{pmatrix} Ax_{\underline{1d}} \\ Ay_{\underline{1d}} \end{pmatrix} \qquad \text{(B8)}$$

$$\underline{Aa1} = \begin{pmatrix} (y_{\underline{a}} - y_1) & hy_{\underline{a1}} & hz_{\underline{a\_1}} \\ -(x_{\underline{a}} - x_1) & hx_{\underline{a1}} & hz_{\underline{a1}} \end{pmatrix} = \begin{pmatrix} Ax_{\underline{a1}} \\ Ay_{\underline{a1}} \end{pmatrix} \qquad \text{(B9)}$$

The upper terms of the above vectors represent the x component, while the lower terms represent they y component. Finally, the wedge face areas are defined in terms of the planar areas as follows:

$$\underline{Awa} = (-2(A_{y1\underline{d}} + A_{y\underline{a}1} + A_{y\underline{d}2} + A_{y2\underline{2}})) \qquad \text{(B10)}$$

with similar expressions for $\underline{Awb}$, $\underline{Awc}$, and $\underline{Awd}$. Equation(B10) is based on the following geometric relations:

$$\left.\begin{aligned} A_{y2\underline{2}} &= A_{y\underline{23}} \\ A_{y\underline{a}1} &= A_{y4\underline{9}} \\ A_{x1\underline{d}} &= A_{x\underline{d}2} = A_{x4\underline{3}} = A_{x\underline{33}} \end{aligned}\right\} \qquad \text{(B11)}$$

The points $\underline{a}$, $\underline{d}$, $\underline{2}$, and $\underline{3}$ were selected to satisfy Equations (B11).

For the case where $\sigma_a = \sigma_b = \sigma_c = \sigma_d = p$, the vector areas of Equations (B7) cancel, i.e., $\underline{A}_{1\underline{d}} + \underline{A}_{\underline{d}1} = 0$, etc. Thus, only the wedge face contribution to the force on Momentum zone 1 remain.

$$\underline{F}_1 = P/4\ (\underline{Awa} + \underline{Awb} + \underline{Awc} + \underline{Awd}) \qquad \text{(B12)}$$

Equation (B12) is in turn cancelled by the remaining wedge face terms in the equations of motion. Therefore, for the hydrostatic case the overall force balance for Momentum zone 1 is zero.

The quadrilateral force balance logic was incorporated into the blade-to-blade VANS computer code and the cross-sectional VANS computer code.

APPENDIX C

INTEGRAL CONTINUITY MOMENTUM AND SPECIFIC INTERNAL ENERGY RELATIONS IN GENERALIZED COORDINATES FOR BLADE-TO-BLADE MODE OF COMPUTATION

Continuity

$$\frac{\partial}{\partial t}\int_A \rho h_x h_y dA + \int_C \rho(\underline{q}-\underline{q}_s)\cdot\underline{n}dC - \frac{1}{U_z}\int_C \rho w' \underline{q}_s\cdot\underline{n}dC = -\frac{1}{U_z}\frac{\partial}{\partial t}\int_A \tilde{\rho}\tilde{w}' h_x h_y dA \tag{C1}$$

where

$$\underline{q} = uh_y h_z \underline{i} + vh_x h_z \underline{j}$$

$$\underline{q}_s = S_x h_x h_y \underline{i} + S_y h_y h_x \underline{j}$$

$$z = U_z t$$

$$w' = w - U_z$$

Internal Energy Equation

$$\begin{aligned}
&\frac{\partial}{\partial t}\int_A \rho E h_x h_y dA + \int_C \rho E(\underline{q}-\underline{q}_s)\cdot\underline{n}dC - \int_C \rho E w' \underline{q}_s\cdot\underline{n}dC = -\frac{1}{U_z}\frac{\partial}{\partial t}\int_A \tilde{\rho}\tilde{E}\tilde{w}' h_x h_y dA \\
&+ \frac{1}{U_z}\left\{\sigma_{zz}\frac{\partial}{\partial t}\int_A \tilde{w} h_x h_y dA + \tau_{yz}\frac{\partial}{\partial t}\int_A \tilde{v} h_x h_y dA + \tau_{zx}\frac{\partial}{\partial t}\int_A \tilde{u} h_x h_y dA\right\} \\
&- \frac{1}{U_z}\left\{\sigma_{zz}\int_C w\underline{q}_s\cdot\underline{n}dC + \tau_{yz}\int_C v\underline{q}_s\cdot\underline{n}dC + \tau_{zx}\int_C u\underline{q}_s\cdot\underline{n}dC\right\} + \int_A h_x h_y h_z \pi_E dA + \int_A \pi_{Ep} dA \\
&+ \int_C \bar{\sigma}_p \underline{n}\cdot\underline{q}dC + \int_C \tau_p \underline{n}\cdot\underline{q}_\tau dC + \int_C \tau_{pz}\underline{n}\cdot\underline{q}_{\tau z}dC
\end{aligned} \tag{C2}$$

where

$$\pi_E = \sigma_{xx}\left|\frac{v}{h_x h_y}\frac{\partial h_x}{\partial y} + \frac{w}{h_x h_z}\frac{\partial h_x}{\partial z}\right|$$

$$+ \sigma_{yy}\left|\frac{w}{h_y h_z}\frac{\partial h_y}{\partial z} + \frac{u}{h_x h_y}\frac{\partial h_y}{\partial x}\right|$$

$$+ \sigma_{zz}\left|\frac{u}{h_x h_z}\frac{\partial h_z}{\partial x} + \frac{v}{h_y h_z}\frac{\partial h_z}{\partial y}\right|$$

$$- \tau_{xy}\left|\frac{v}{h_x h_y}\frac{\partial h_y}{\partial x} + \frac{u}{h_x h_y}\frac{\partial h_x}{\partial y}\right|$$

$$- \tau_{zx}\left|\frac{u}{h_z h_x}\frac{\partial h_x}{\partial z} + \frac{w}{h_z h_x}\frac{\partial h_z}{\partial x}\right|$$

$$- \tau_{yz}\left|\frac{w}{h_z h_y}\frac{\partial h_z}{\partial y} + \frac{v}{h_z h_y}\frac{\partial h_y}{\partial z}\right|$$

$$\pi_{Ep} = -[\sigma_{zz}w + \tau_{yz}v + \tau_{zx}u]\frac{\partial(h_x h_y)}{\partial z}$$

$$-[\sigma_{xx}u + \tau_{xy}v + \tau_{zx}w]\frac{\partial(h_y h_z)}{\partial x}$$

$$-[\sigma_{yy}v + \tau_{xy}u + \tau_{yz}w]\frac{\partial(h_x h_z)}{\partial y}$$

$$\bar{\sigma}_p = \begin{pmatrix} \sigma_{xx} & 0 \\ 0 & \sigma_{yy} \end{pmatrix}$$

$$\tau_p = \begin{pmatrix} 0 & \tau_{xy} \\ \tau_{xy} & 0 \end{pmatrix}$$

$$\tau_{pz} = \begin{pmatrix} 0 & \tau_{zy} \\ \tau_{zx} & 0 \end{pmatrix}$$

$$\underline{q}_\tau = uh_x h_z \underline{i} + vh_y h_z \underline{j}$$

$$\underline{q}_{\tau z} = wh_x h_z \underline{i} + wh_y h_z \underline{j}$$

Equation of State

$$P = (\gamma - 1)\rho E \tag{C3}$$

x-direction momentum

$$\begin{aligned}
&\frac{\partial}{\partial t}\int_A \rho u h_x h_y dA + \int_C \rho u(\underline{q}-\underline{q}_s)\cdot\underline{n}dC \\
&+\int_A h_x h_y h_z A_x dA - \frac{1}{U_z}\int_C \rho uw'\underline{q}_s\cdot\underline{n}dC \\
&= -\frac{1}{U_z}\frac{\partial}{\partial t}\int_A \rho\bar{u}\bar{w}' h_x h_y dA \\
&+ \frac{1}{U_z}\frac{\partial}{\partial t}\int_A \tau_{zx} h_x h_y dA \\
&- \frac{1}{U_z}\int_C \tau_{zx}\underline{q}_s\cdot\underline{n}dC + \int_A h_x h_y h_z \pi_x dA \\
&+ \int_C \bar{\sigma}_{p_x}\cdot\underline{n}dC
\end{aligned} \tag{C4}$$

where

$$\begin{aligned}
A_x &= \frac{\rho u}{h_x}\left\{\frac{u}{h_x}\frac{\partial h_x}{\partial x} + \frac{v}{h_y}\frac{\partial h_x}{\partial y} + \frac{w}{h_z}\frac{\partial h_z}{\partial z}\right\} \\
&- \frac{\rho}{h_x}\left\{\frac{u^2}{h_x}\frac{\partial h_x}{\partial x} + \frac{v^2}{h_y}\frac{\partial h_y}{\partial x} + \frac{w^2}{h_z}\frac{\partial h_z}{\partial x}\right\} \\
&+ 2\rho\omega\left(\frac{w}{h_y}\frac{\partial X_3}{\partial y} - \frac{v}{h_z}\frac{\partial X_3}{\partial z}\right) \\
&- \frac{\rho\omega^2}{h_x}\left(\frac{\partial X_1}{\partial x}X_1 + \frac{\partial X_2}{\partial x}X_2\right)
\end{aligned}$$

$$\begin{aligned}
\pi_x &= \frac{\tau_{xy}}{h_x h_y}\frac{\partial h_x}{\partial y} + \frac{\tau_{zx}}{h_x h_z}\frac{\partial h_x}{\partial z} \\
&- \frac{\sigma_{yy}}{h_x h_y}\frac{\partial h_y}{\partial x} - \frac{\sigma_{zz}}{h_x h_z}\frac{\partial h_z}{\partial x}
\end{aligned}$$

$$\bar{\sigma}_{p_x} = \sigma_{xx} h_y h_z \underline{i} + \tau_{yx} h_x h_z \underline{j}$$

y-Direction Momentum

$$\frac{\partial}{\partial t}\int_A \rho v h_x h_y dA + \int_C \rho v(\underline{q}-\underline{q}_s)\cdot\underline{n}dC$$

$$+ \int_A h_x h_y h_z A_y dA - \frac{1}{U_z}\int_C \rho v w' \underline{q}_s \cdot \underline{n} dC$$

$$= -\frac{1}{U_z}\frac{\partial}{\partial t}\int_A \overline{\rho v w}' h_x h_y dA$$

$$+ \frac{1}{U_z}\frac{\partial}{\partial t}\int_A h_x h_y \overline{\tau}_{zy} dA - \frac{1}{U_z}\int_C \tau_{zy}\underline{q}_s\cdot\underline{n}dC \qquad \text{(C5)}$$

$$+ \int_A h_x h_y h_z \pi_y dA + \int_C \overline{\sigma}_{p_y}\cdot\underline{n}dC$$

where

$$A_y = \frac{\rho v}{h_y}\left\{\frac{u}{h_x}\frac{\partial h_y}{\partial x} + \frac{v}{h_y}\frac{\partial h_y}{\partial y} + \frac{w}{h_z}\frac{\partial h_z}{\partial z}\right\}$$

$$- \frac{\rho}{h_y}\left\{\frac{u^2}{h_x}\frac{\partial h_x}{\partial y} + \frac{v^2}{h_y}\frac{\partial h_y}{\partial y} + \frac{w^2}{h_z}\frac{\partial h_z}{\partial y}\right\}$$

$$+ 2\rho\omega\left(\frac{u}{h_z}\frac{\partial X_3}{\partial z} - \frac{w}{h_x}\frac{\partial X_3}{\partial x}\right)$$

$$- \frac{\rho\omega^2}{h_y}\left(X_1\frac{\partial X_1}{\partial y} + X_2\frac{\partial X_2}{\partial y}\right)$$

$$\pi_y = \frac{\tau_{yz}}{h_y h_z}\frac{\partial h_y}{\partial z} + \frac{\tau_{xy}}{h_x h_y}\frac{\partial h_y}{\partial x} - \frac{\sigma_{zz}}{h_y h_z}\frac{\partial h_z}{\partial y}$$

$$- \frac{\sigma_{xx}}{h_x h_y}\frac{\partial h_x}{\partial y}$$

$$\overline{\sigma}_{p_y} = h_y h_z \tau_{xy}\underline{i} + h_x h_z \sigma_{yy}\underline{j}$$

z-Direction Momentum

$$\frac{\partial}{\partial t}\int_A \rho w h_x h_y dA + \int_C \rho w(\underline{q}-\underline{q}_s)\cdot\underline{n}dC$$

$$+\int_A h_x h_y h_z A_z dA - \frac{1}{U_z}\int \rho ww'\underline{q}_s\cdot\underline{n}dC$$

$$= -\frac{1}{U_z}\frac{\partial}{\partial t}\int_A \overline{\rho ww}' h_x h_y dA$$

$$+\frac{1}{U_z}\frac{\partial}{\partial t}\int_A h_x h_y \overline{\sigma}_{zz} dA - \frac{1}{U_z}\int_C \sigma_{zz}\underline{q}_s\cdot\underline{n}dC$$

$$+\int_A h_x h_y h_z \pi_z dA + \int_C \overline{\sigma}_{p_z}\cdot\underline{n}dC \qquad (C6)$$

where

$$A_z = \frac{\rho w}{h_z}\left\{\frac{u}{h_x}\frac{\partial h_z}{\partial x} + \frac{v}{h_y}\frac{\partial h_z}{\partial y} + \frac{w}{h_z}\frac{\partial h_z}{\partial z}\right\}$$

$$- \frac{\rho}{h_z}\left\{\frac{u^2}{h_x}\frac{\partial h_x}{\partial z} + \frac{v^2}{h_y}\frac{\partial h_y}{\partial z} + \frac{w^2}{h_z}\frac{\partial h_z}{\partial z}\right\}$$

$$+ 2\rho\omega\left(\frac{v}{h_x}\frac{\partial X_3}{\partial x} - \frac{u}{h_y}\frac{\partial X_3}{\partial y}\right)$$

$$- \frac{\rho\omega^2}{h_z}\left(X_1\frac{\partial X_1}{\partial z} + X_2\frac{\partial X_2}{\partial z}\right)$$

$$\pi_z = \frac{\tau_{zx}}{h_x h_z}\frac{\partial h_z}{\partial x} + \frac{\tau_{yz}}{h_z h_y}\frac{\partial h_z}{\partial y} - \frac{\sigma_{xx}}{h_z h_x}\frac{\partial h_x}{\partial z}$$

$$- \frac{\sigma_{yy}}{h_z h_y}\frac{\partial h_y}{\partial z}$$

$$\overline{\sigma}_{p_z} = h_y h_z \tau_{zx}\underline{i} + h_z h_x \tau_{yz}\underline{j}$$

APPENDIX D

MASS FLUX CONSERVATIVE INTEGRAL EQUATIONS OF MOTION

z-Direction Momentum

$$\frac{1}{U_z^2}\frac{\partial}{\partial t}\int_A \rho w w h_x h_y dA + \int_C \rho w(\underline{q}-\underline{q}_s)\cdot\underline{n}dC + \int_A h_x h_y h_z A_z dA - \frac{1}{U_z}\int \rho w w' \underline{q}_s \cdot \underline{n} dC$$

$$= \frac{1}{U_z}\frac{\partial}{\partial t}\int_A h_x h_y \tilde{\sigma}_{zz} dA - \frac{1}{U_z}\int_C \sigma_{zz}\underline{q}_s \cdot n dC + \int_A h_x h_y h_z \pi_z dA + \int_C \bar{\sigma} p_z \cdot \underline{n} dC \quad \text{(D1)}$$

Continuity

$$\frac{1}{U_z}\frac{\partial}{\partial t}\int_A \rho w h_x h_y dA + \int_C \rho(\underline{q}-\underline{q}_s)\cdot\underline{n}dC - \frac{1}{U_z}\int_C \rho w' \underline{q}_s \cdot \underline{n} dC = 0 \quad \text{(D2)}$$

$$w = \frac{(\rho ww)_{z\ \text{momentum}}}{(\rho w)_{\text{continuity}}} \quad \text{(D3)}$$

$$\rho = \frac{(\rho w)\ \text{continuity}}{w} \quad \text{(D4)}$$

Internal Energy Equation

$$\frac{1}{U_z}\frac{\partial}{\partial t}\int_A \rho w h_x h_y E\,dA + \int_C \rho E(\underline{q}-\underline{q}_s)\cdot\underline{n}\,dC$$

$$-\int_C \rho E w'\underline{q}_s\cdot\underline{n}\,dC =$$

$$+\frac{1}{U_z}\left\{\sigma_{zz}\frac{\partial}{\partial t}\int_A \tilde{w}h_x h_y\,dA + \tau_{yz}\frac{\partial}{\partial t}\int_A \tilde{v}h_x h_y\,dA + \tau_{zx}\frac{\partial}{\partial t}\int_A \tilde{u}h_x h_y\,dA\right\}$$

$$-\frac{1}{U_z}\left\{\sigma_{zz}\int_C w\underline{q}_s\cdot\underline{n}\,dC + \tau_{yz}\int_C v\underline{q}_s\cdot\underline{n}\,dC + \tau_{zx}\int_C u\underline{q}_s\cdot\underline{n}\,dC\right\} + \int_A h_x h_y h_z \pi_E\,dA + \int_A \pi_{Ep}\,dA$$

$$+\int_C \bar{\sigma}_p\underline{n}\cdot\underline{q}\,dC + \int_C \tau_p\underline{n}\cdot\underline{q}_\tau\,dC + \int_C \tau_{pz}\underline{n}\cdot\underline{q}_{\tau z}\,dC \qquad (D5)$$

Equation of State

$$P = (\gamma-1)\rho E \qquad (D6)$$

x-Direction Momentum

x-direction momentum

$$\frac{1}{U_z}\frac{\partial}{\partial t}\int_A \rho w h_x h_y u\,dA + \int_C \rho u(\underline{q}-\underline{q}_s)\cdot\underline{n}\,dC$$

$$+\int_A h_x h_y h_z A_x\,dA - \frac{1}{U_z}\int_C \rho u w'\underline{q}_s\cdot\underline{n}\,dC$$

$$= \frac{1}{U_z}\frac{\partial}{\partial t}\int_A \tilde{\tau}_{zx} h_x h_y\,dA \qquad (D7)$$

$$-\frac{1}{U_z}\int_C \tau_{zx}\underline{q}_s\cdot\underline{n}\,dC + \int_A h_x h_y h_z \pi_x\,dA$$

$$+\int_C \bar{\sigma}_{p_x}\cdot\underline{n}\,dC$$

y-Direction Momentum

$$\frac{1}{U_z}\frac{\partial}{\partial t}\int_A \rho w h_x h_y V\, dA + \int_C \rho v(\underline{q}-\underline{q}_s)\cdot\underline{n}\,dC$$

$$+ \int_A h_x h_y h_z A_y\, dA - \frac{1}{U_z}\int_C \rho v w' \underline{q}_s\cdot\underline{n}\,dC$$

$$= \frac{1}{U_z}\frac{\partial}{\partial t}\int_A h_x h_y \vec{\tau}_{zy}\, dA - \frac{1}{U_z}\int_C \tau_{zy}\underline{q}_s\cdot\underline{n}\,dC$$

$$+ \int_A h_x h_y h_z \pi_y\, dA + \int_C \vec{\sigma}_{p_y}\cdot\underline{n}\,dC$$

(D8)

APPENDIX E

MASS FLUX CONSERVATION PROPERTY ILLUSTRATION

In order to develop the mass flux-conservative VANS cross-sectional code, a sample problem was run for debug purposes.

A centrifugal impeller was selected for which the blade-to-blade solution was known. Input conditions for the impeller are as follows:

rotational speed = 33620 rpm

tip speed = 420 m/sec

passage mass flux = .0410 kilograms/sec

The cross-sectional code was run two hundred cycles starting at a station upstream of the blading. Then the code was run through the blade leading edge starting from a station just upstream of the leading edge. Table 1 presents the integrated passage mass-flux on two cross-sections upstream of the blading, a cross-section at the blade leading edge, and at two cross-sections just downstream of the blade leading edge. The parameter $\tilde{z}$ represents the ratio of the distance along the hub to the hub distance between blades. Negative values represent distance upstream of the blades.

TABLE 1

Passage Mass-Flux Evaluation At Four Cross-Sectional Surfaces

$\tilde{z}$	$\dot{m}$	Percent Difference From Incoming Mass-Flow
-.3994	.0410	0
-.3461	.0410	0
-.0077	.0410	0
.0988	.0406	-.97
.1024	.0406	-.97

It is seen from Table 1 that for $\tilde{z}$ parameters upstream of the blading the mass-flux is exactly conserved. As the cross-section passes through the blade leading edge, i.e., between $\tilde{z} = -.0077$ and $\tilde{z} = .0988$, the mass flux decreases by .97 percent. When the cross-section is within the blading, i.e., for $\tilde{z} > .0988$, the mass flux is again exactly conserved. The small mass flux deviation through the blade leading edge comes from the blade thickness. The lateral boundary between the suction surface blade tip and shroud is slightly different than the corresponding lateral boundary between the pressure surface blade tip and shroud.

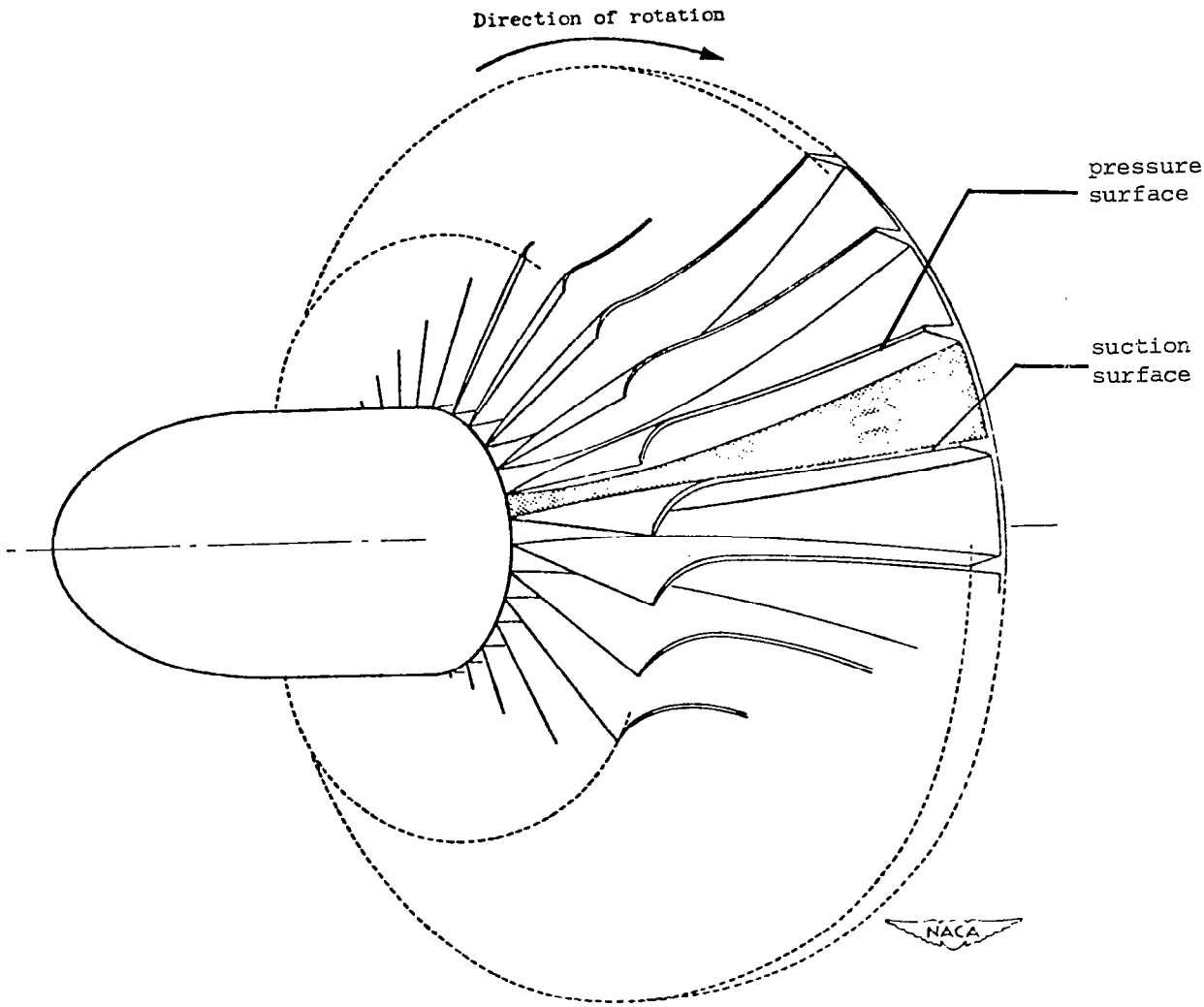

Figure 1. Passage between blades in an impeller of a typical compressor.

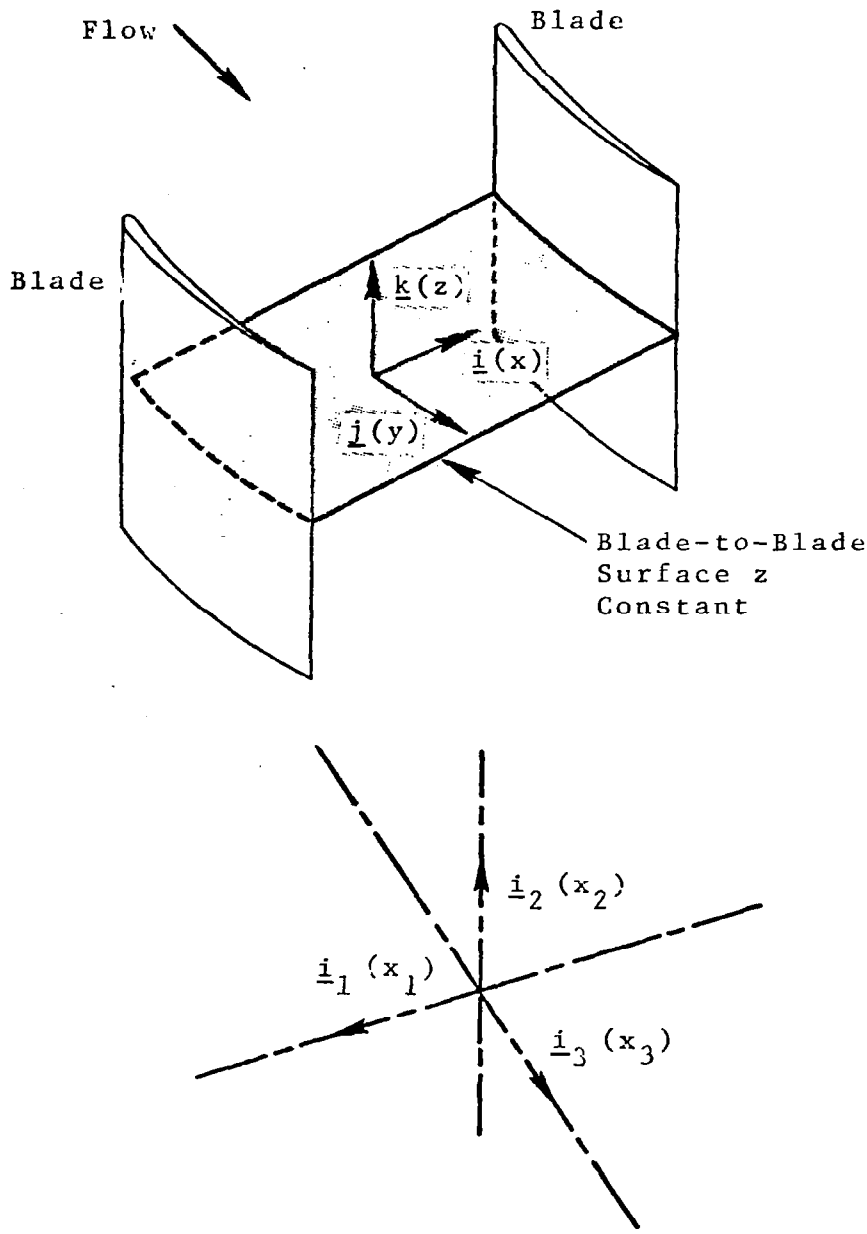

Fig. 2 Schematic of rotor blading passage illustrating the blade-to-blade mode of marching.

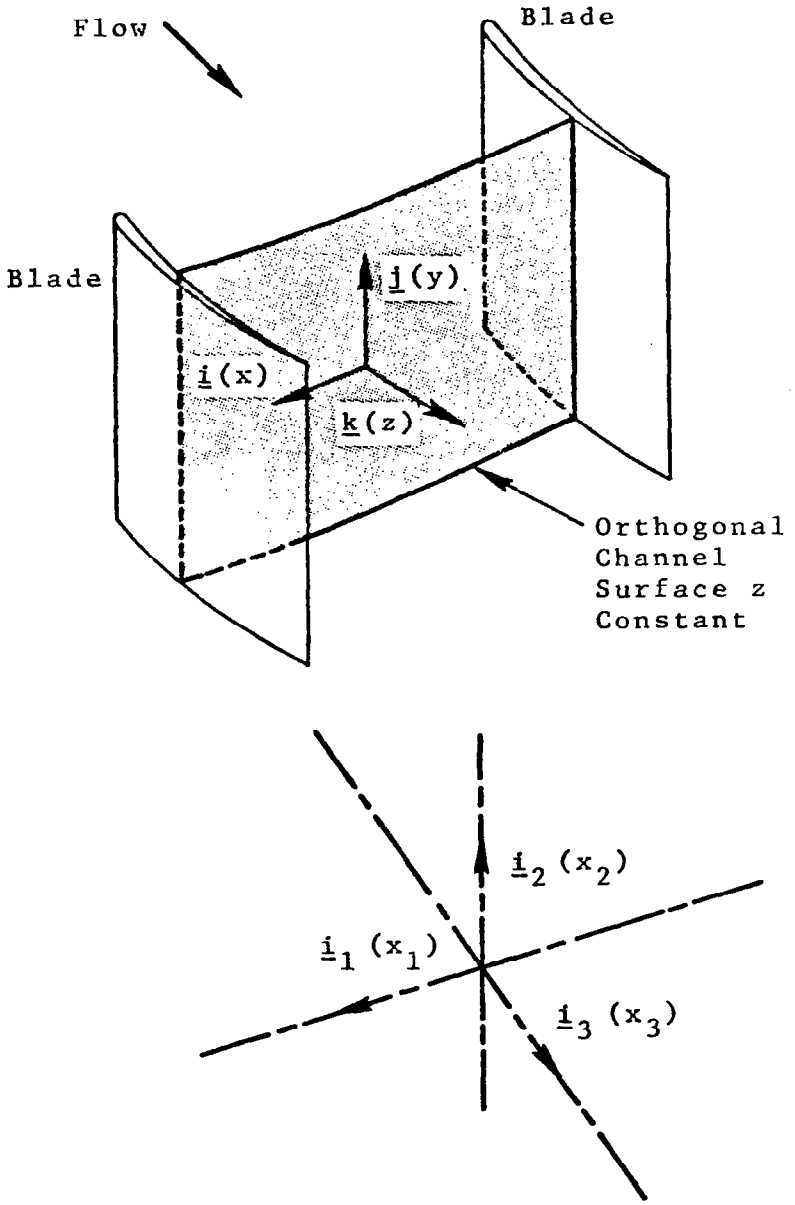

Fig. 3 Schematic of rotor blading passage illustrating cross-sectional mode of marching.

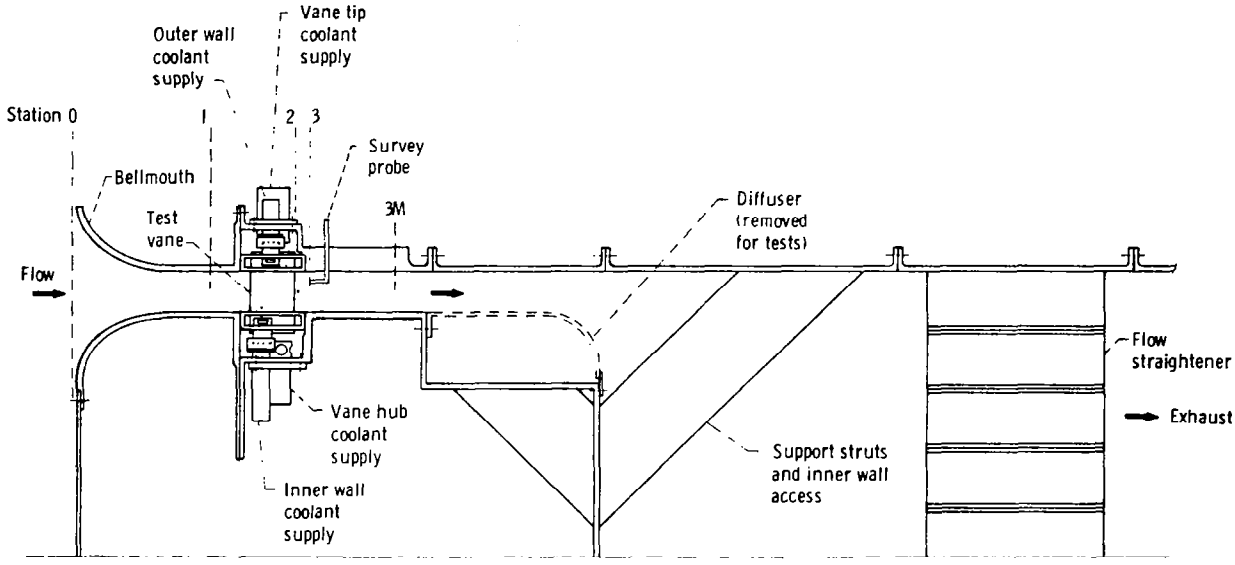

Figure 4 Schematic cross-sectional view of axial annular cascade experimental setup; outer annular radius of 10.0 inches and inner annular radius of 8.5 inches.

X		Y_L		Y_U	
cm	in.	cm	in.	cm	in.
0	0	0.508	0.200	0.508	0.200
0.127	0.050	-----	-----	.851	.335
.254	.100	-----	-----	1.003	.395
.381	.150	-----	-----	1.120	.441
.508	.200	-----	-----	1.212	.477
.635	.250	-----	-----	1.285	.506
.762	.300	.061	.024	1.341	.528
.889	.350	.117	.046	1.389	.547
1.016	.400	.163	.064	1.425	.561
1.143	.450	.201	.079	1.448	.570
1.270	.500	.236	.093	1.463	.576
1.397	.550	.267	.105	1.471	.579
1.524	.600	.292	.115	1.476	.581
1.778	.700	.328	.129	1.461	.575
2.032	.800	.358	.141	1.427	.562
2.286	.900	.376	.148	1.377	.542
2.540	1.000	.384	.151	1.321	.520
2.794	1.100	.381	.150	1.255	.494
3.048	1.200	.368	.145	1.191	.469
3.302	1.300	.353	.139	1.110	.437
3.556	1.400	.328	.129	1.026	.404
3.810	1.500	.297	.117	.942	.371
4.064	1.600	.262	.103	.848	.334
4.318	1.700	.221	.087	.747	.294
4.572	1.800	.178	.070	.635	.250
4.826	1.900	.130	.051	.521	.205
5.080	2.000	.084	.033	.399	.157
5.334	2.100	.025	.010	.267	.105
5.552	2.186	.089	.035	.089	.035

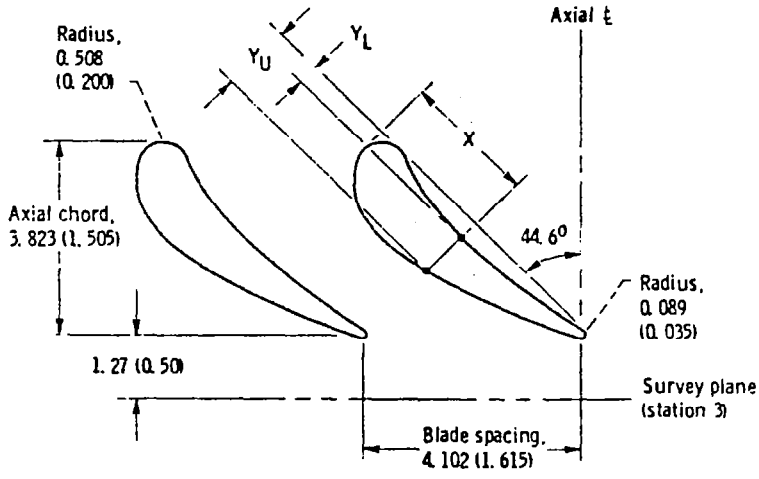

Figure 5 Mean section vane geometry and coordinates for the axial annular cascade.

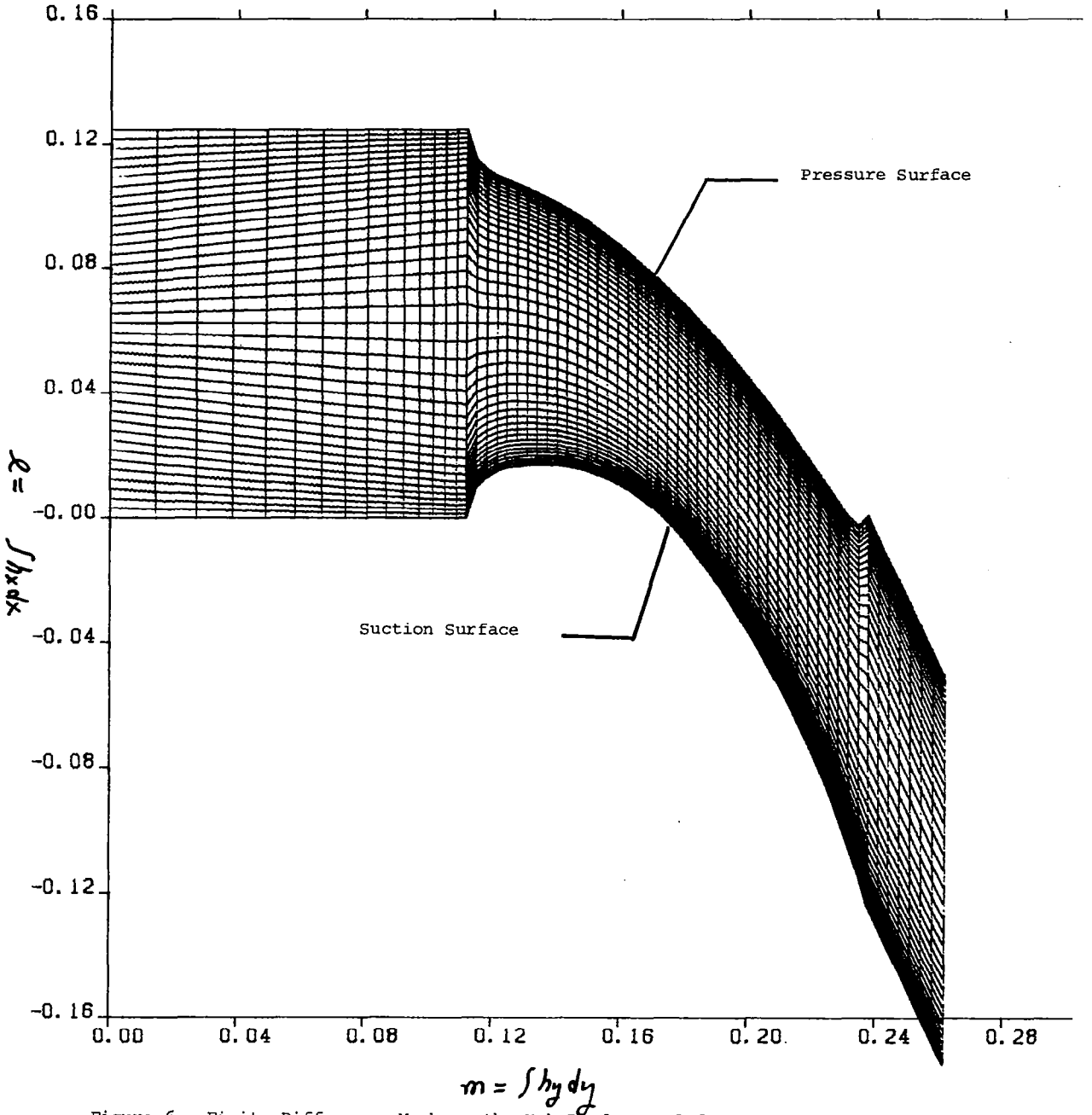

Figure 6 Finite Difference Mesh on the Hub Blade-to-Blade Surface: Mesh Comprised of 42 Streamline-like Lines and 63 Potential-like Lines.

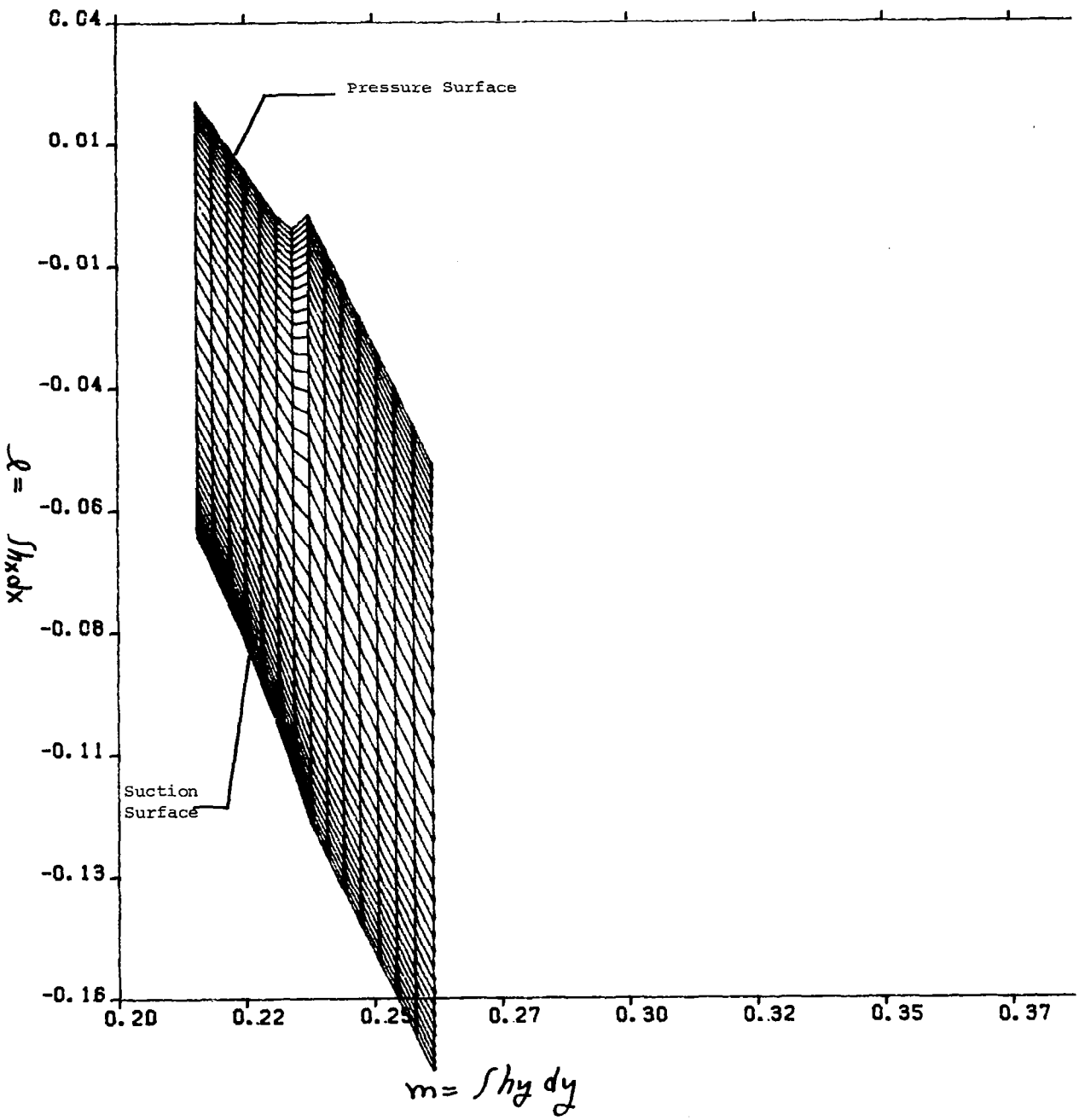

Figure 7 Blow-up of Mesh in the Turbine Nozzle Discharge Region at Hub Radius

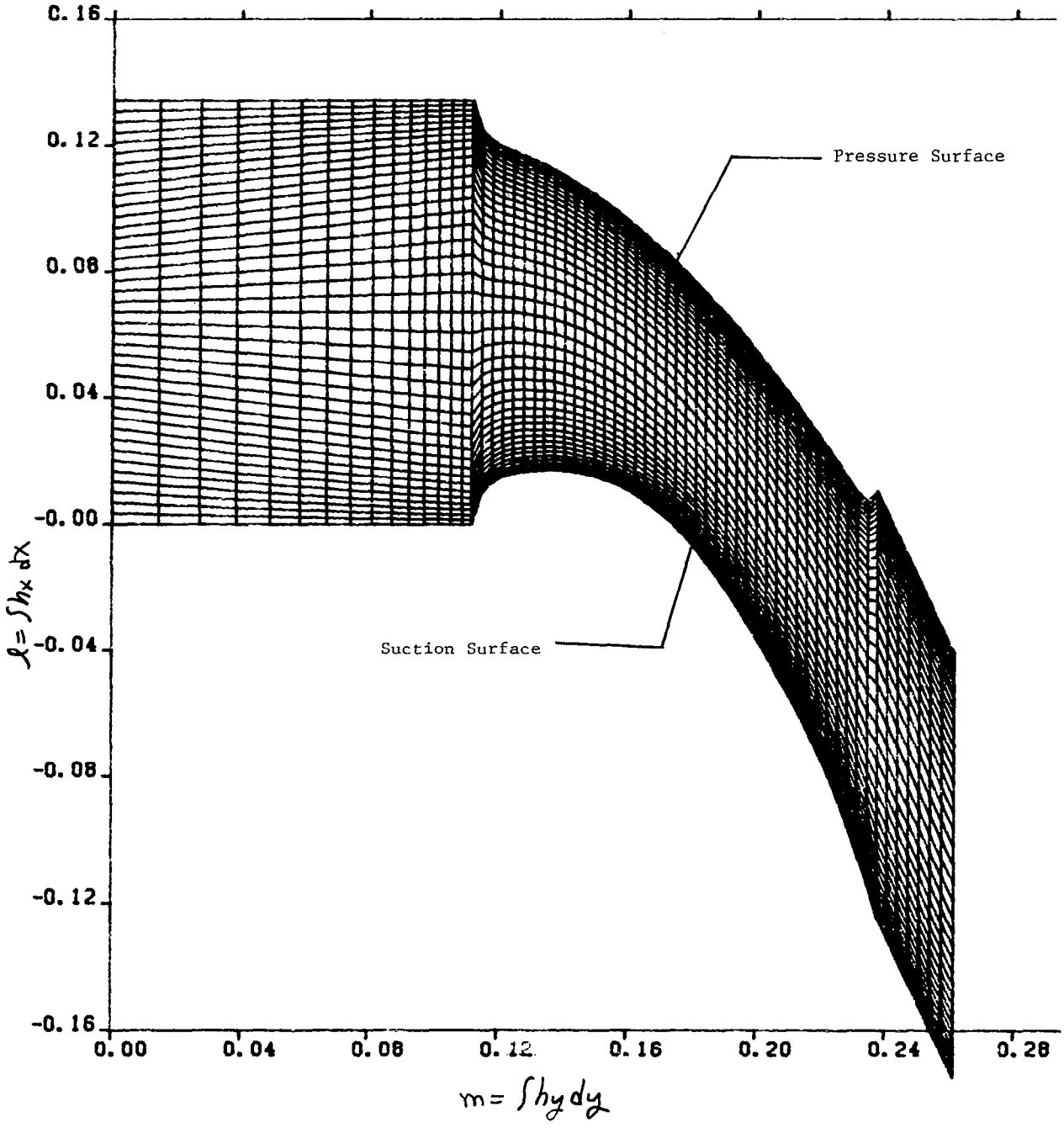

Figure 8 Finite Difference Mesh on the Mean Blade-to-Blade Surface; Mesh Comprised of 42 Streamline-like Lines and 63 Potential-like Lines.

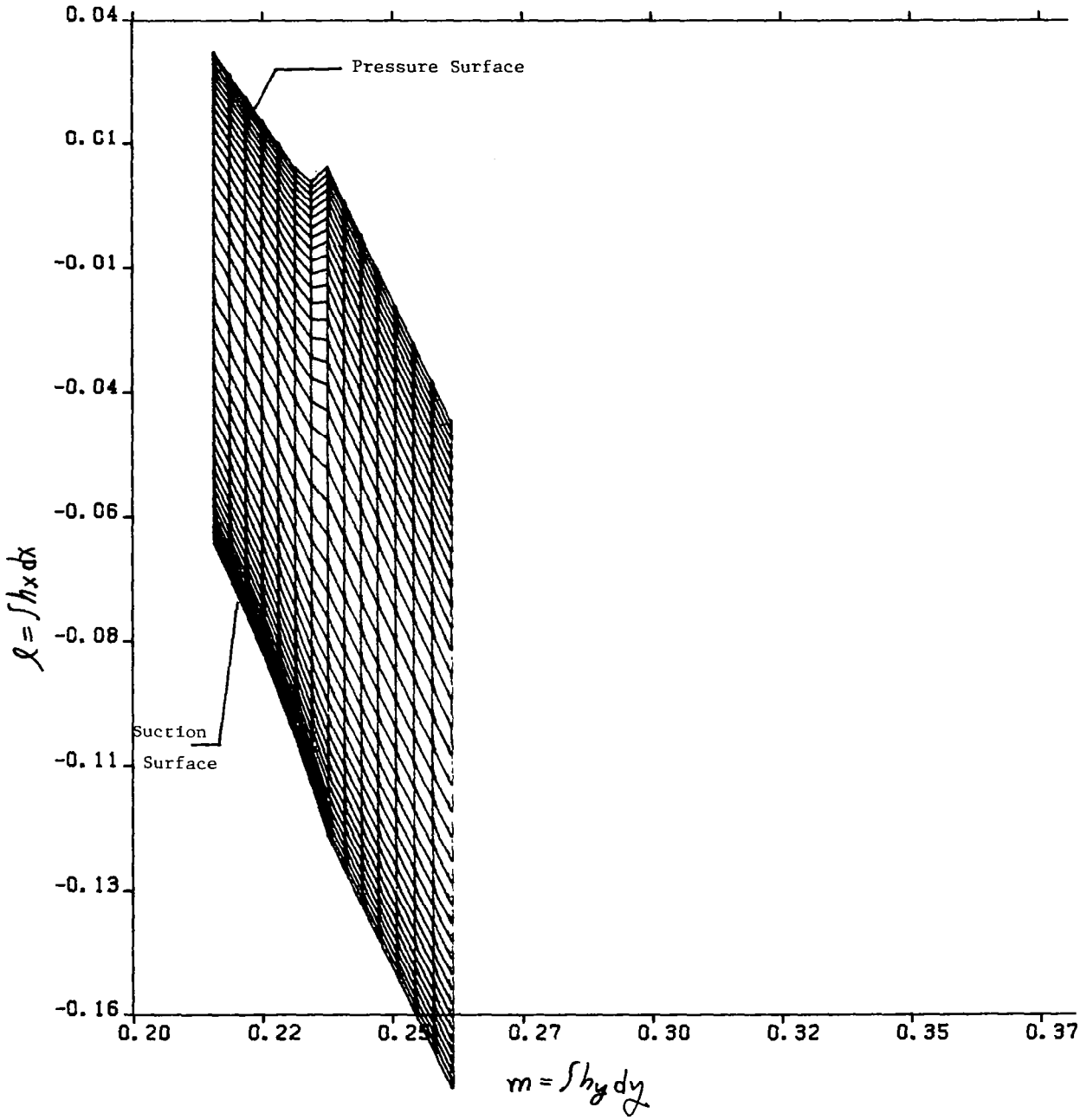

Figure 9 Blow-up of Mesh in the Turbine Nozzle Discharge Region at the Mean Radius.

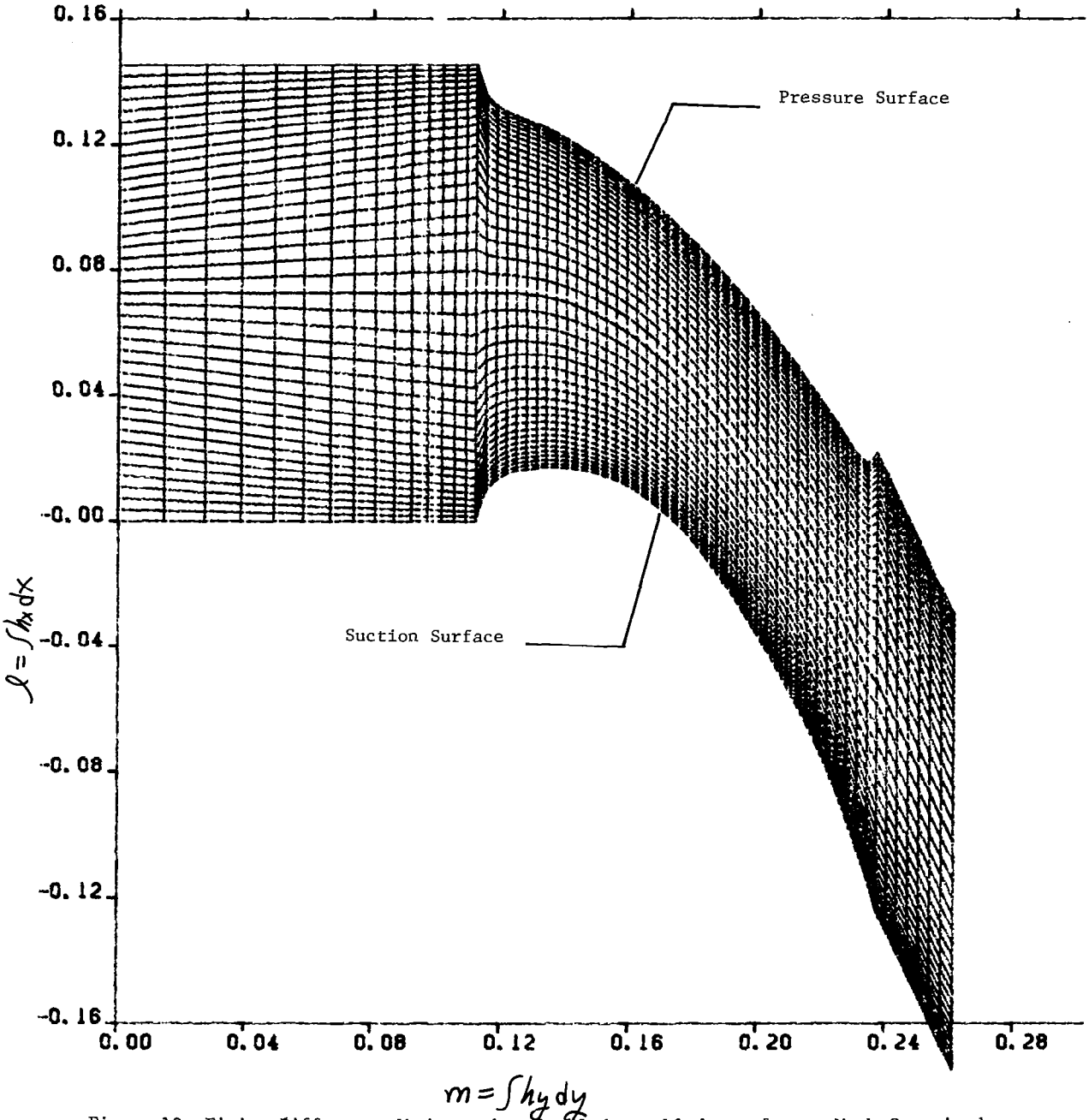

Figure 10 Finite Difference Mesh on the Tip Blade-to-blade Surface: Mesh Comprised of 42 Streamline-like Lines and 63 Potential-like Lines.

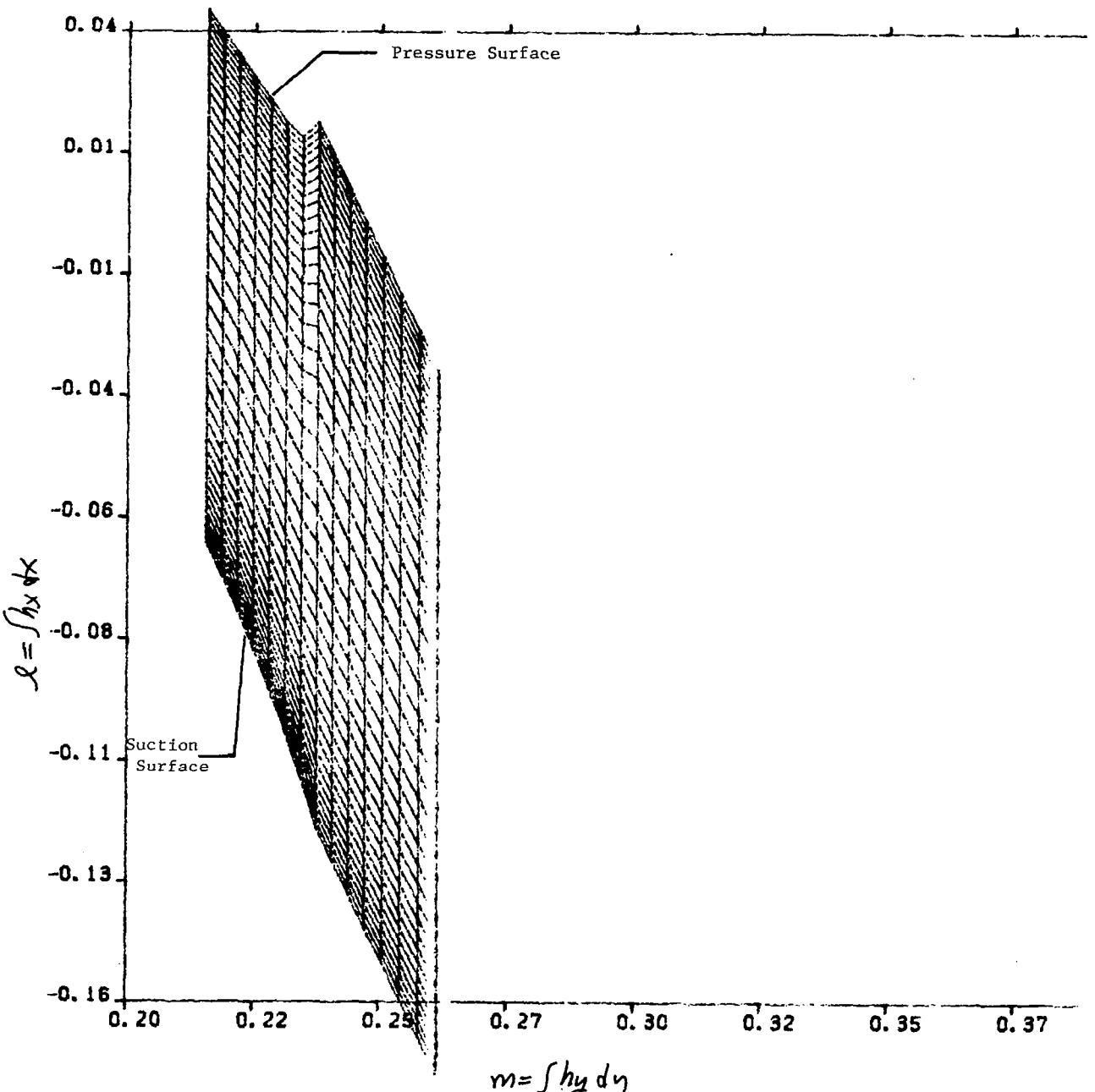

Figure 11 Blow-up of mesh in the Turbine Nozzle Discharge Region at the Tip Radius.

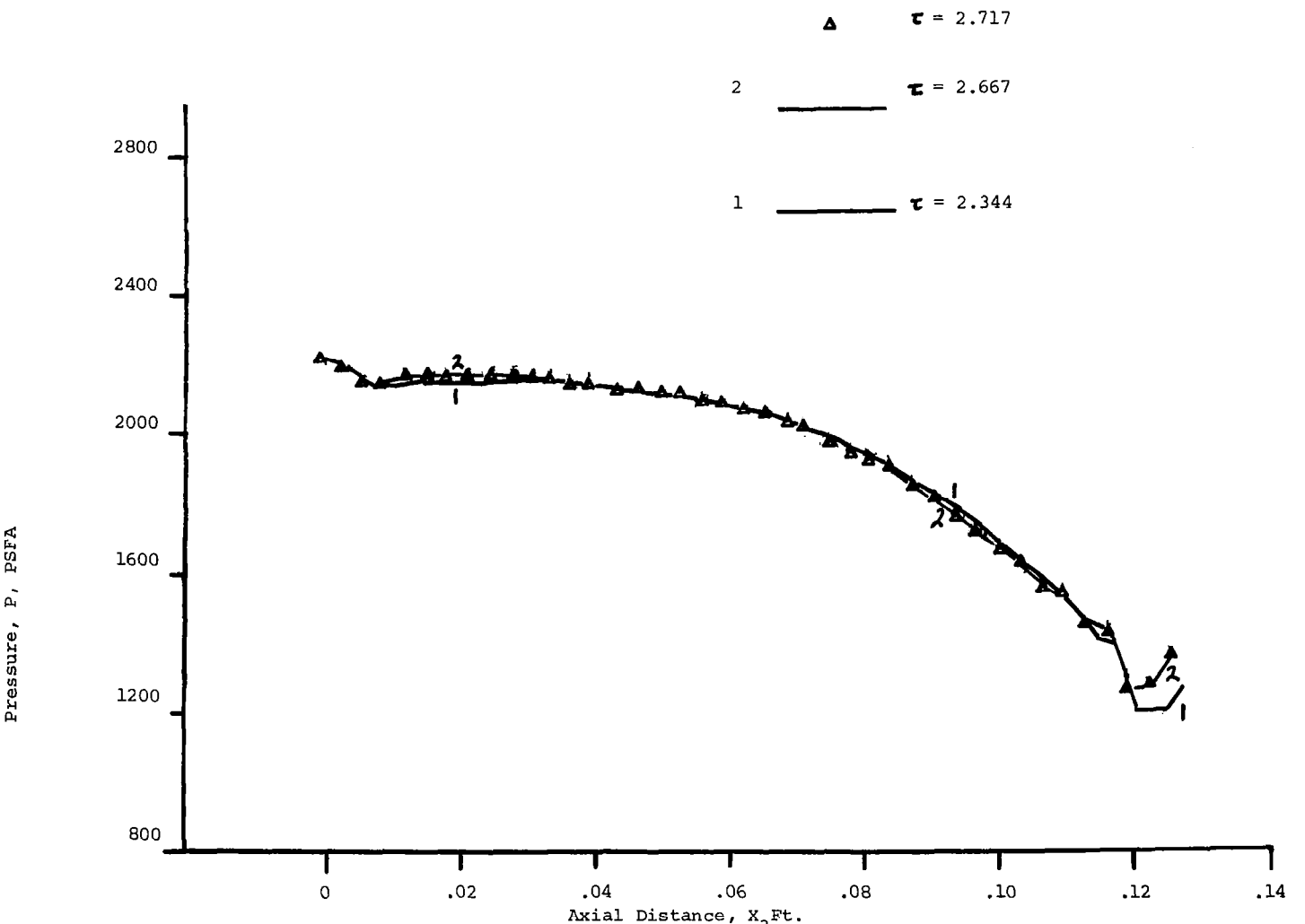

Figure 12 Pressure Surface Pressure Distributions at Three Characteristic Times in the Cascade Calculation; a Characteristic Time τ of Unity is the Time it Takes a Particle to Travel an Axial Chord.

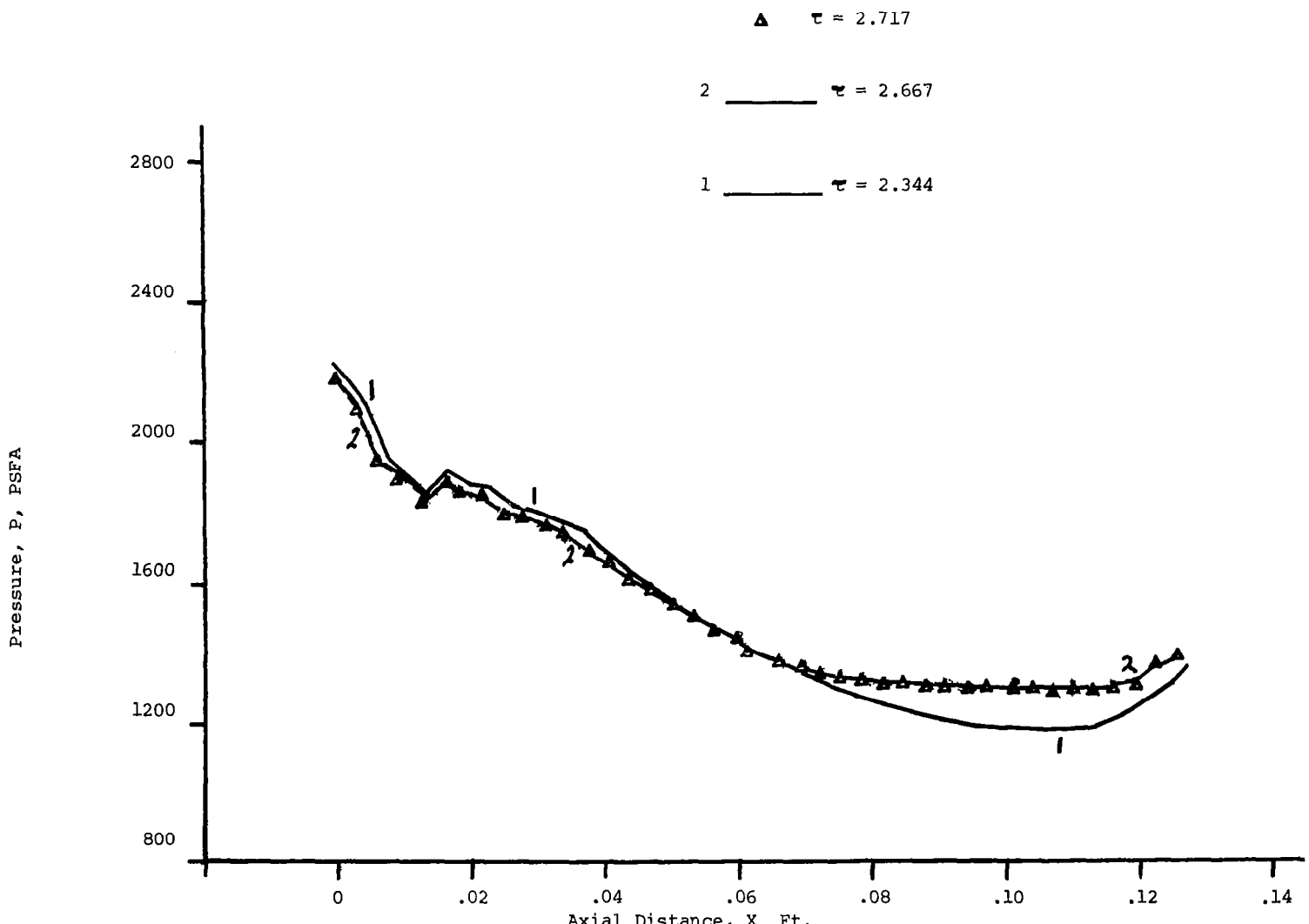

Figure 13 Suction Surface Pressure Distributions at Three Characteristic Times in the Cascade Calculation; a Characteristic Time τ of Unity is the Time it Takes a Particle to Travel an Axial Chord.

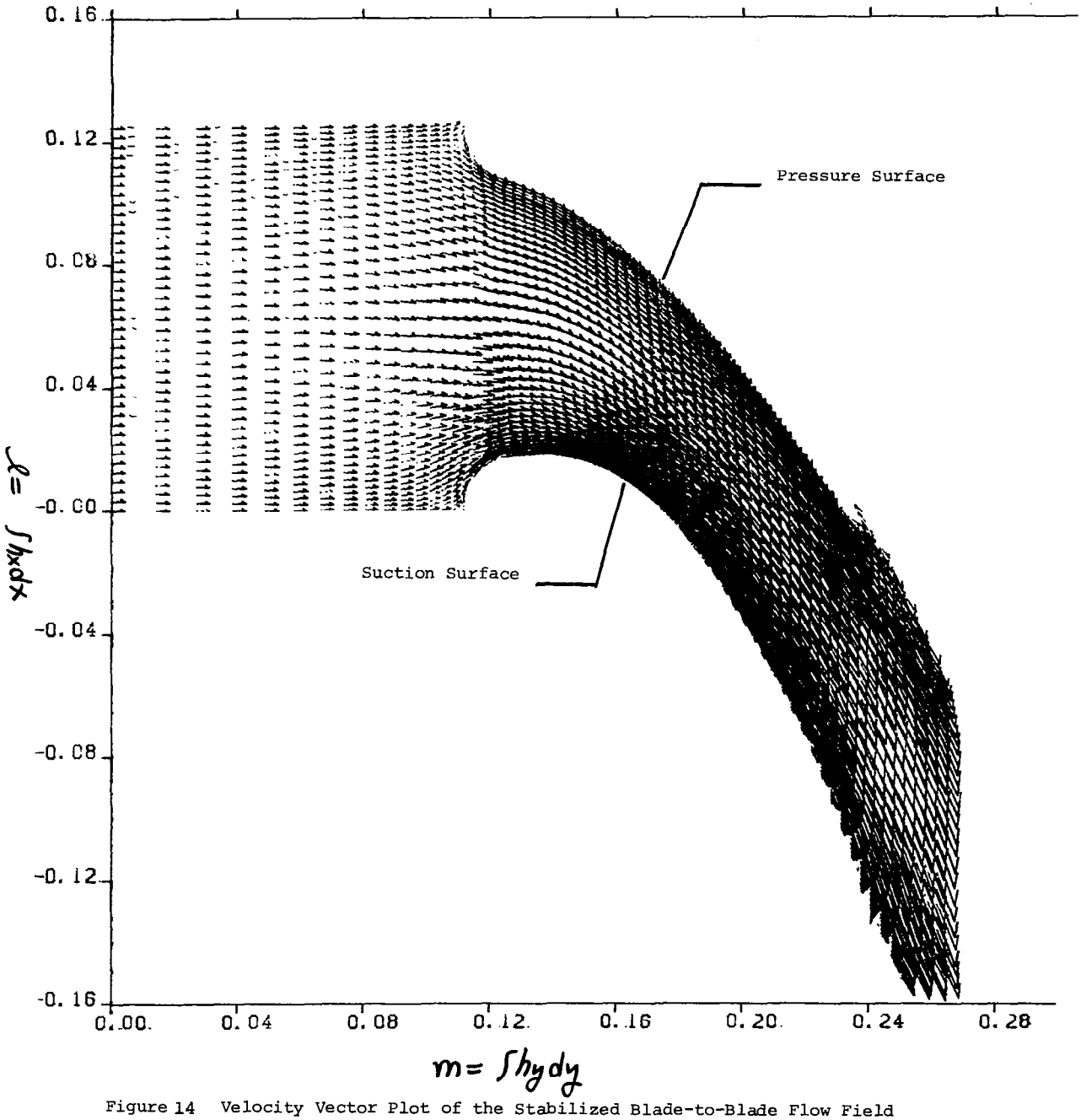

Figure 14 Velocity Vector Plot of the Stabilized Blade-to-Blade Flow Field at the Hub.

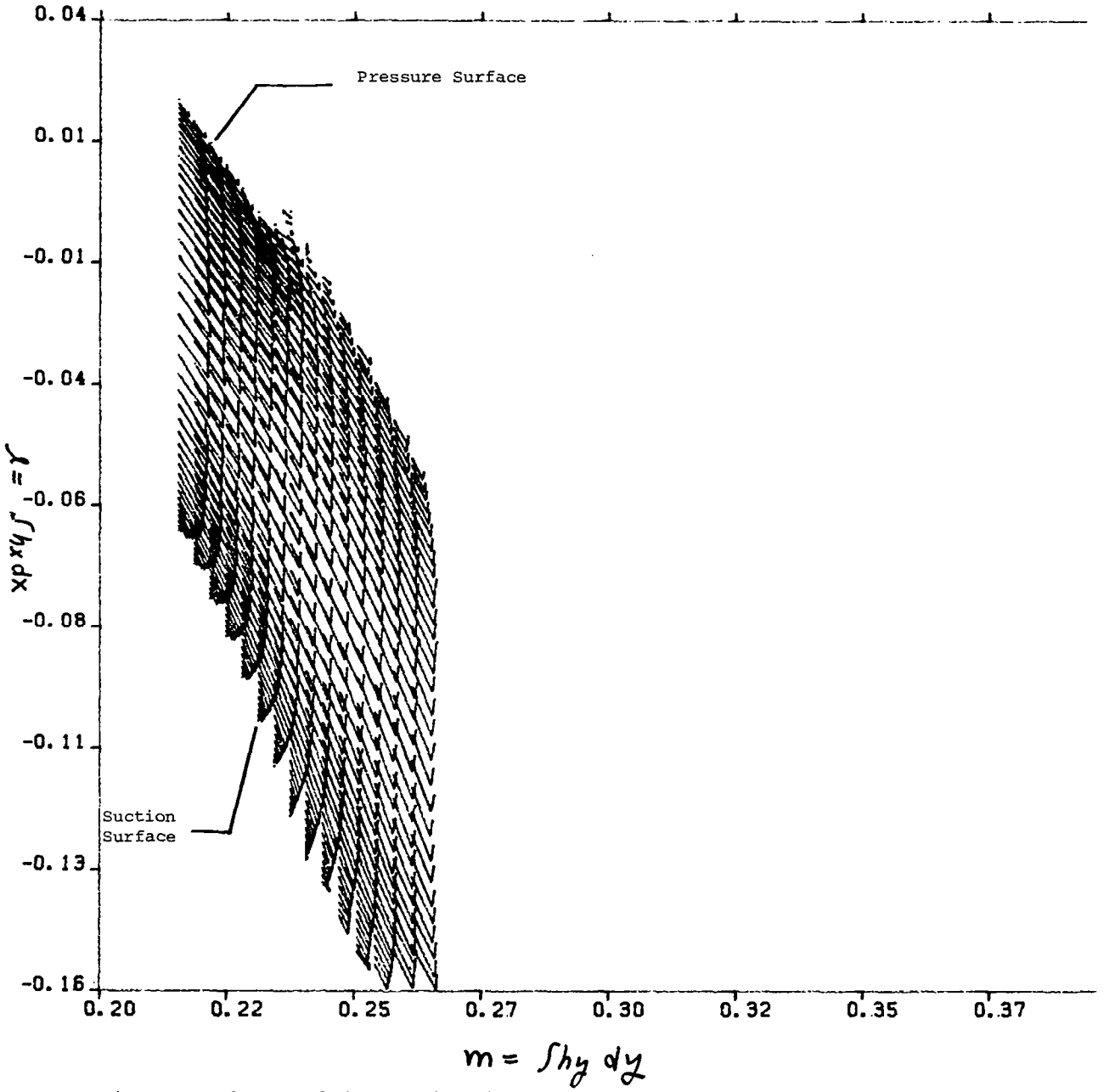

Figure 15 Blow-up of the Velocity Field in the Turbine Cascade Discharge Region at the Hub.

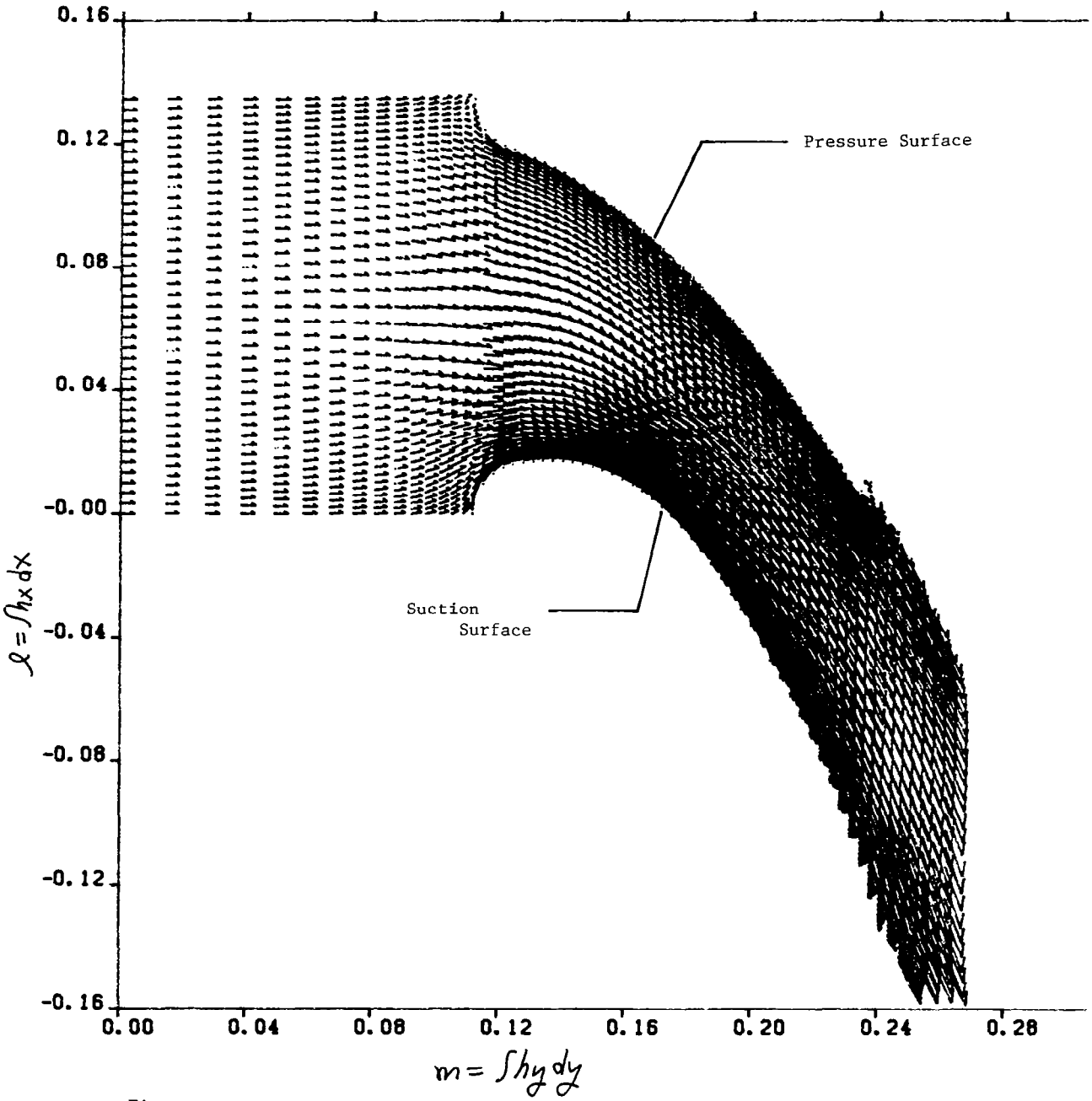

Figure 16 Velocity Vector Plot of the Blade-to-Blade Flow Field at the Mean Radius.

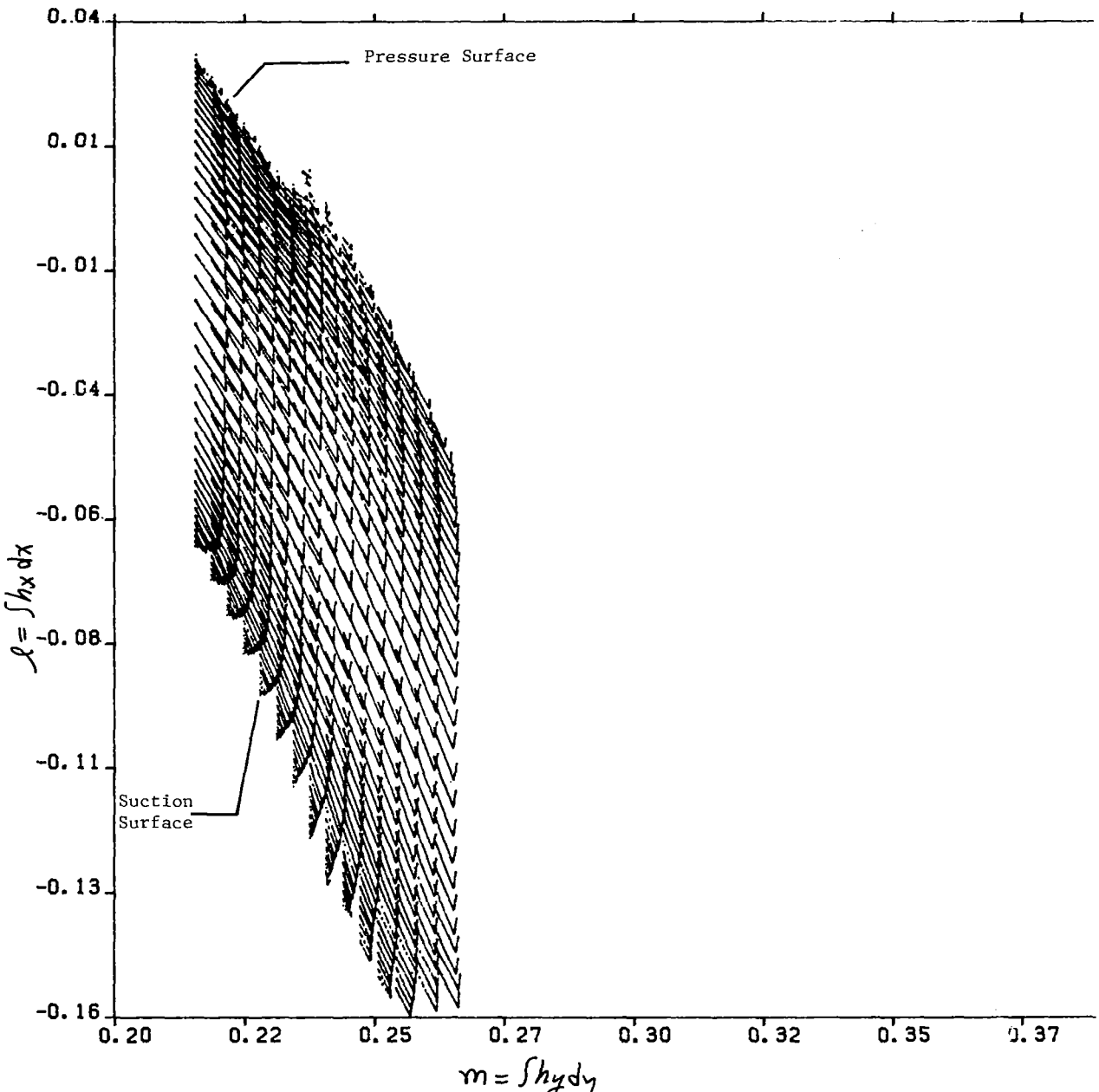

Figure 17 Blow-up of the Velocity Field in the Turbine Cascade Discharge Region at the Mean Radius.

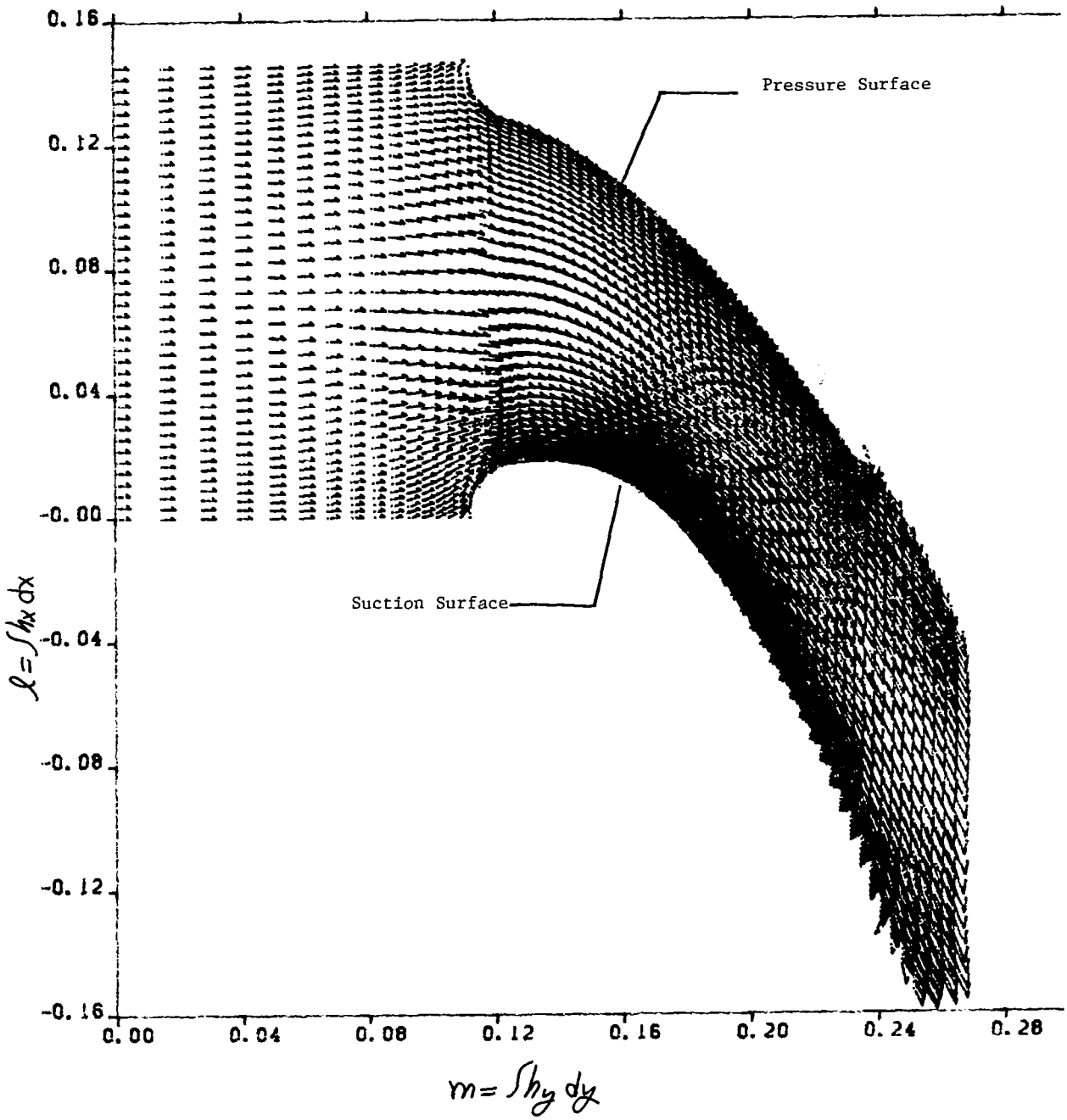

Figure 18 Velocity Vector Plot of the Stabilized Blade-to-Blade Flow Field at the Tip Radius.

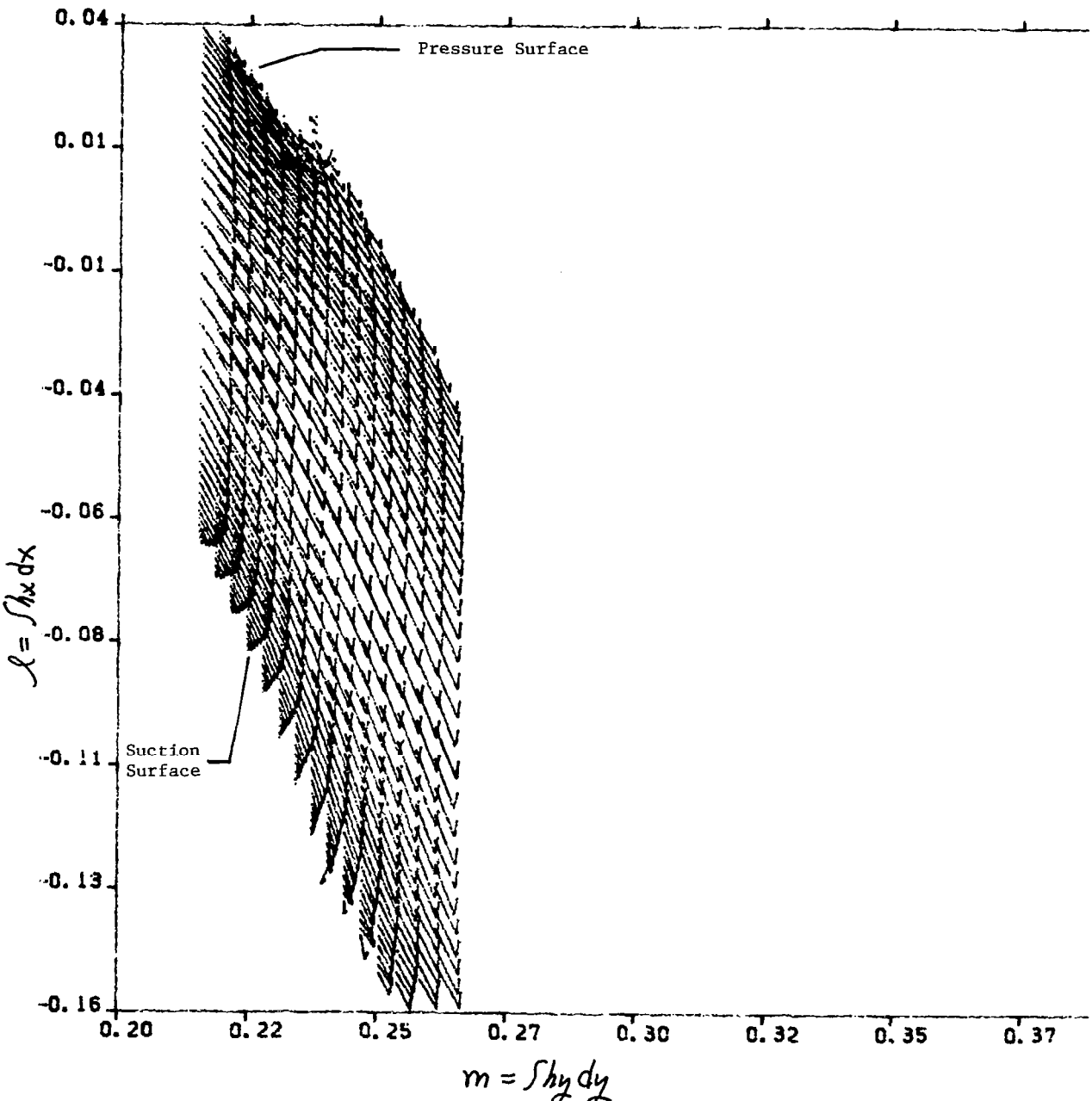

Figure 19 Blow-up of the Velocity Field in the Turbine Cascade Discharge Region at the Tip Radius.

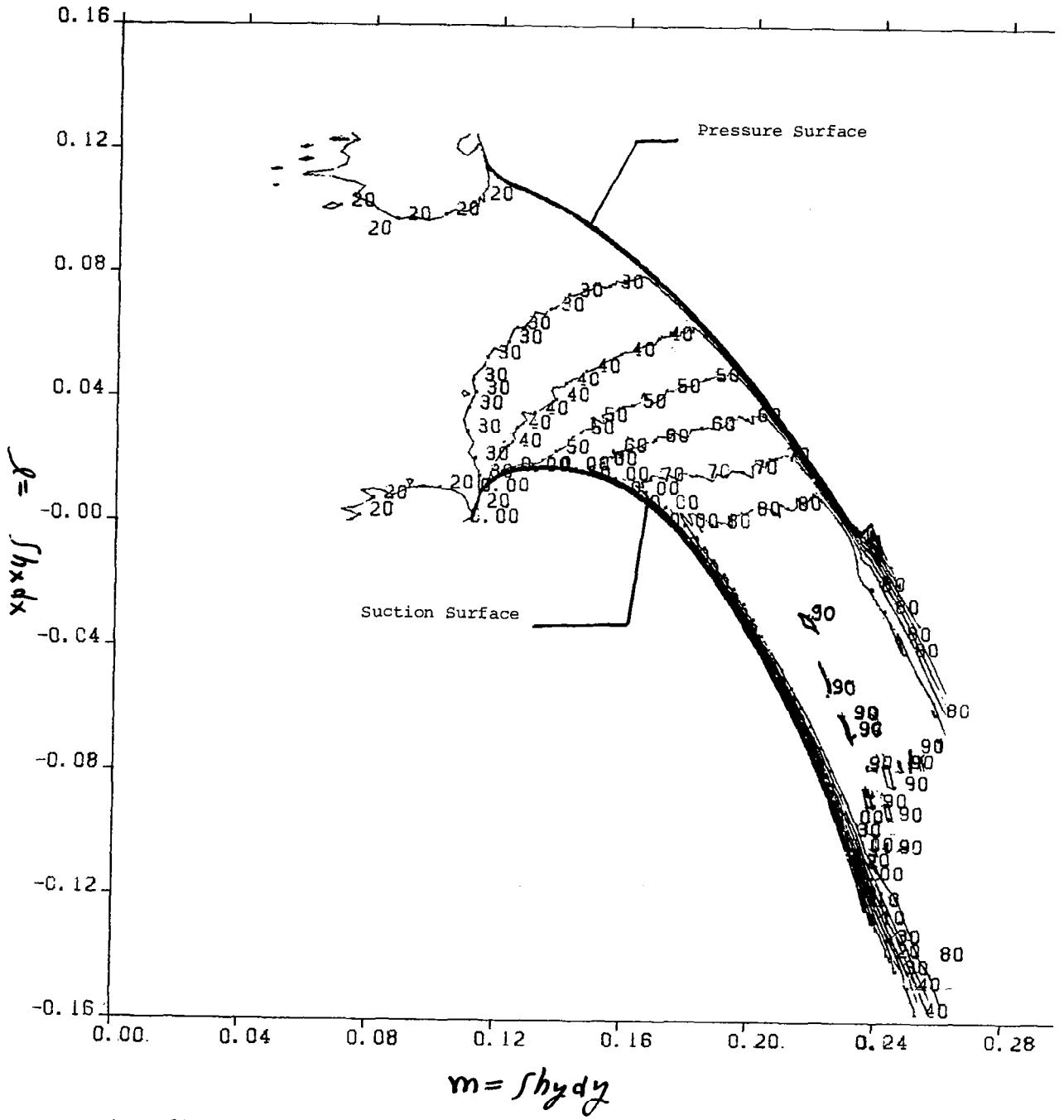

Figure 20 Contour Plot of the Ratio of the Velocity to the Critical Velocity on the Hub Blade-to-Blade Surface.

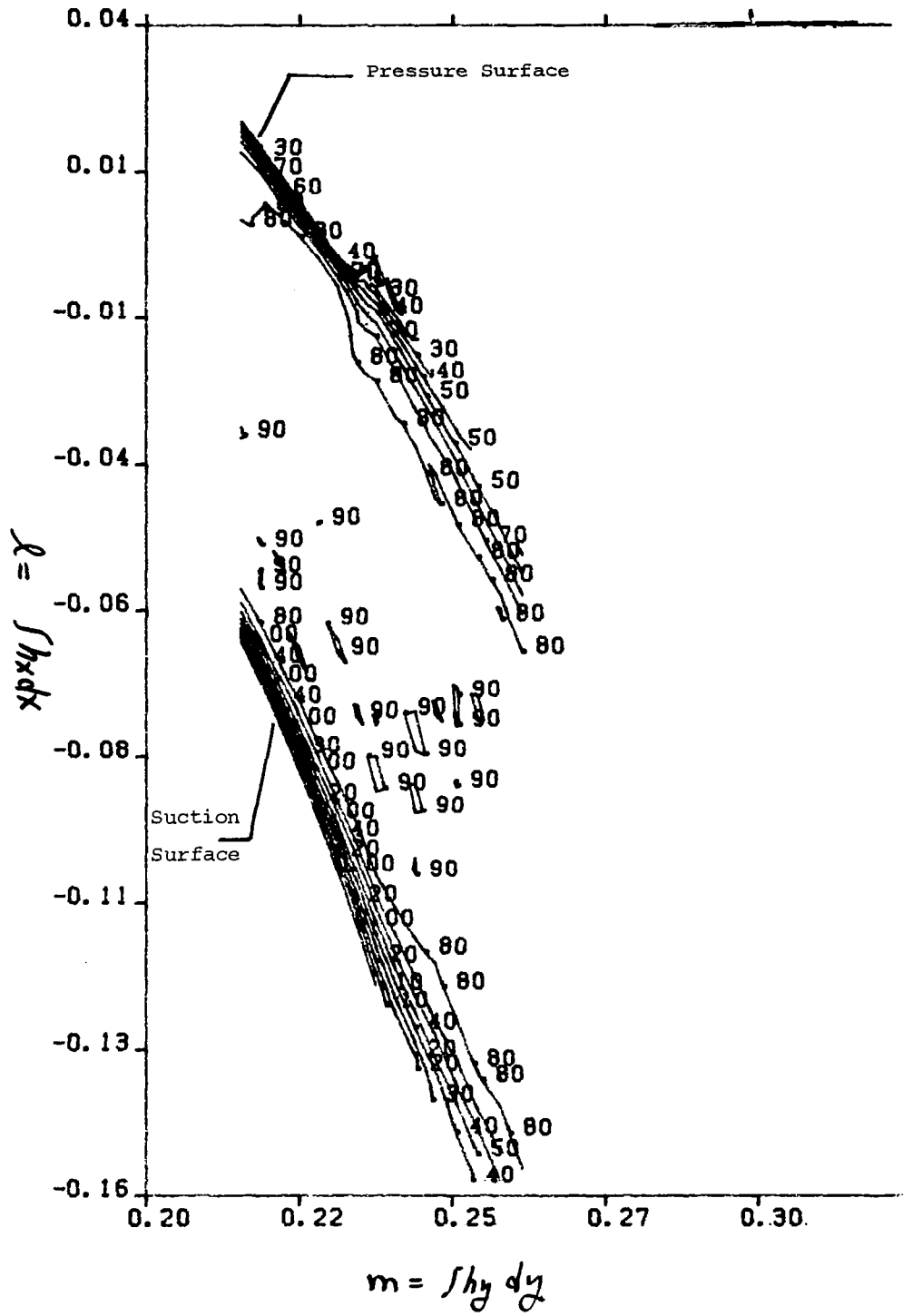

Figure 21 Blow-up of the Ratio of the Velocity to the Critical Velocity at the Turbine Cascade Discharge Region at the Hub.

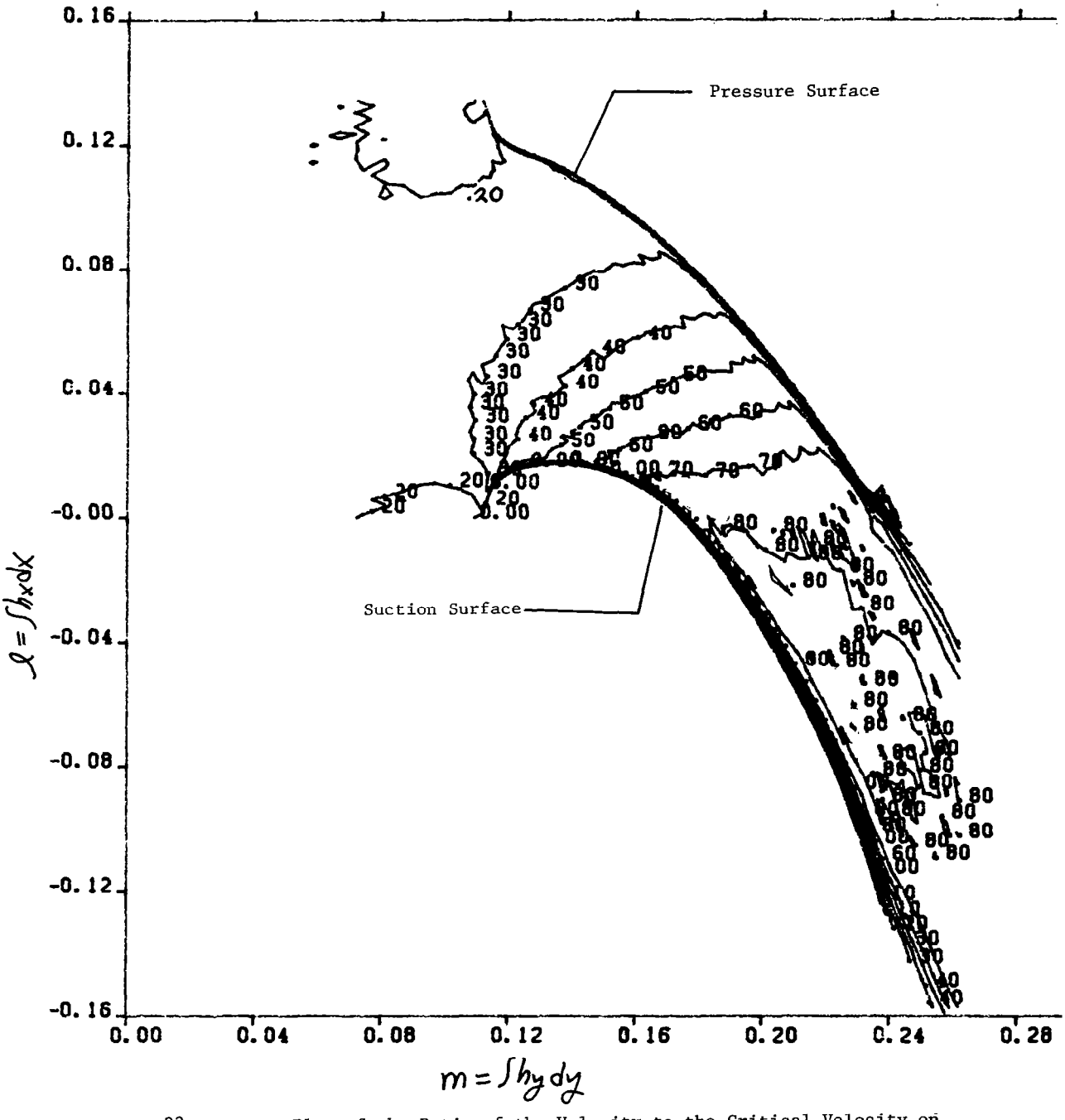

Figure 22 Contour Plot of the Ratio of the Velocity to the Critical Velocity on the Mean Blade-to-Blade Surface.

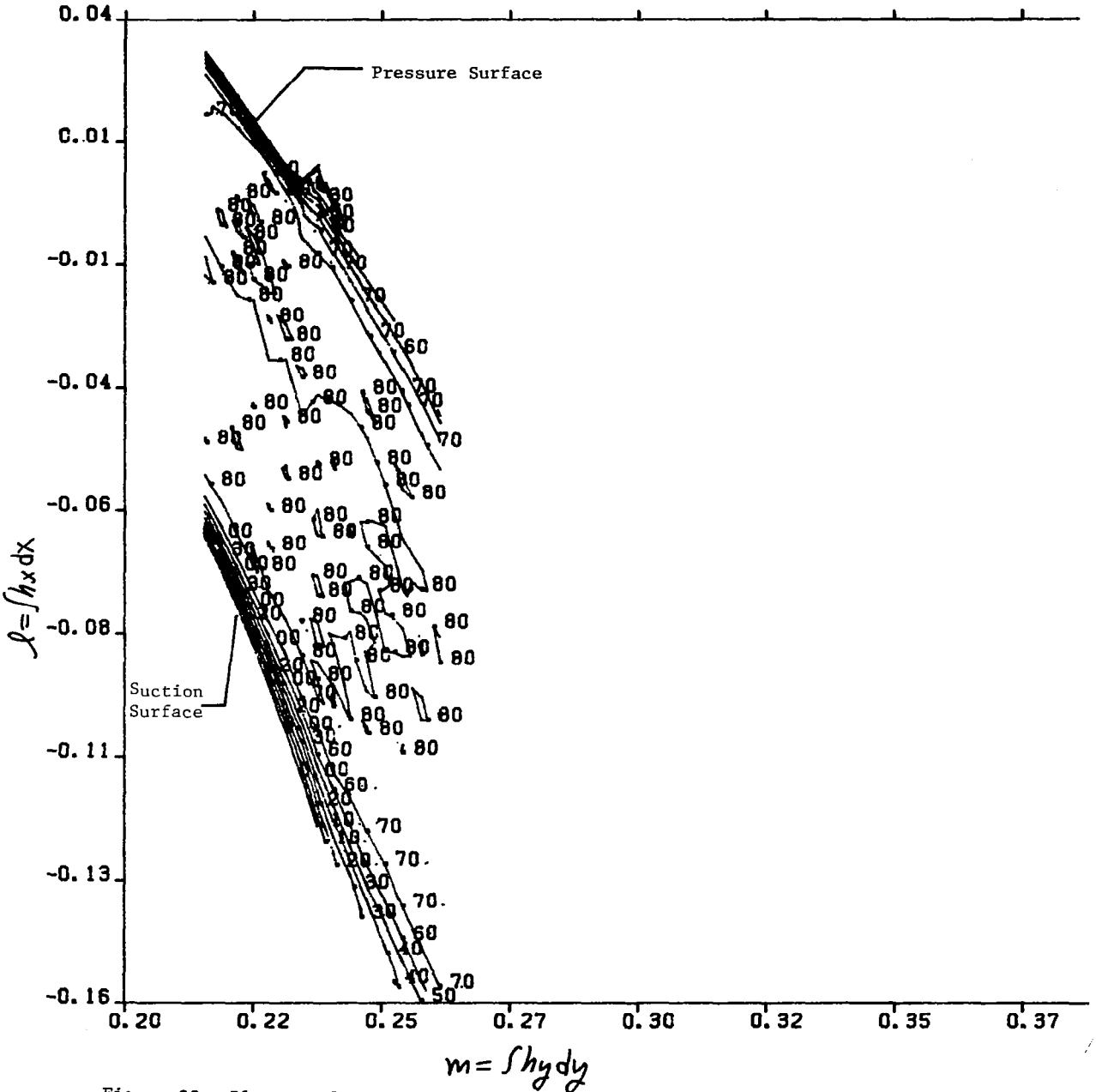

Figure 23 Blow-up of the Ratio of the Velocity to the Critical Velocity at the Turbine Cascade Discharge Region at the Mean Radius.

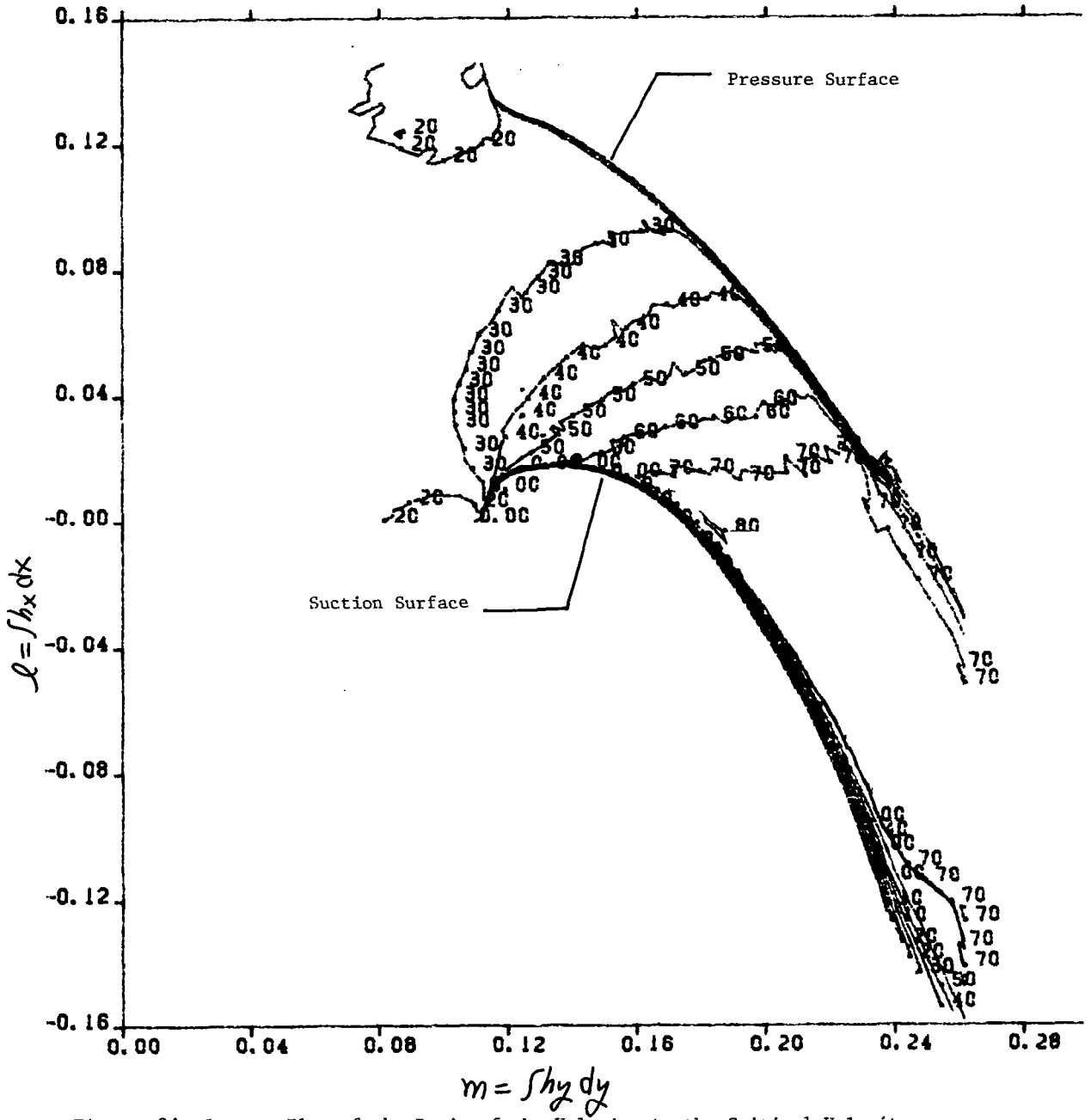

Figure 24 Contour Plot of the Ratio of the Velocity to the Critical Velocity on the Tip Blade-to-Blade Surface.

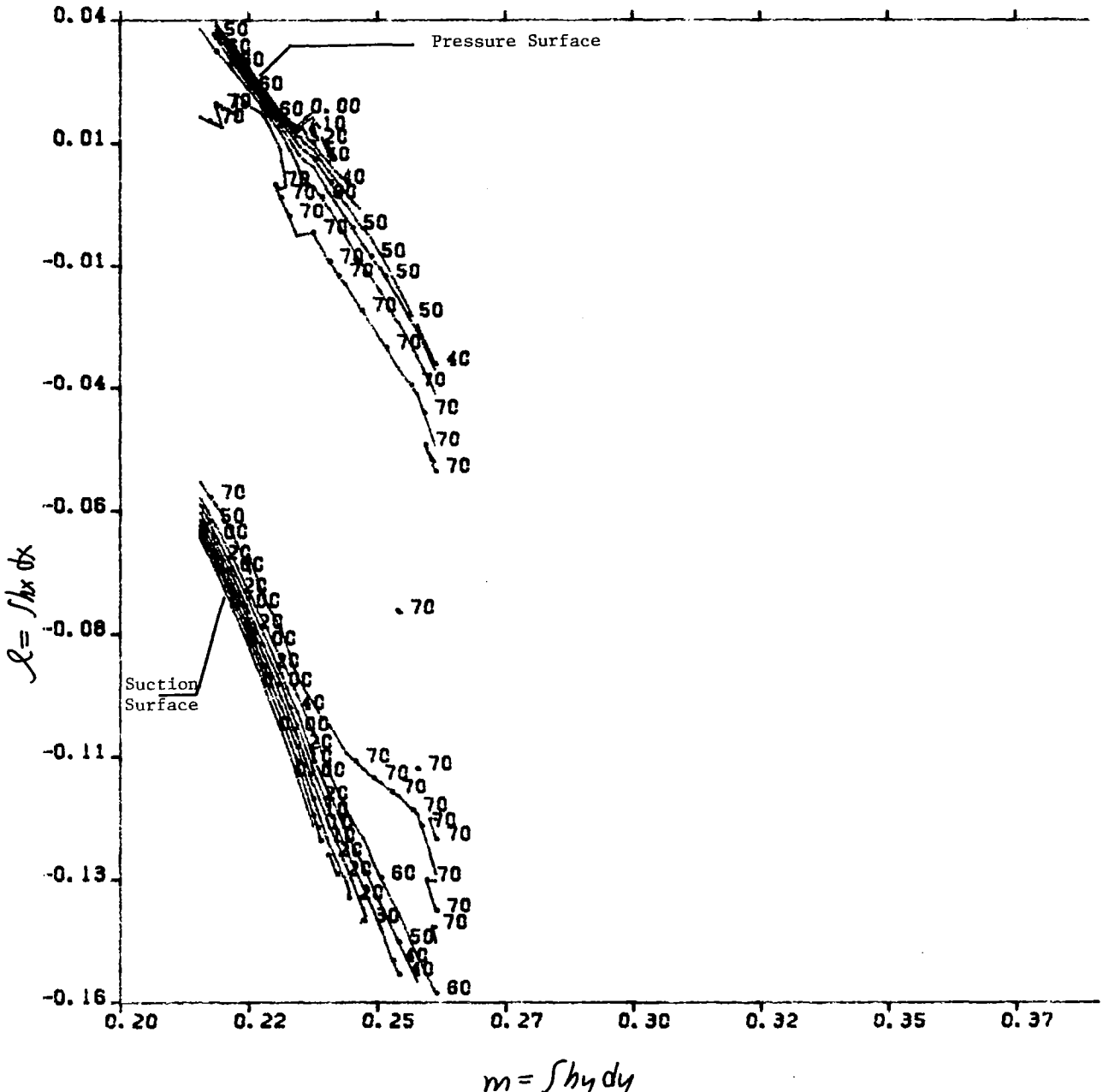

Figure 25 Blow-up of the Ratio of the Velocity to the Critical Velocity at the Turbine Cascade Discharge Region at the Tip Radius.

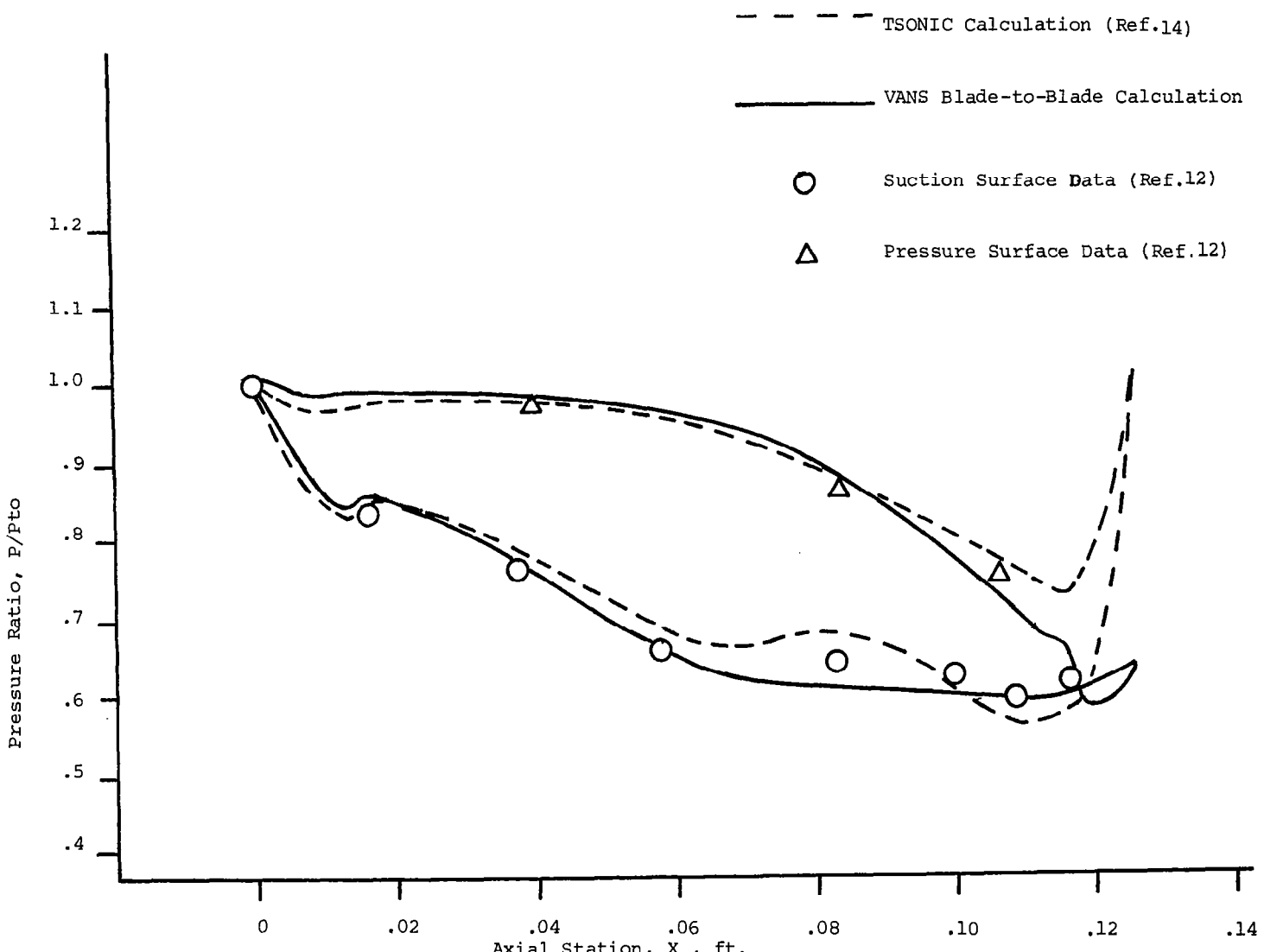

Figure 26 Comparison of blade pressure variations at the hub radius; Pto is the upstream stagnation pressure; hub radius R_{hub} = .7083 ft.

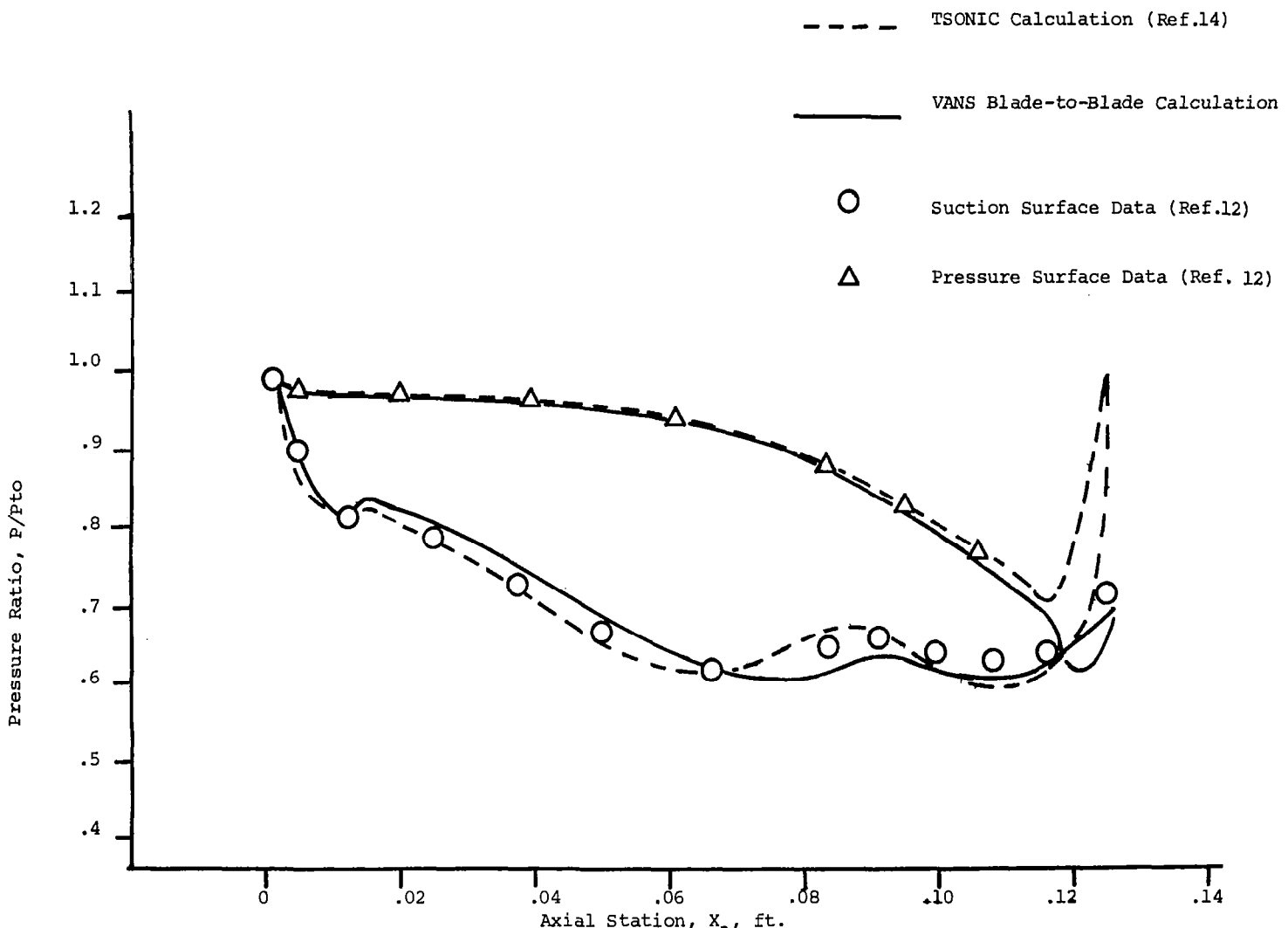

Figure 27 Comparison of blade pressure variations at the mean radius; Pto is the upstream stagnation pressure; mean radius R_{mean} = .7699 ft.

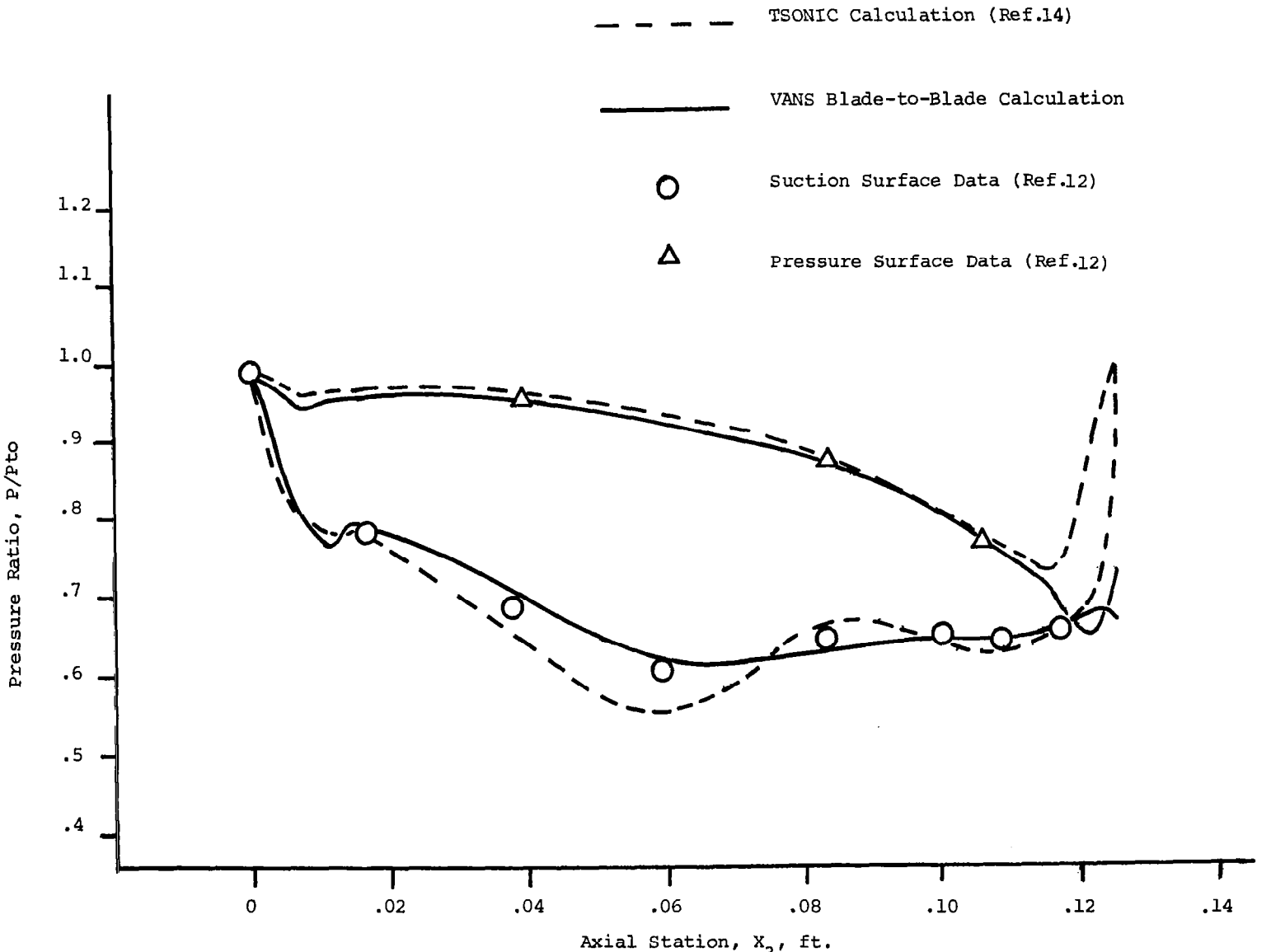

Figure 28 Comparison of blade pressure variations at the tip radius; Pto is the upstream stagnation pressure; tip radius R_{tip} = .8333 ft.

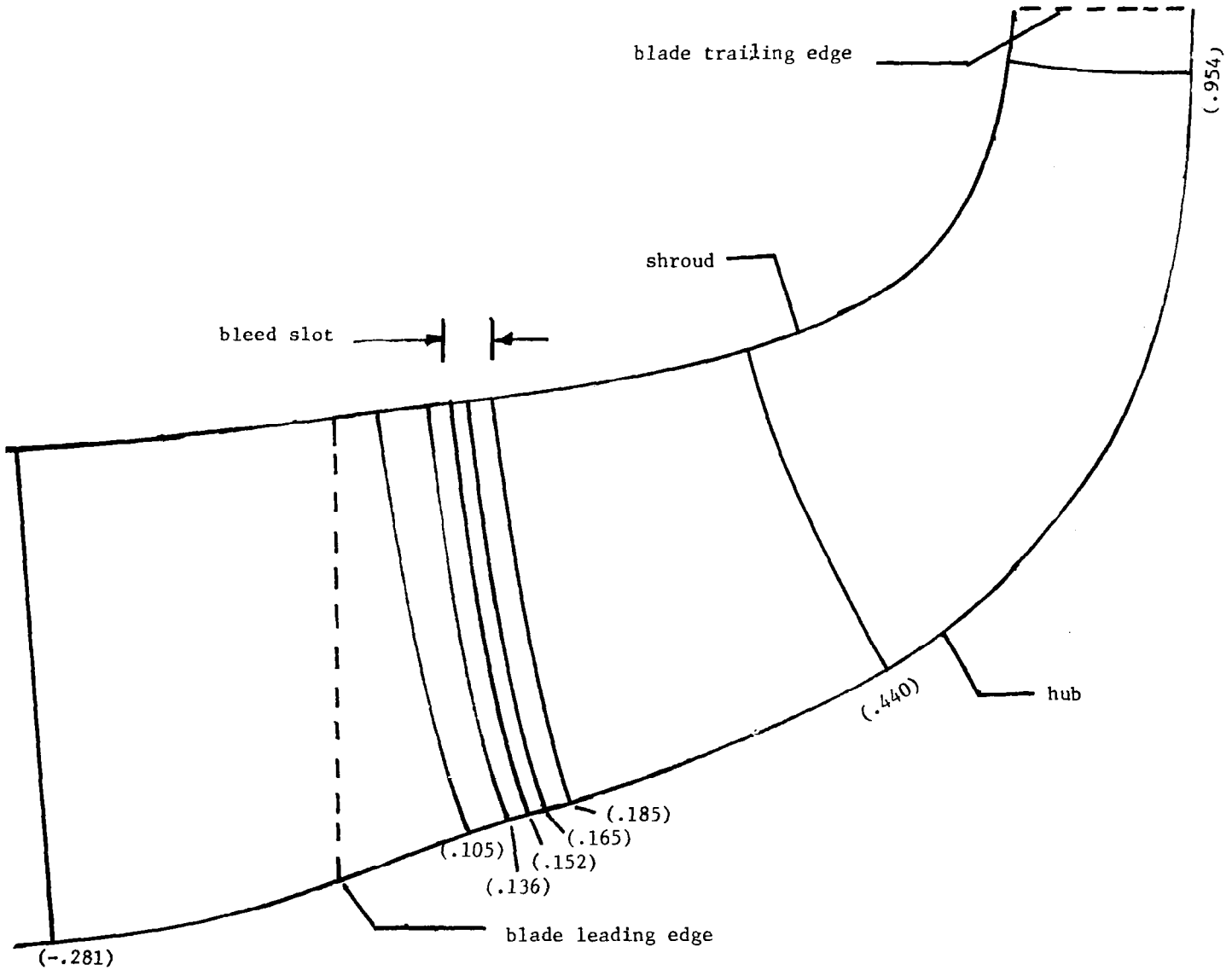

Figure 29. Schematic of impeller geometry showing cross-sectional surfaces which have been analysed; the parameter $\tilde{z}$ is defined in parenthesis.

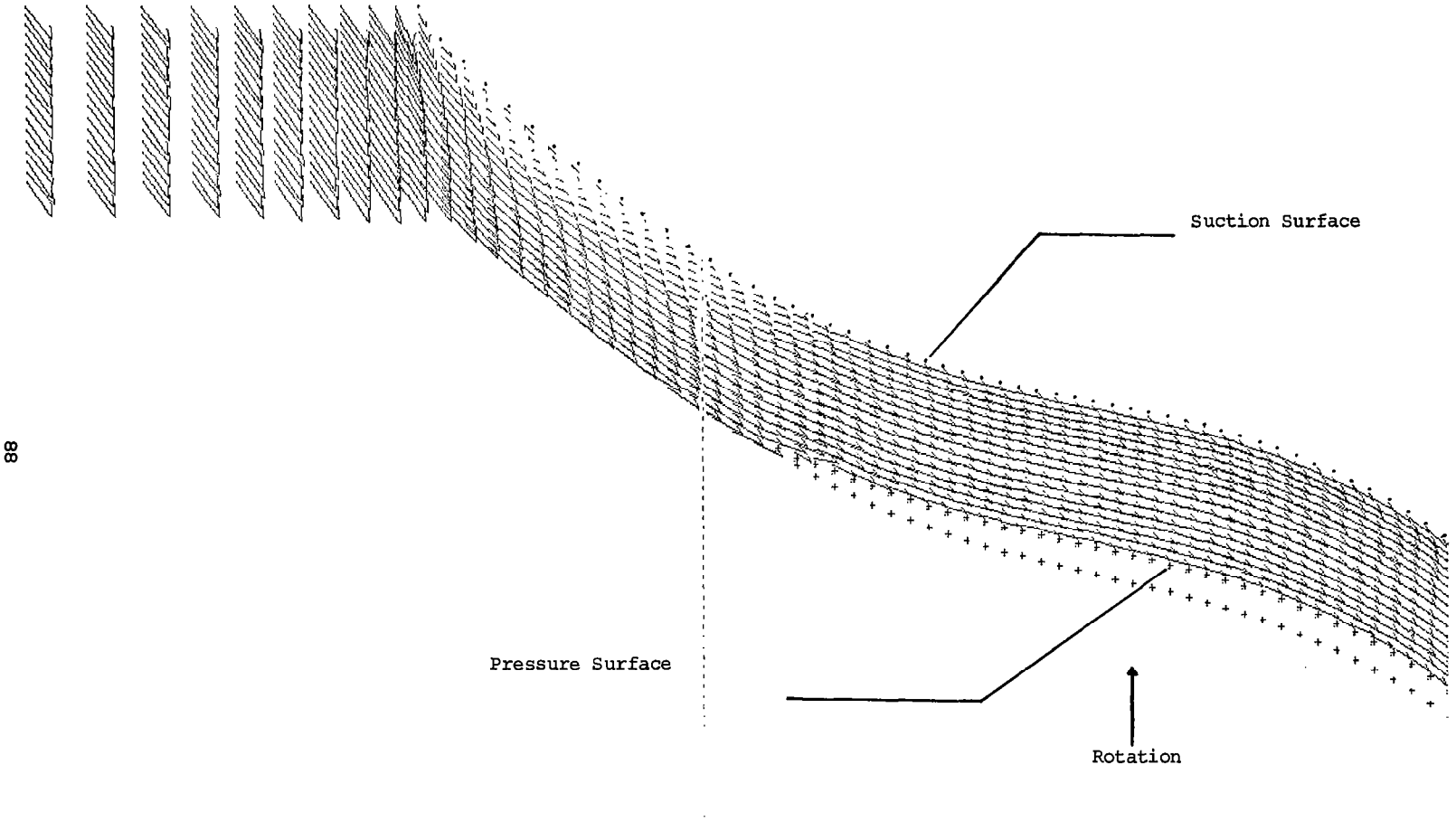

Figure 30. Velocity vector plot of the inducer flow field in the neighborhood of the suction surface; blade-to-blade surface trace in meridional plane located at 12 percent of the distance between the hub and the shroud.

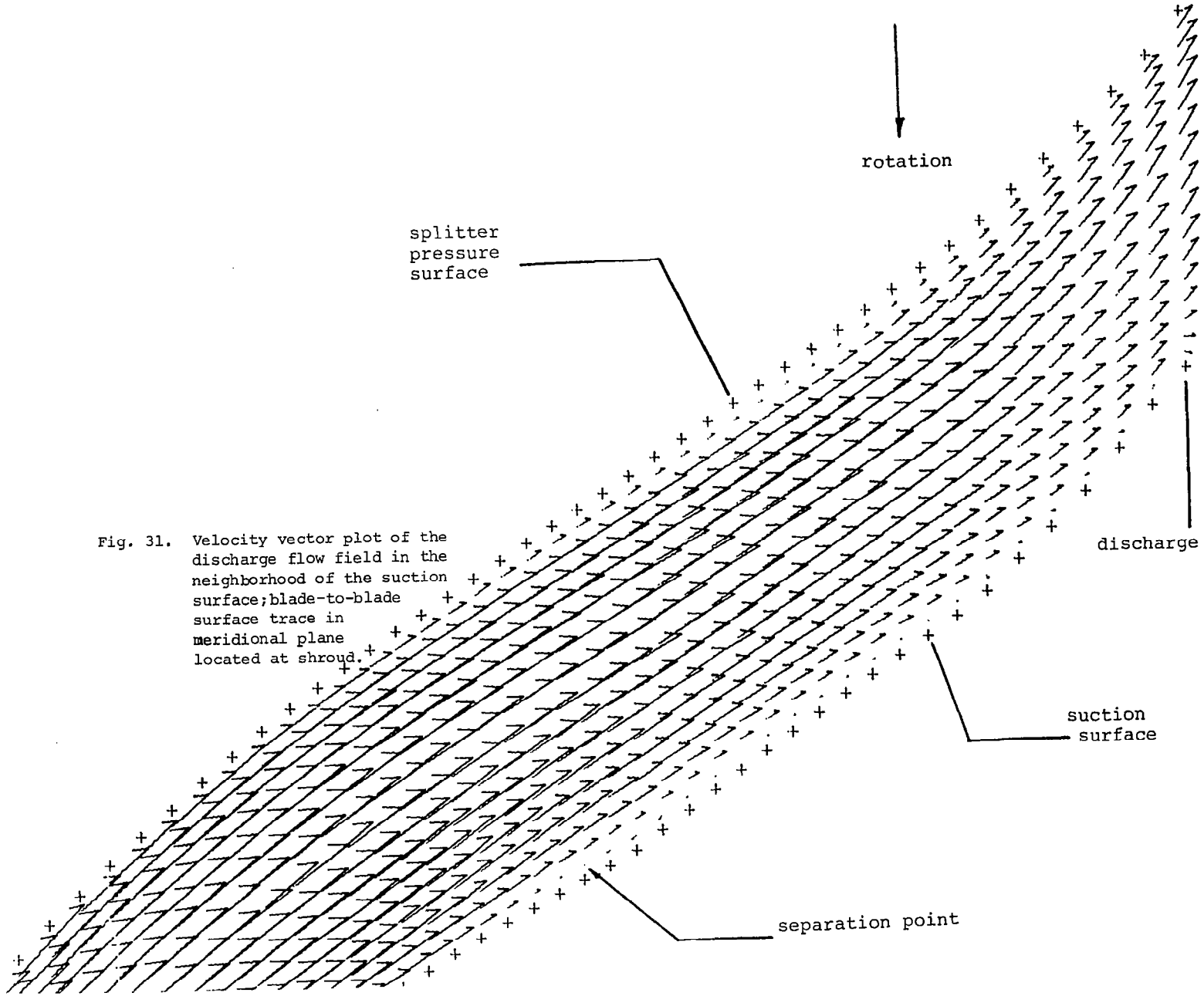

Fig. 31. Velocity vector plot of the discharge flow field in the neighborhood of the suction surface; blade-to-blade surface trace in meridional plane located at shroud.

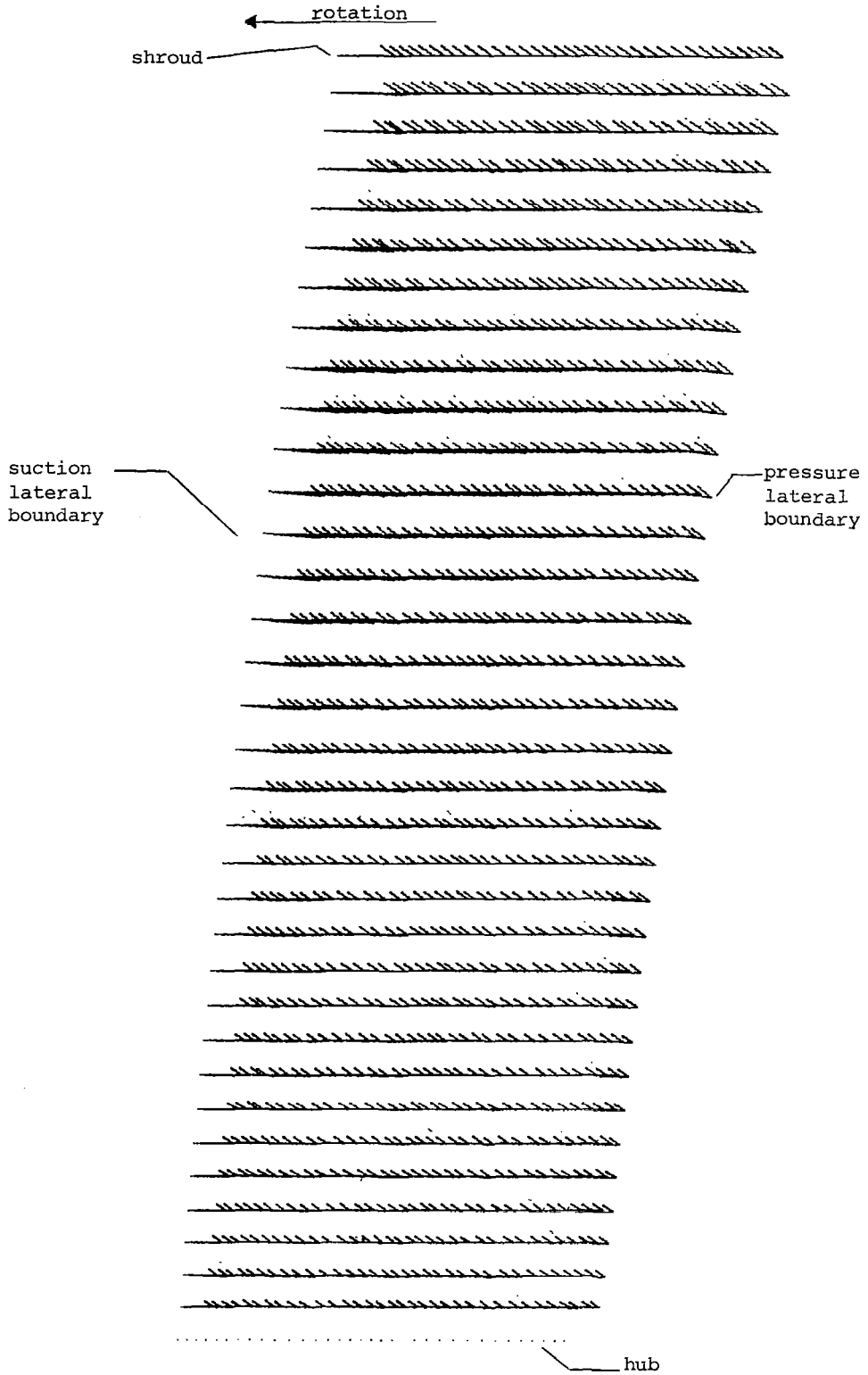

Figure 32. Velocity vector plot of the cross-sectional flow field at a station corresponding to $\hat{z}$ = -.2183.

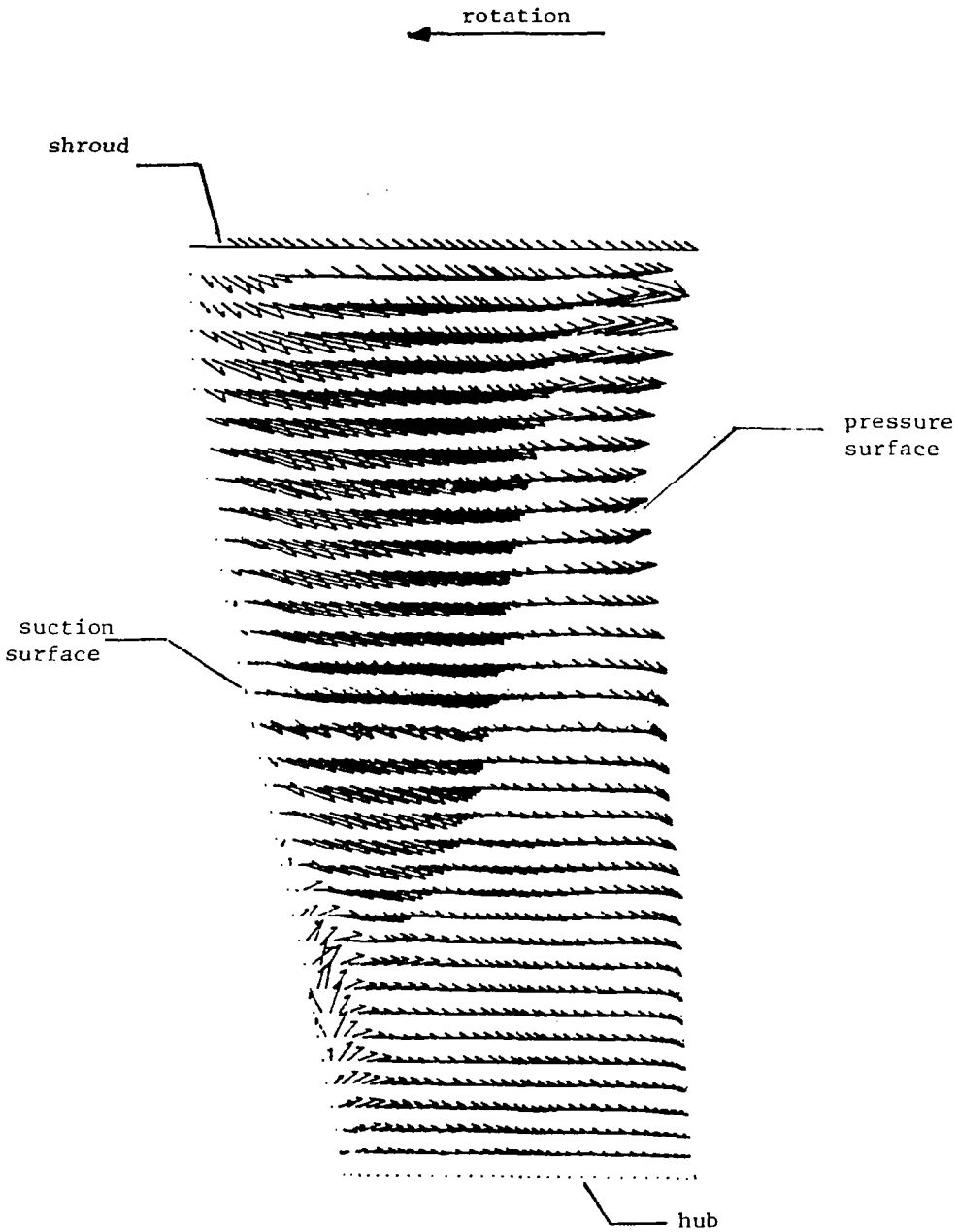

Figure 33. Velocity vector plot of the cross-sectional flow field at a station corresonding to $\tilde{z}$ = .1053.

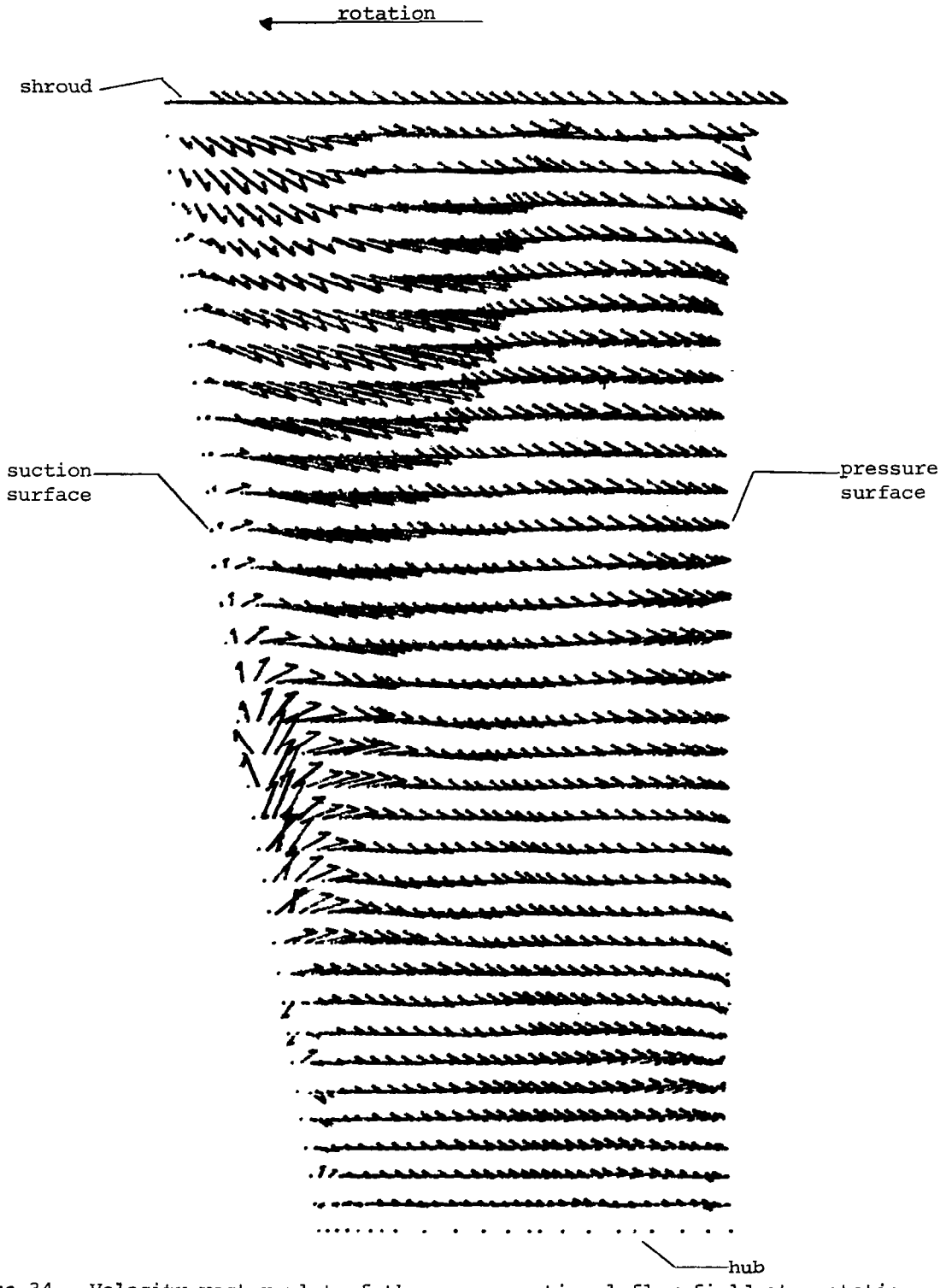

Figure 34. Velocity vector plot of the cross-sectional flow field at a station corresponding to $\hat{z}$ = .1362.

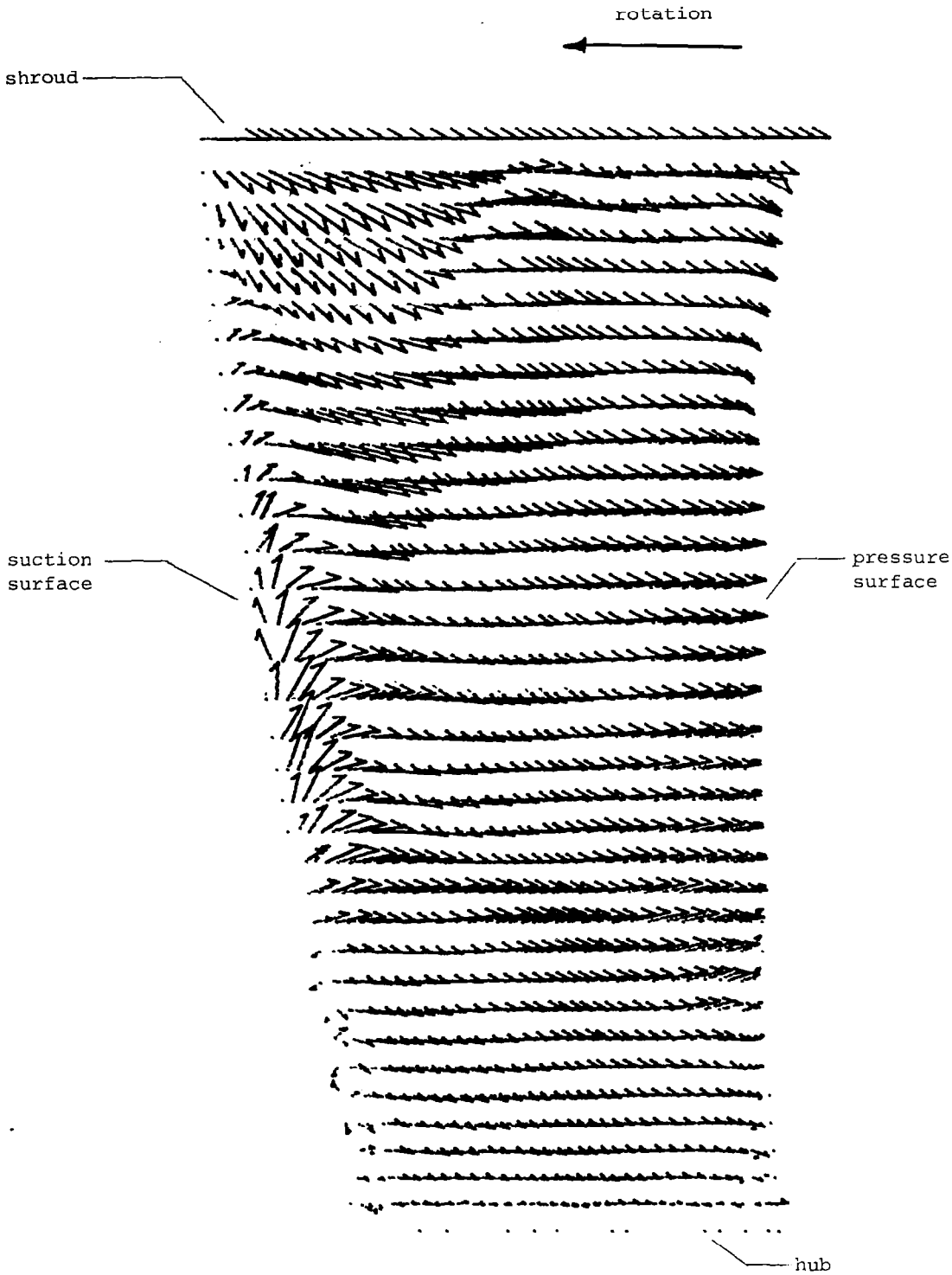

Figure 35. Velocity vector plot of the cross-sectional flow field at a station corresponding to $\hat{z}$ = .1522.

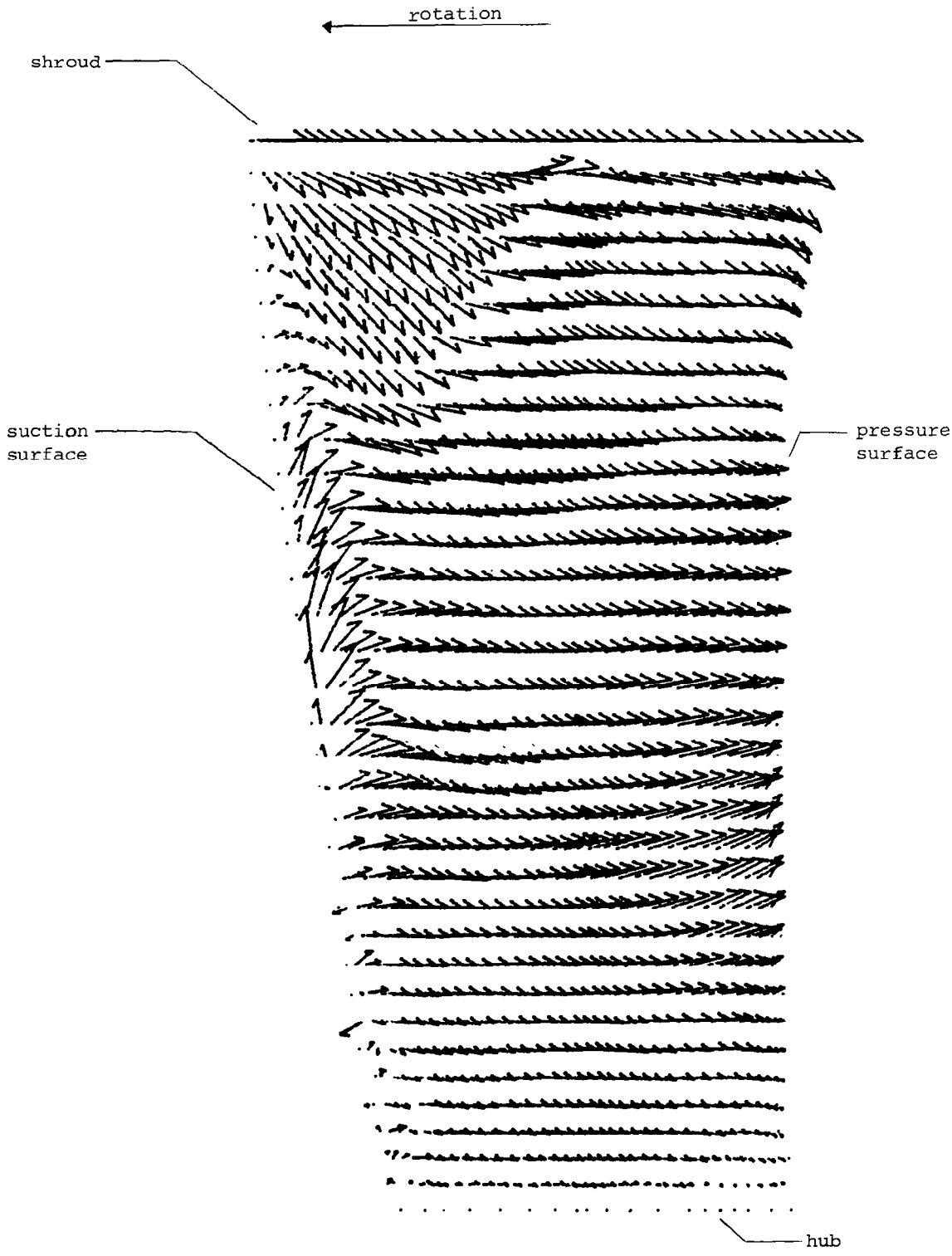

Figure 36. Velocity vector plot of the cross-sectional flow field at a station corresponding to $\hat{z}$ = .1645.

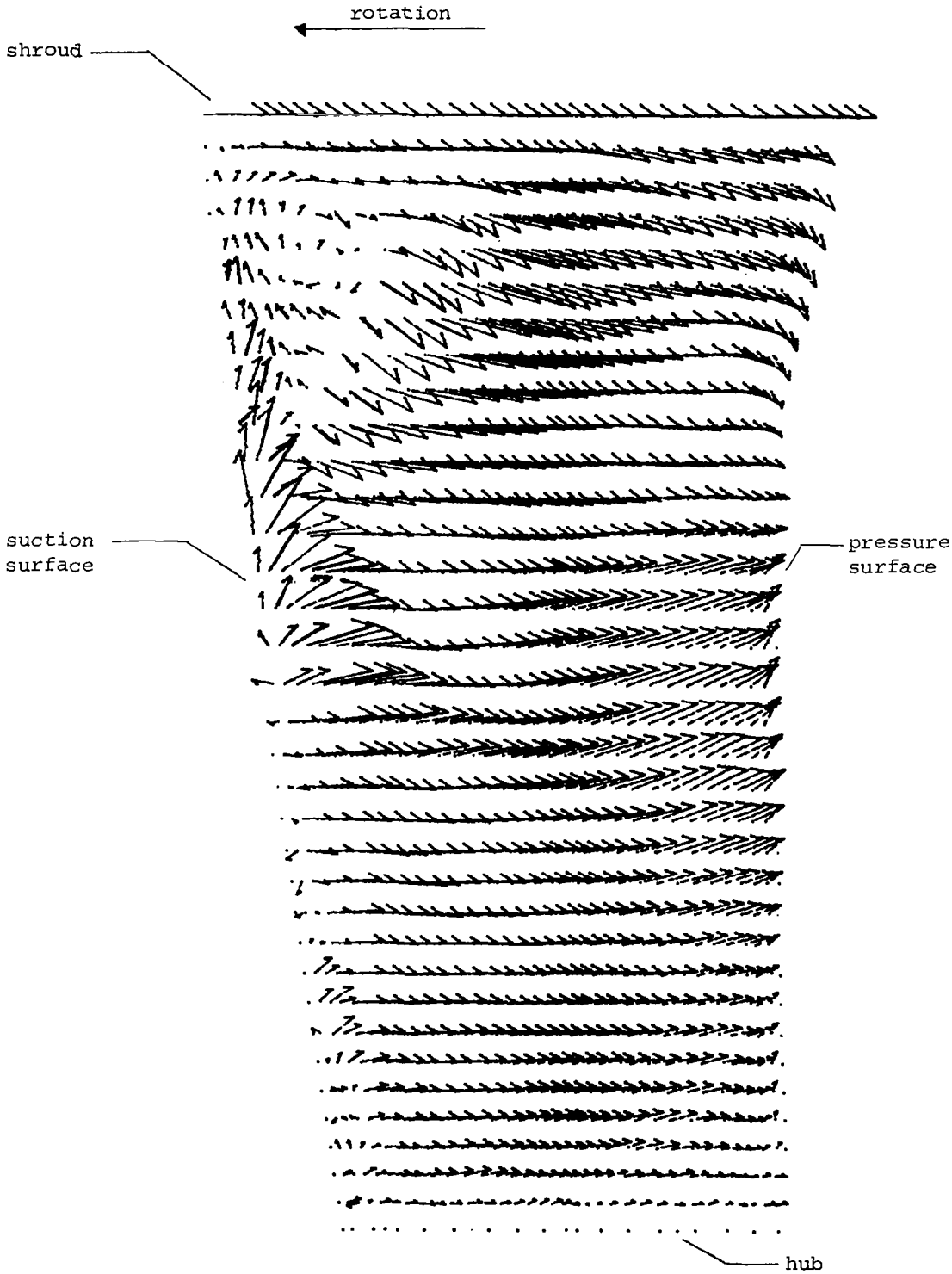

Figure 37. Velocity vector plot of the cross-sectional flow field at a station corresponding to $\bar{z}$ = .185.

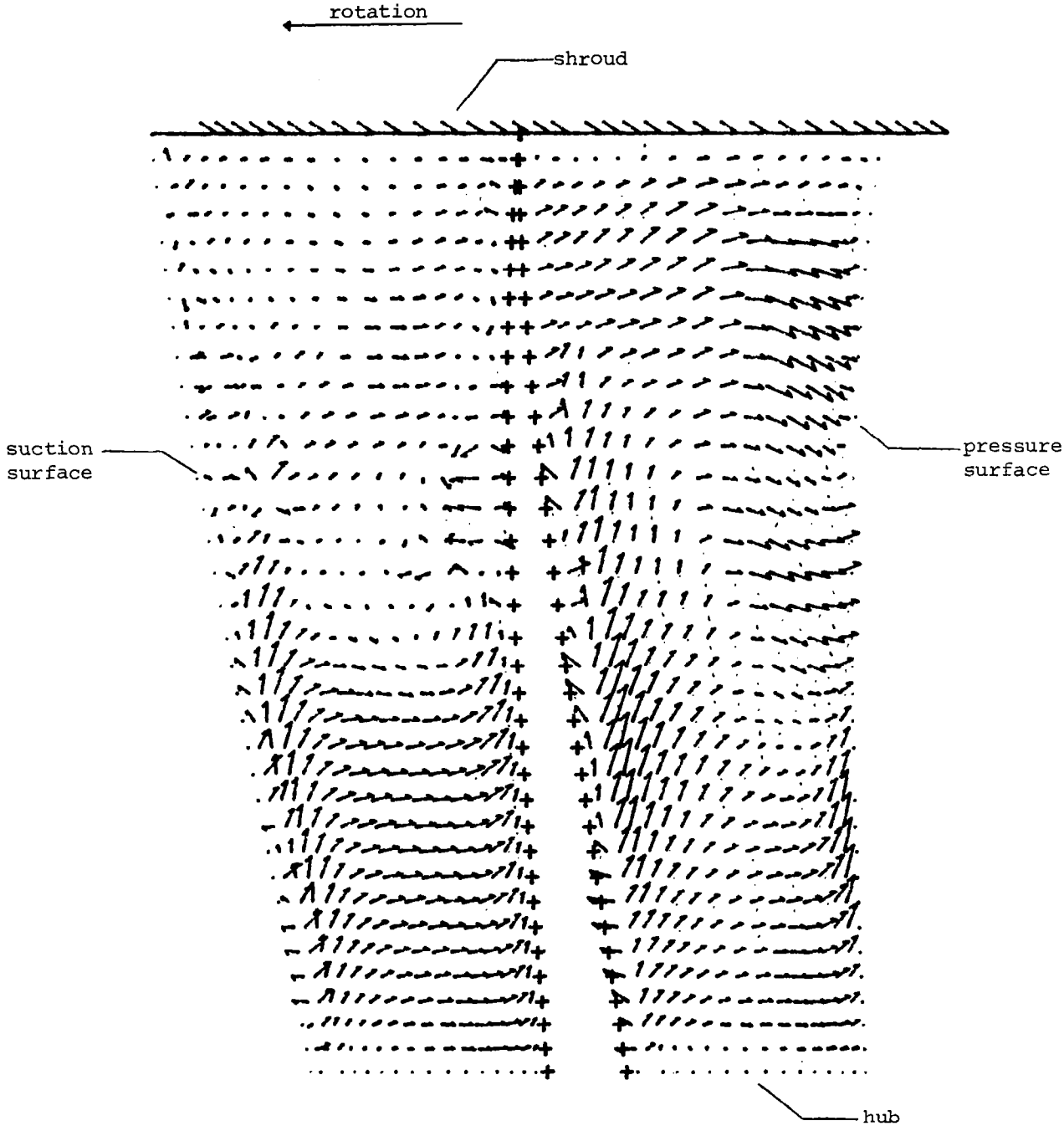

Figure 38. Velocity vector plot of the cross-sectional flow field at a station corresponding to $\bar{z}$ = .440.

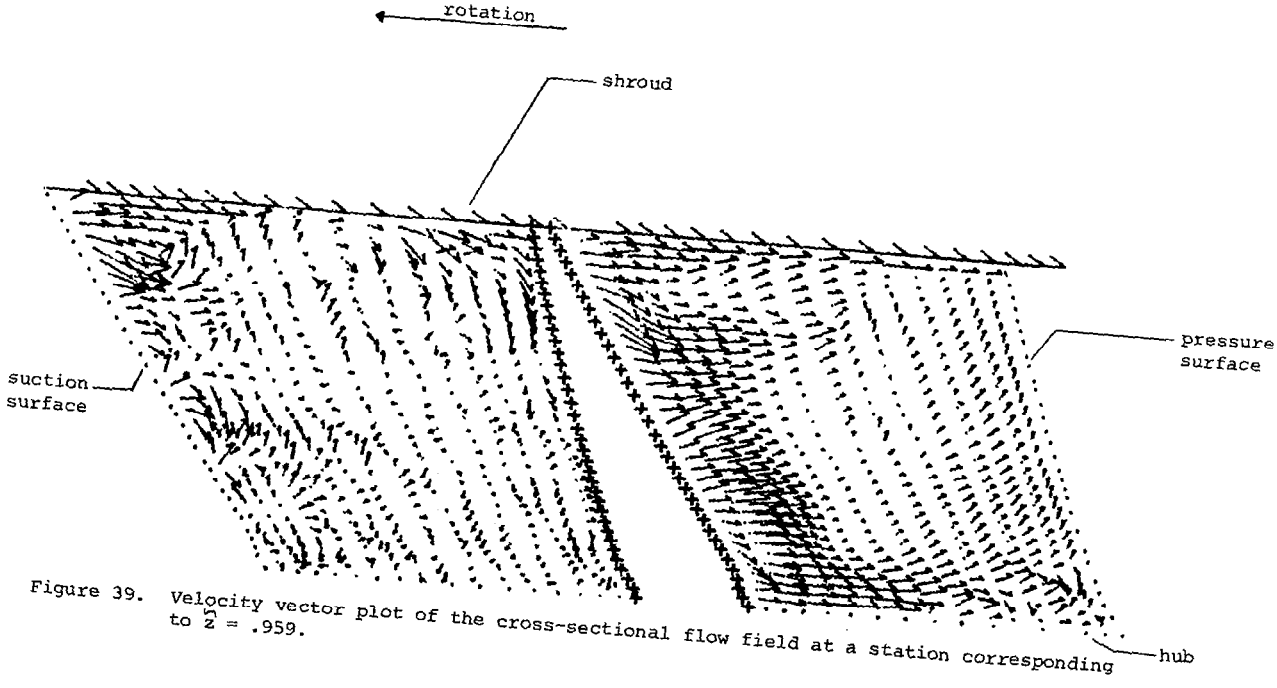

Figure 39. Velocity vector plot of the cross-sectional flow field at a station corresponding to $\bar{z} = .959$.

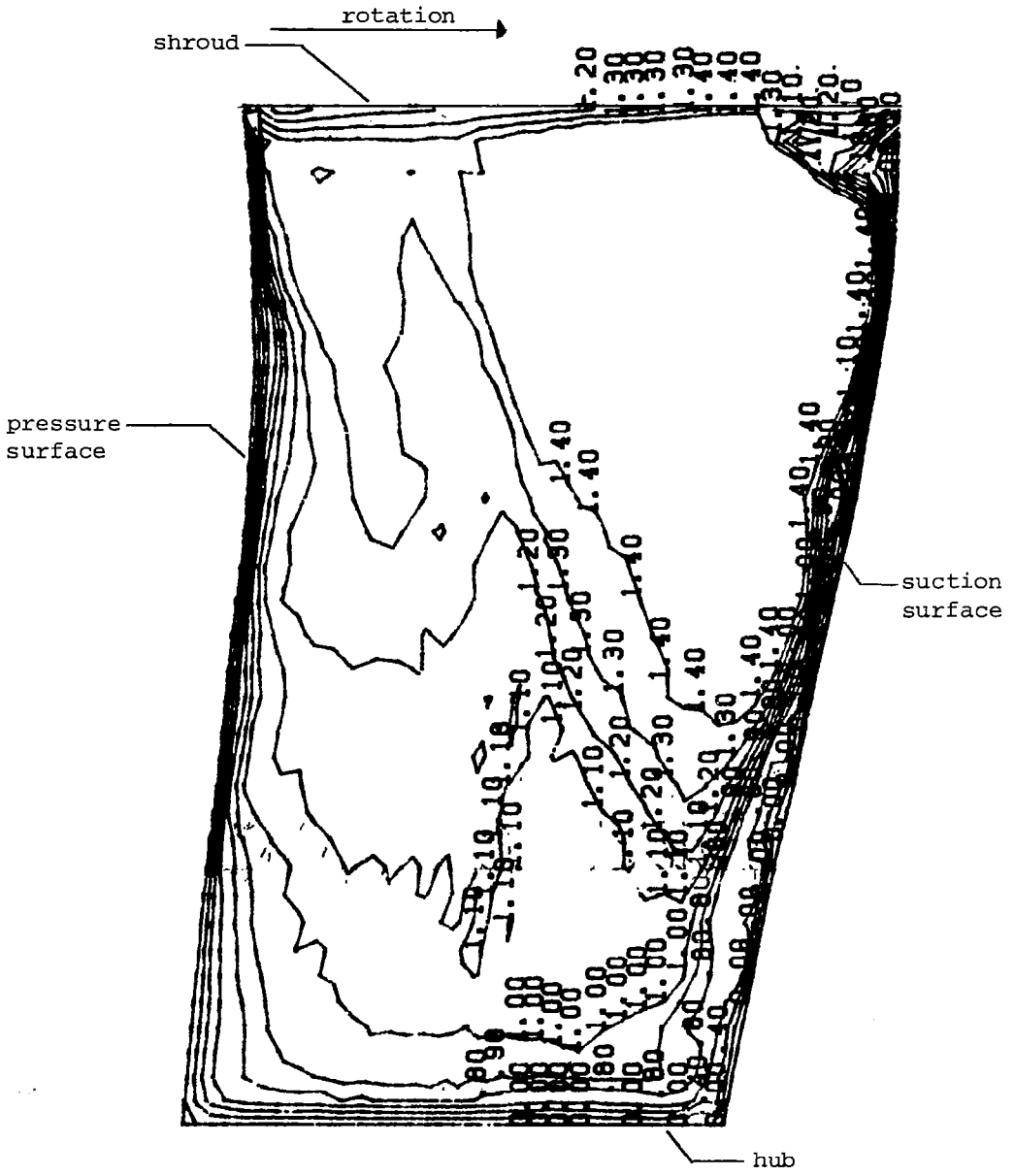

Figure 40. Relative-to-critical velocity ratio contours on a cross-sectional located at non-dimensional station $\hat{z}$ = .105.

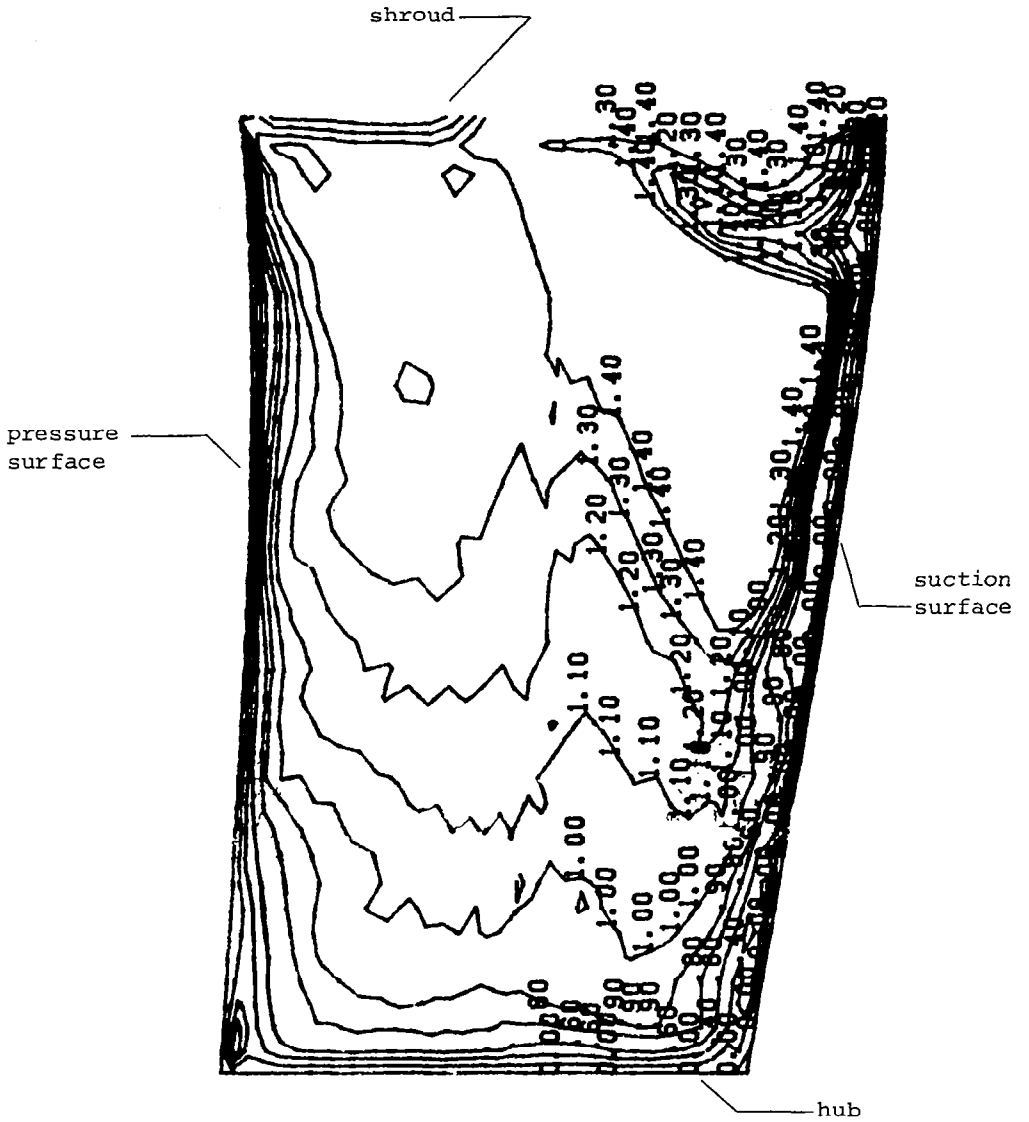

Figure 41. Relative-to-critical velocity ratio contours on a cross-sectional located at non-dimensional station $\tilde{z}$ = .136.

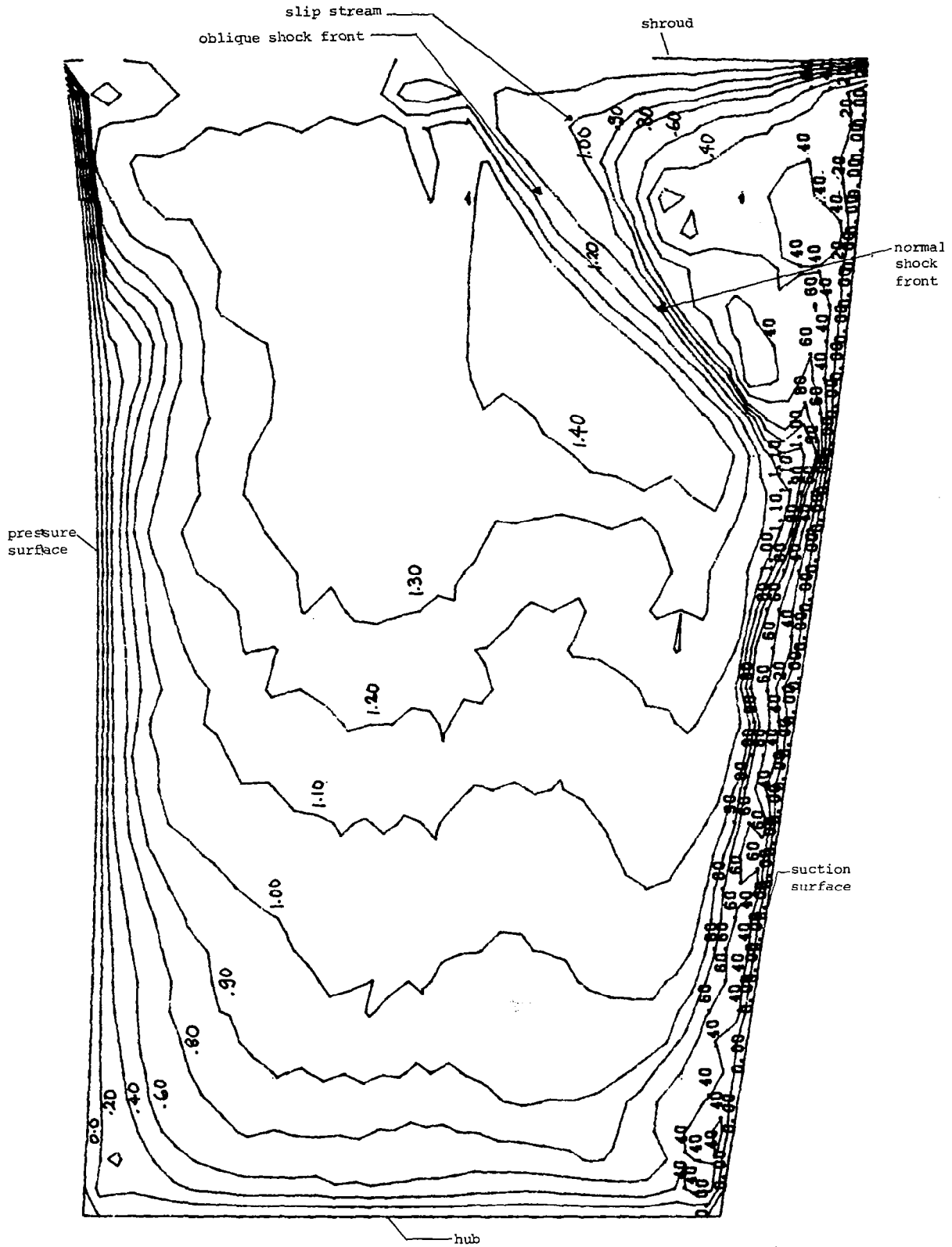

Figure 42. Relative-to-critical velocity ratio contours on a cross-sectional located at non-dimensional station $\bar{z}$ = .185.

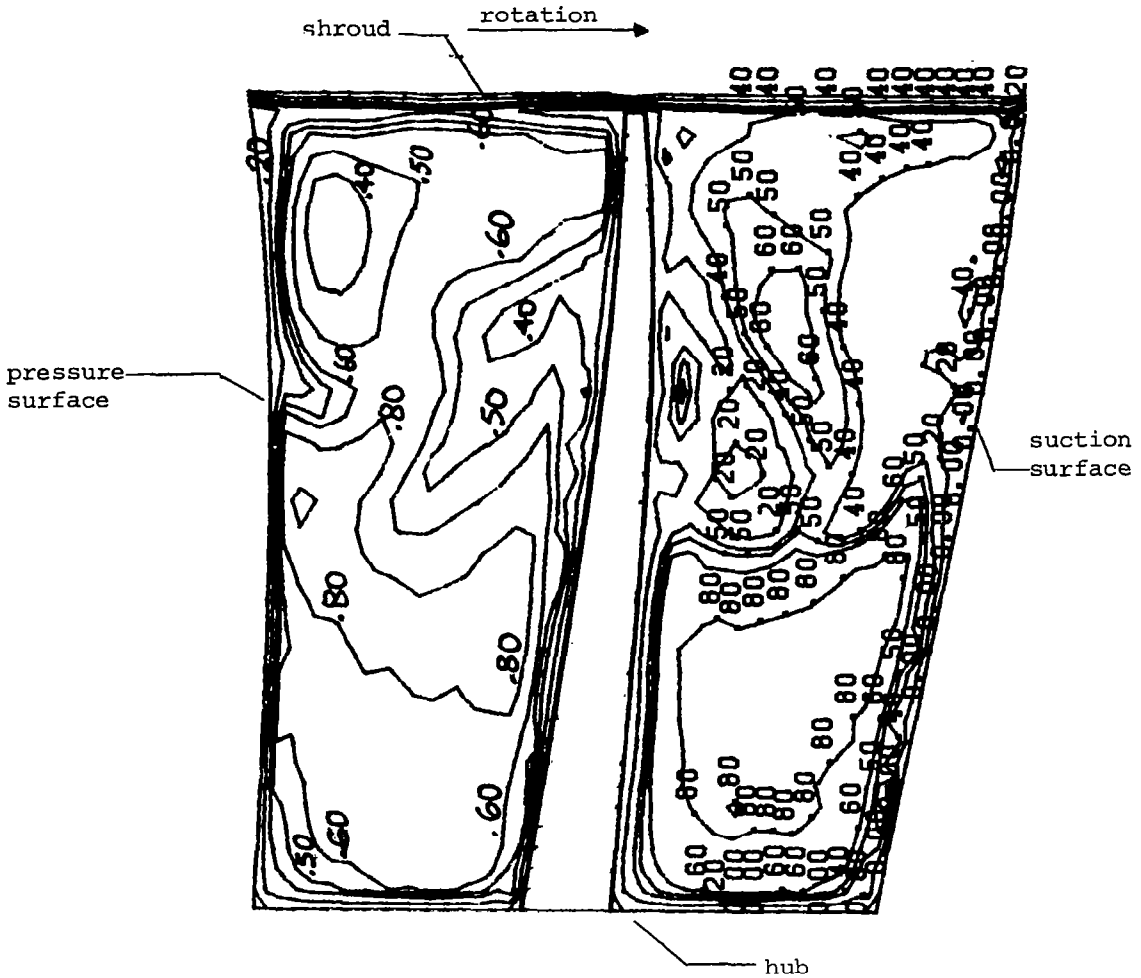

Figure 43. Relative-to-critical velocity ratio contours on a cross-sectional located at non-dimensional station $\bar{z}$ = .440.

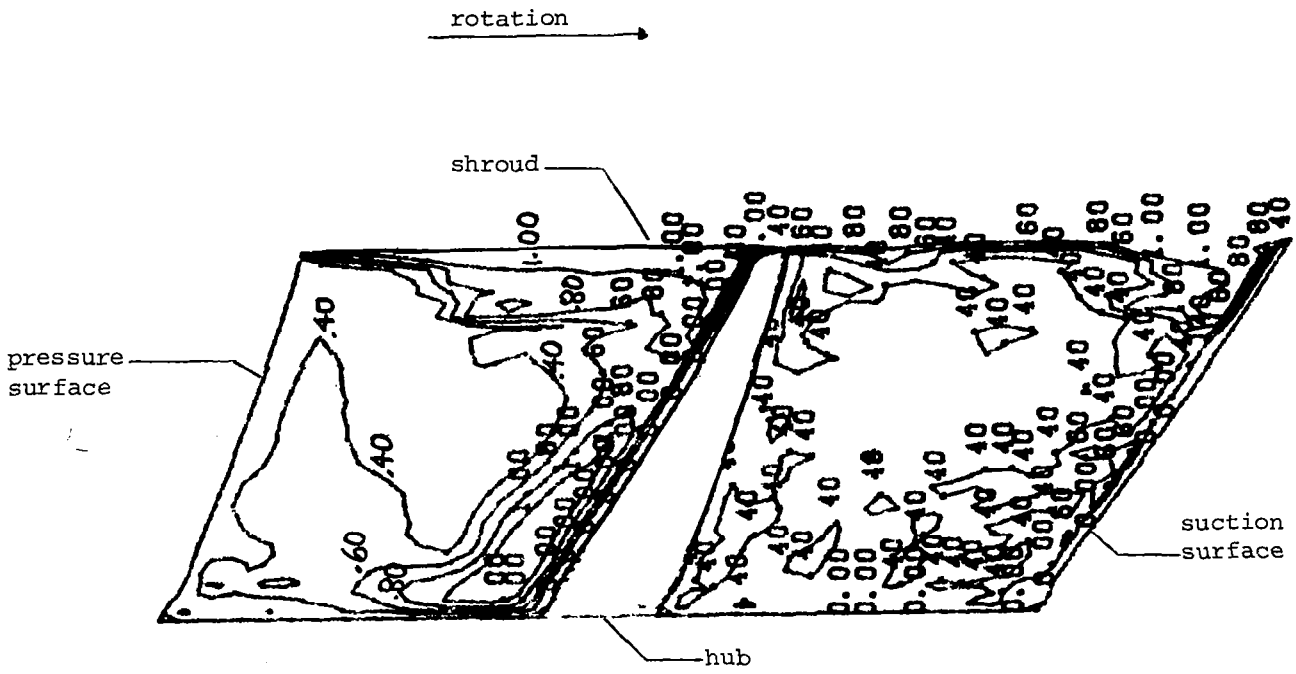

Figure 44. Relative-to-critical velocity ratio contours on a cross-sectional located at non-dimensional station $\hat{z}$ = .954.

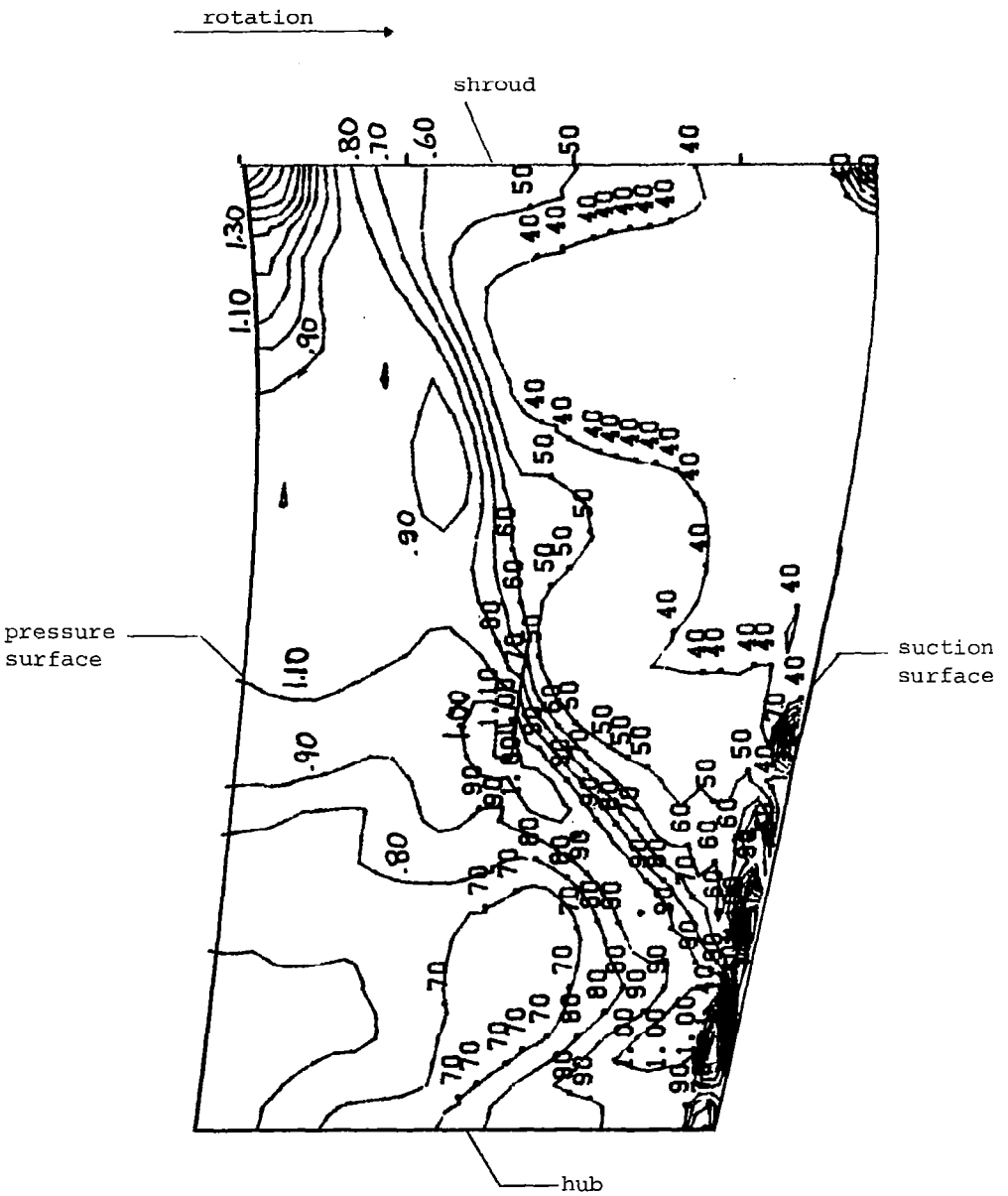

Figure 45. Pressure ratio contours on a cross-section located at a non-dimensional station $\bar{z}^S$ = .105.

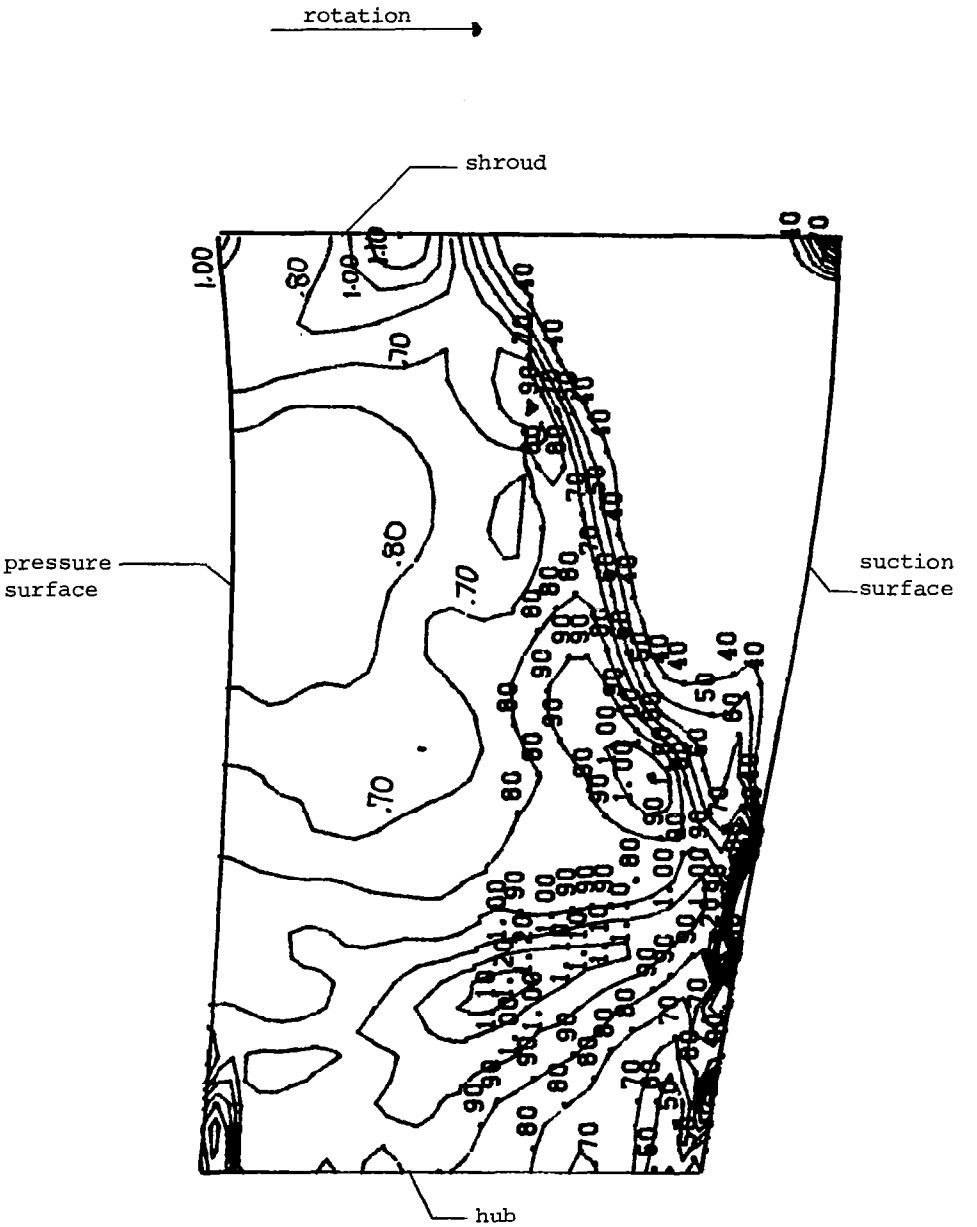

Figure 46. Pressure ratio contours on a cross-section located at a non-dimensional station $\bar{z}$ = .136.

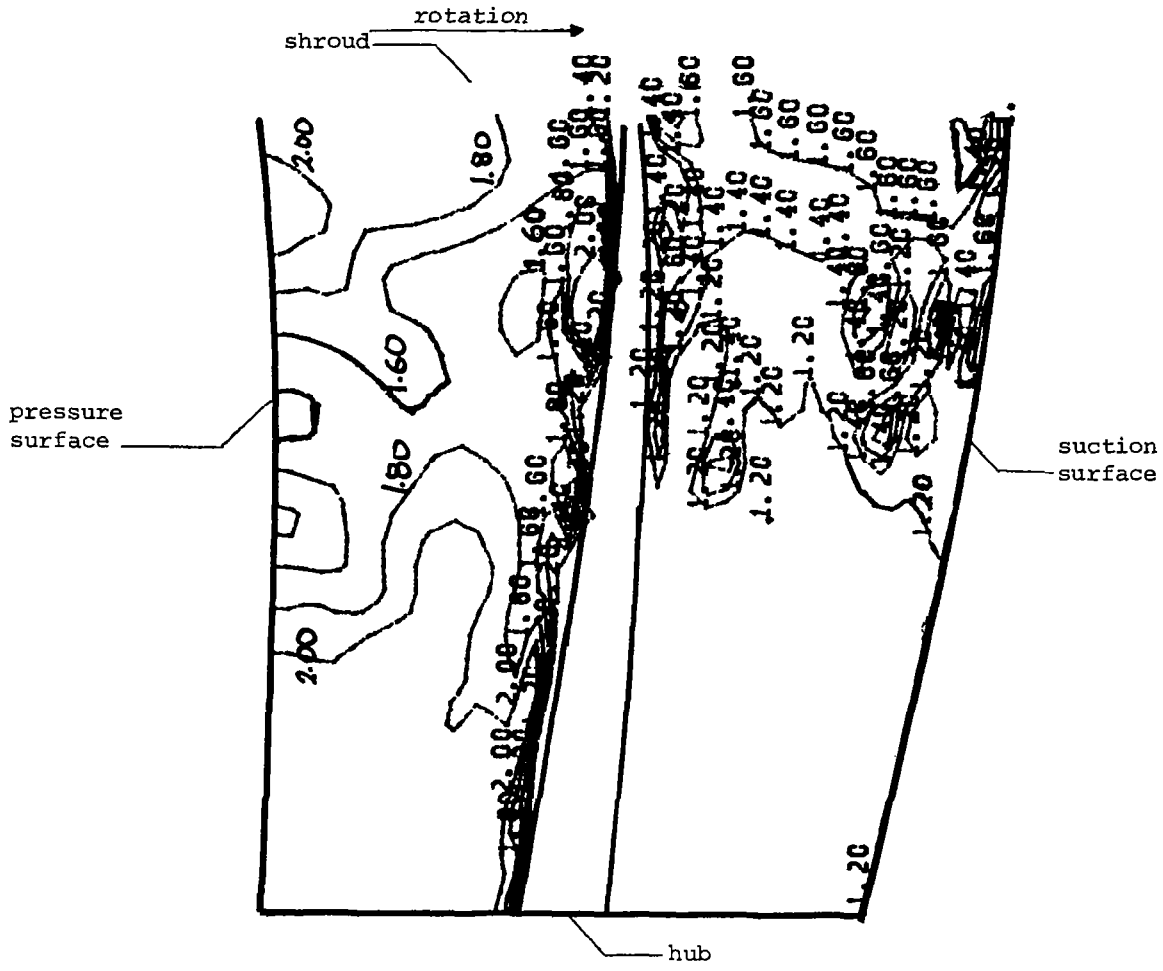

Figure 47. Pressure ratio contours on a cross-section located at a non-dimensional station $\tilde{z}$ = .440.

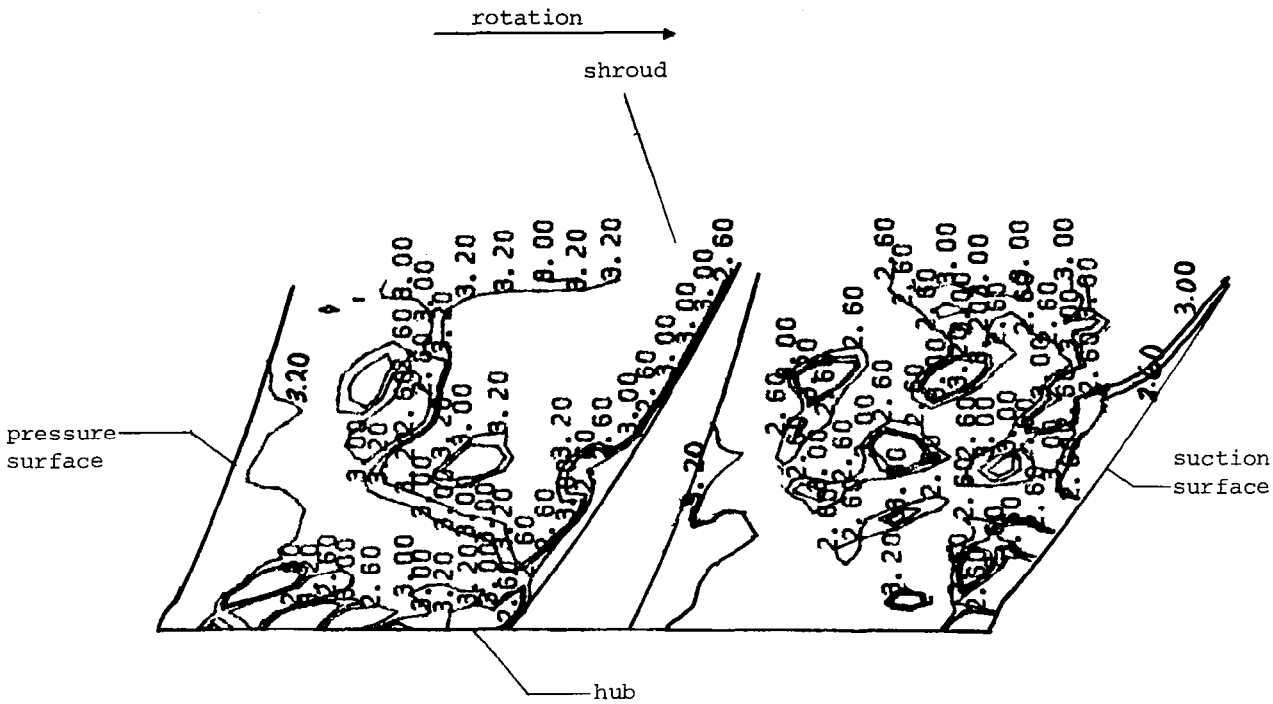

Figure 48. Pressure ratio contours on a cross-section located at a non-dimensional station $\hat{z}$ = .954.

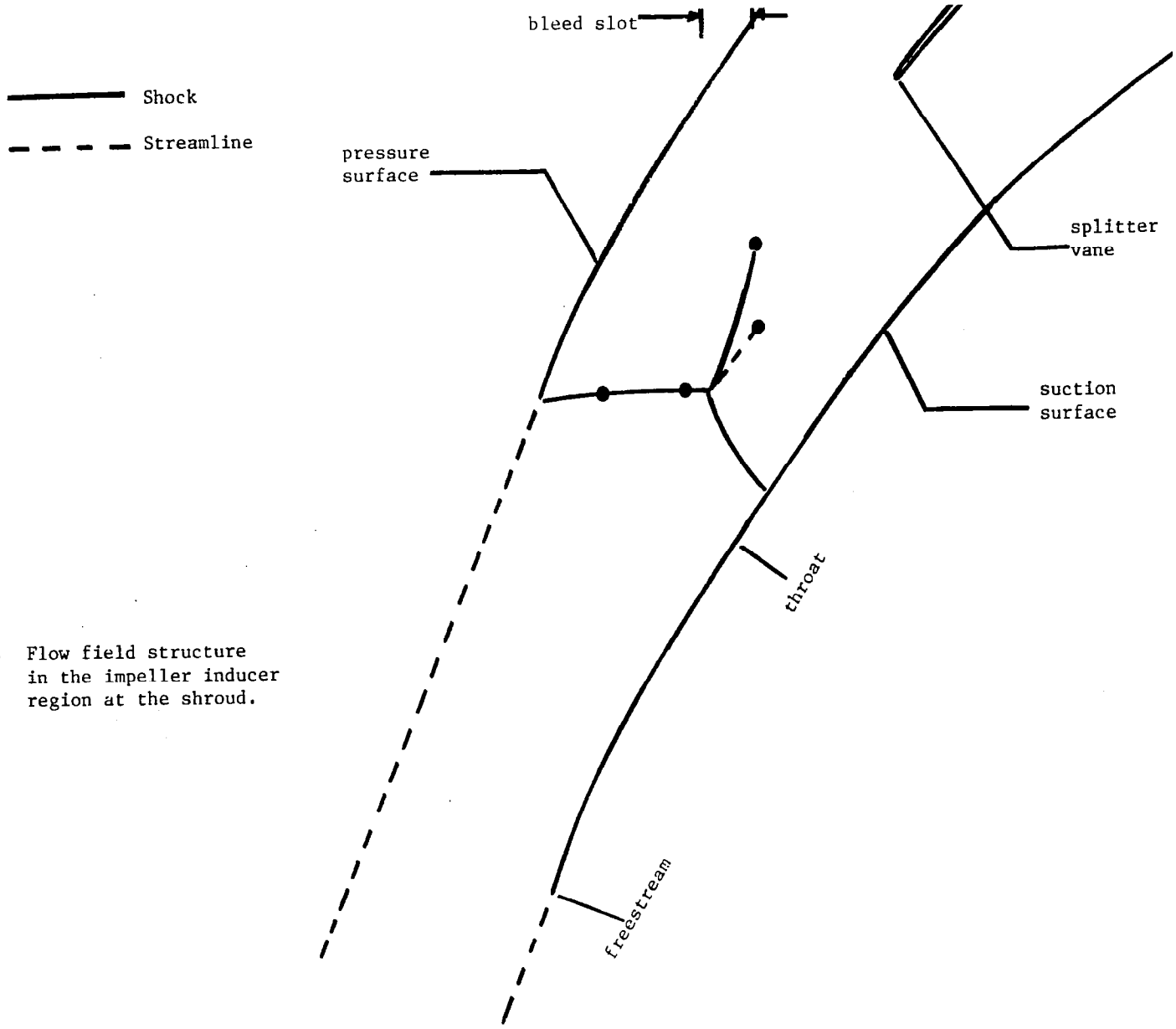

Fig. 49. Flow field structure in the impeller inducer region at the shroud.

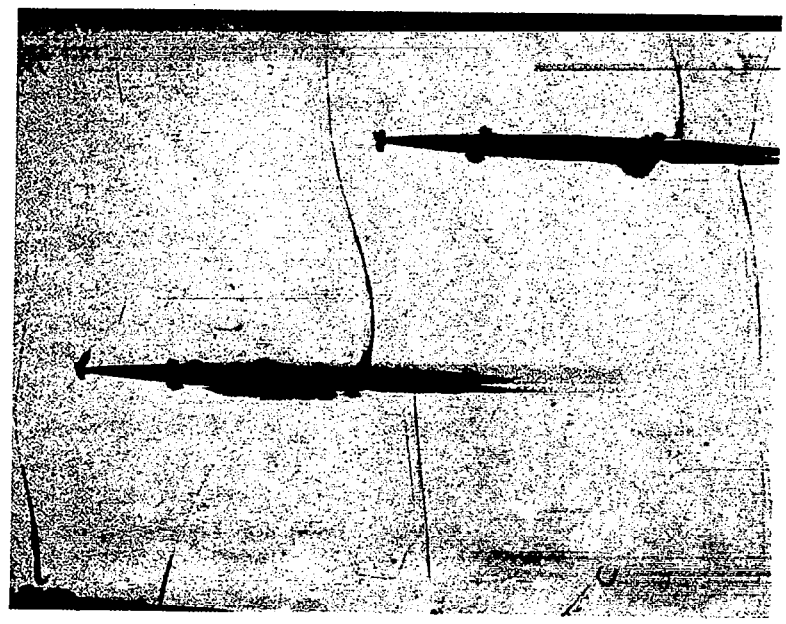

(a) Unstarted flow regime.

(b) Started flow regime.

Fig. 50. Comparison Schlieren photographs for unstarted and started cascades in the transonic flight regime.

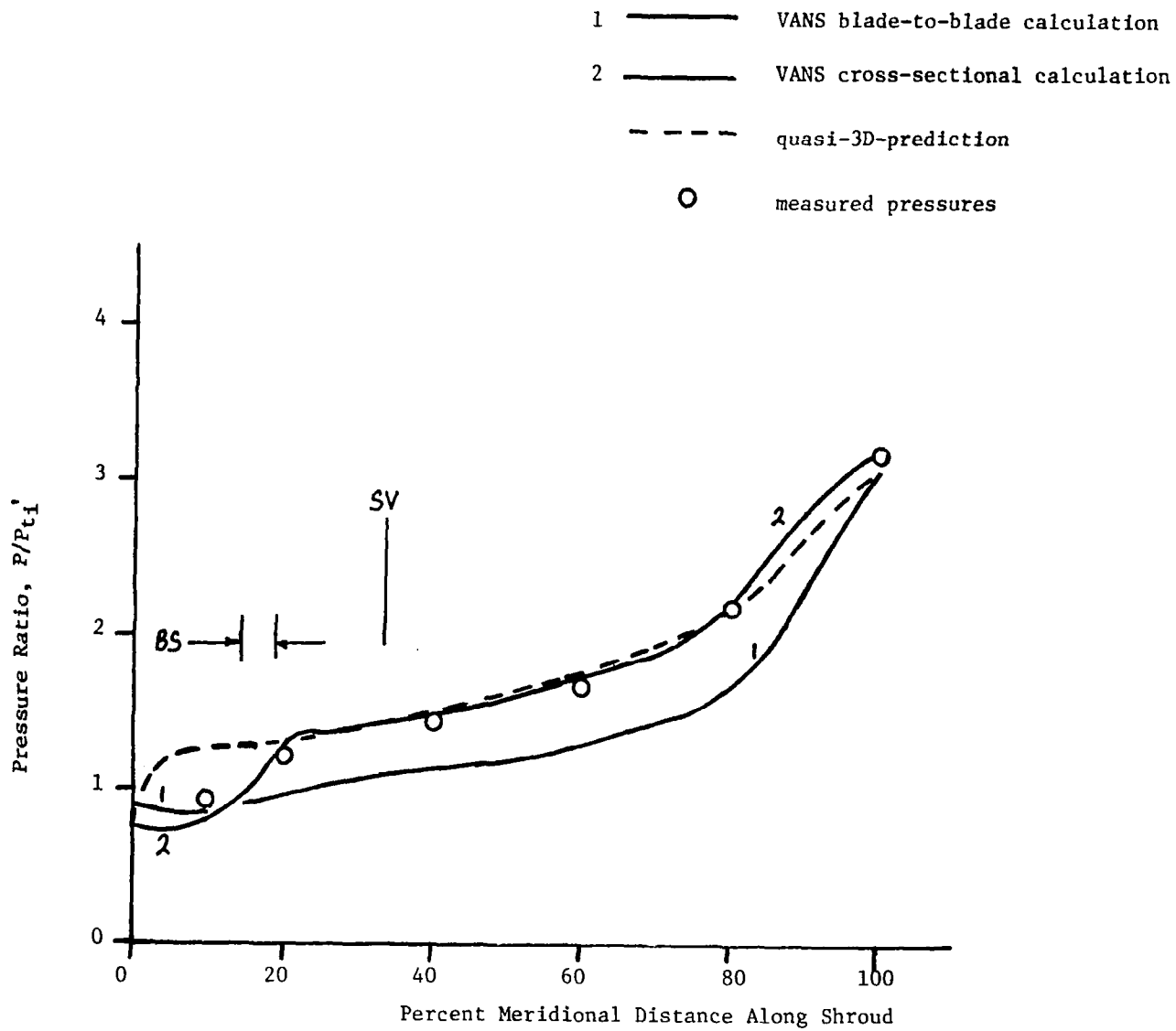

Fig.51. Comparisons of shroud pressure variations; $P_{t_i}' = 2116.2$ psfa.

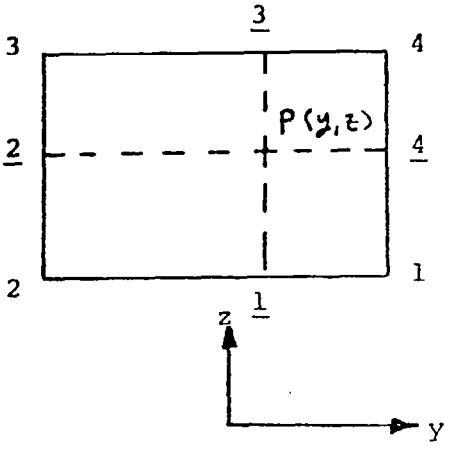

Figure 52b. Two-dimensional linear continuous interpolation.

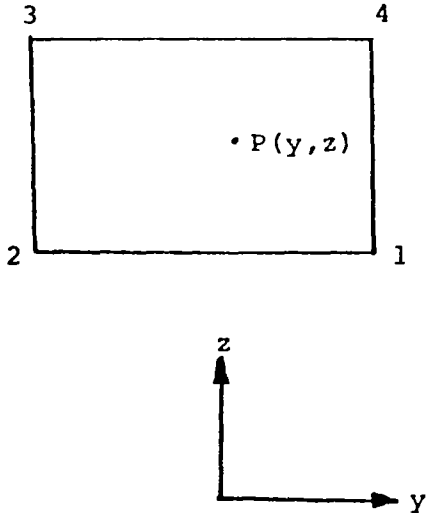

Figure 52a. Two-dimensional double Taylor's series interpolation.

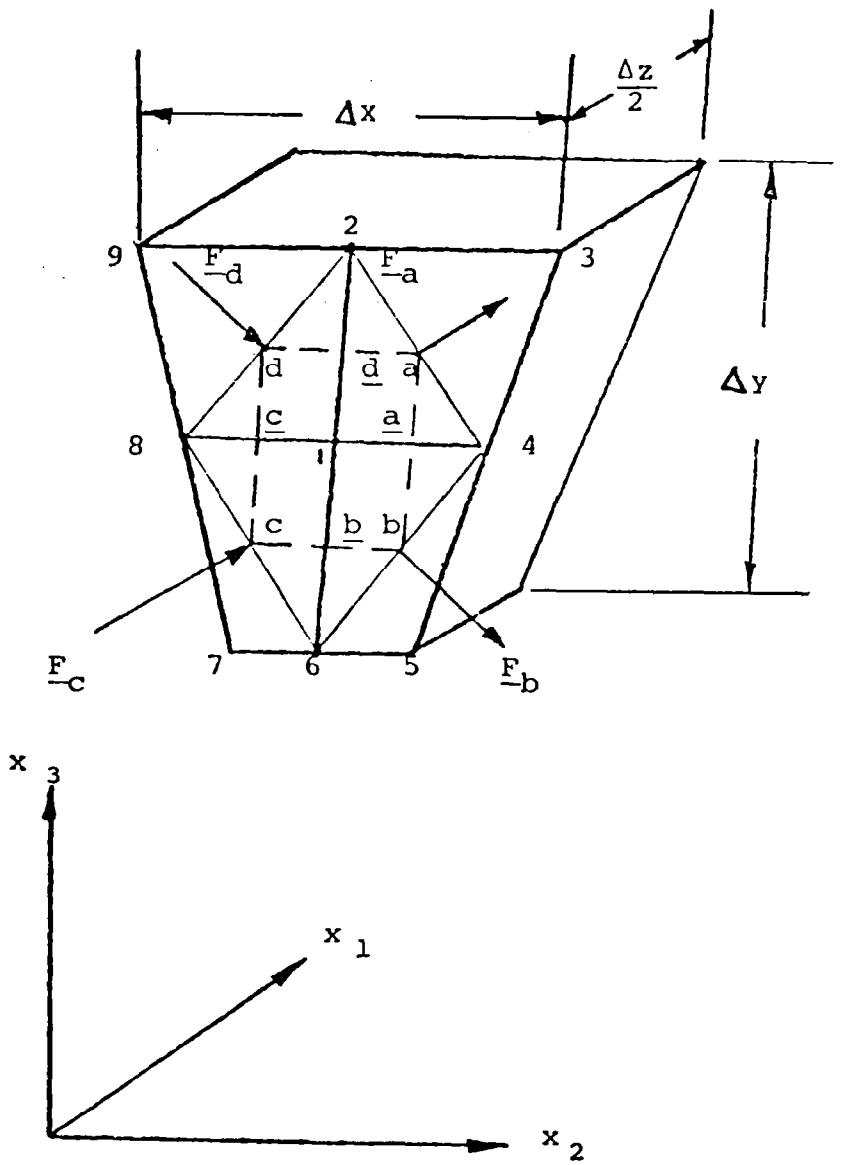

Figure 53. Schematic of three-dimensional computational element illustrating equivalent quadrilateral slab force balance.

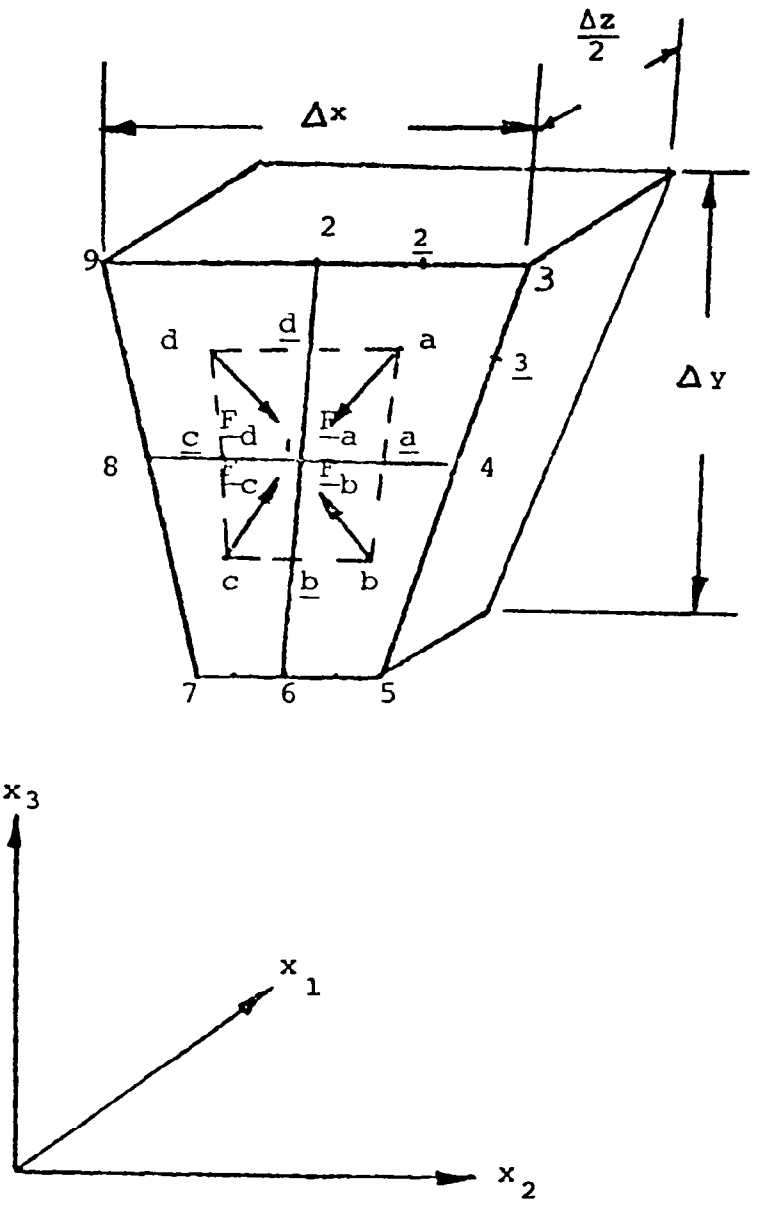

Figure 54. Schematic of three-dimensional computational element illustrating quadrilateral wedge force balance.

1. Report No.	2. Government Accession No.	3. Recipient's Catalog No.
NASA CR-3539		

4. Title and Subtitle	5. Report Date
DEVELOPMENT OF A LOCALLY MASS FLUX CONSERVATIVE COMPUTER CODE FOR CALCULATING 3-D VISCOUS FLOW IN TURBOMACHINES	April 1982
	6. Performing Organization Code: 505-04-82
7. Author(s): Leonard Walitt	8. Performing Organization Report No.: SR-34
	10. Work Unit No.
9. Performing Organization Name and Address: Thermo Mechanical Systems Company, 7252 Remmet Avenue, Canoga Park, California 91303	11. Contract or Grant No.: NAS3-20834
	13. Type of Report and Period Covered: Contractor Report
12. Sponsoring Agency Name and Address: U.S. Army Research & Development Laboratories (AVRADCOM) Propulsion Laboratory, DAVDL-PL Lewis Research Center Cleveland, Ohio 44135	14. Sponsoring Agency Code: 1L162209AH76C

15. Supplementary Notes

Final report. Project Manager, Theodore Katsanis, Fluid Mechanics and Acoustics Division, NASA Lewis Research Center, Cleveland, Ohio 44135.

16. Abstract

The VANS successive approximation numerical method has been extended to the computation of 3-D, viscous, transonic flows in turbomachines. The principal development reported herein is the generation of a cross-sectional computer code, which conserves mass flux at each point of the cross-sectional surface of computation. In the VANS numerical method, the cross-sectional computation follows a blade-to-blade calculation. The VANS blade-to-blade code was developed earlier. Numerical calculations were made for an axial annular turbine cascade and a transonic, centrifugal impeller with splitter vanes. The subsonic turbine cascade computation was generated in blade-to-blade surfaces to evaluate the accuracy of the blade-to-blade mode of marching. Calculated blade pressures at the hub, mid, and tip radii of the cascade agreed with corresponding measurements. The transonic impeller computation was conducted to test the newly developed locally mass flux conservative cross-sectional computer code. Both blade-to-blade and cross-sectional modes of calculation were implemented for this problem. A triple point shock structure was computed in the inducer region of the impeller. In addition, time-averaged shroud static pressures generally agreed with measured shroud pressures. Two principal conclusions are drawn from this research effort: the blade-to-blade computation produces a useful engineering flow field in regions of subsonic relative flow, and cross-sectional computation, with a locally mass flux conservative continuity equation, is required to compute the shock waves in regions of supersonic relative flow.

17. Key Words (Suggested by Author(s))	18. Distribution Statement
Compressible flow analysis; Viscous flow; Three-dimensional flow; Internal flow; Turbomachinery	Unclassified - unlimited STAR Category 02

19. Security Classif. (of this report)	20. Security Classif. (of this page)	21. No. of Pages	22. Price*
Unclassified	Unclassified	115	A06

* For sale by the National Technical Information Service, Springfield, Virginia 22161

NASA-Langley, 1982